I N A U G U R A L - D I S S E R T A T I O N

zur

Erlangung der Doktorwürde

der

Naturwissenschaftlich-Mathematischen

Gesamtfakultät

der

Ruprecht-Karls-Universität

Heidelberg

vorgelegt von

Dipl.-Phys. Markus Hoppe

aus Hanau

Tag der mündlichen Prüfung: 10.01.2001

Differentielle Energieanalyse von Elektronenstrahlen: Eine Studie zur Photoemission aus NEA-GaAs

Gutachter: **Prof. Dr. Andreas Wolf**
Prof. Dr. Reinhard Neumann

Dissertation
submitted to the
Combined Faculties for the Natural Sciences and for Mathematics
of the Rupertus Carola University of
Heidelberg, Germany
for the degree of
Doctor of Natural Sciences

Differential energy analysis of electron beams: A study of photoemission from NEA-GaAs

presented by

Diplom-Physicist: **Markus Hoppe**
born in: Hanau

Heidelberg, 10.1.2001

Referees: **Prof. Dr. Andreas Wolf**
Prof. Dr. Reinhard Neumann

Kurzfassung

Differentielle Energieanalyse von Elektronenstrahlen:
Eine Studie zur Photoemission aus NEA-GaAs

Die mittlere transversale Energie von Photoelektronen aus gekühltem (90 K) GaAs mit negativer Elektronenaffinität wurde mittels adiabatischer transversaler Strahlkompression in einem longitudinalen magnetischen Führungsfeld systematisch untersucht. Darüberhinaus wurde eine neue differentielle Methode zur Energieanalyse von Elektronenstrahlen entwickelt und implementiert. Die 'Markierung' von Photoelektronen in einem engen Intervall longitudinaler Energie erlaubt, durch anschliessende Kompression, die Messung der transversalen Energieverteilung des entsprechenden Subensembles. Durch sequentielle Messungen über den relevanten Bereich der longitudinalen Energie wurde so die erste Bestimmung der zweidimensionalen Energieverteilung $N(E_{\parallel}, E_{\perp})$ ermöglicht. Die Breite der Energieverteilungen zeigt, daß sowohl elastische als auch inelastische Prozesse zum Photoemissionsprozess beitragen. Ein ausgeprägtes Maximum der Verteilung kann möglicherweise dem effektiven Einfang der optisch angeregten Elektronen in einem zweidimensionalen quantisierten Subband in der oberflächennahen Bandverbiegungszone und der darauffolgenden Emission in das Vakuum zugeschrieben werden. Weiterhin konnte gezeigt werden, daß die Produktion von Elektronenstrahlen, die transversal mit der niedrigen Kristalltemperatur thermalisiert sind (entsprechend $k_B T \approx 7.8$ meV), möglich ist. Dazu dürfen nur diejenigen Elektronen extrahiert werden, deren longitudinale Energie die Position des Leitungsbandminimums nicht mehr als etwa 20 meV unterschreitet.

Abstract

Differential energy analysis of electron beams:
A study of photoemission from NEA-GaAs

Systematic measurements of the mean transverse energy of electrons photoemitted from GaAs activated to negative effective electron affinity were performed at cryogenic crystal temperatures (90 K), employing the adiabatic transverse compression of the beam in a longitudinal magnetic guiding field. In addition, a new differential method of energy analysis of electron beams was developed and implemented. The 'marking' of electrons within a narrow interval of longitudinal energy prior to the compression allows the measurement of the transverse energy distribution of the respective subensemble. Successive measurements covering the relevant range of longitudinal energy permitted the first determination of the two-dimensional energy distribution $N(E_{\parallel}, E_{\perp})$. The width of the distribution indicates that elastic as well as inelastic processes take place during the process of photoemission. A distinctive maximum of the distribution can possibly be assigned to an effective capture of photo-excited electrons in a two-dimensional quantized subband in the surface-near band bending region and the subsequent emission into vacuum therefrom. Furthermore, it was proved that it is possible to produce electron beams which are transversely thermalized with the low crystal temperature (i.e. $k_B T \approx 7.8$ meV). For this purpose only electrons should be extracted whose longitudinal energies fall below the position of the conduction band minimum by not more than about 20 meV.

Contents

1. Introduction

Electron beams are used as tools for spectroscopy and material processing in a large variety of applications. The resolution of these techniques is often limited by the energy spread of the electron beam. To reach a narrow electron energy distribution, the beam is usually injected into an electron monochromator, which acts as a bandpass filter on the energy distribution. The often undesirable consequence of this procedure is the corresponding drastic decrease in current density. The development of sources of intense electron beams with low initial energy spreads would thus be very profitable.

A promising candidate for such a source is a photocathode consisting of a p-doped GaAs semiconductor activated to negative electron affinity (NEA). The state of NEA, which is achieved by co-depositing a few monolayers of cesium and an oxidizing species onto the clean semiconductor surface, is characterized by a position of the vacuum level below the conduction band minimum in the bulk. It was first observed in 1965 by Scheer and van Laar [1], who recognized its suitability for the application as highly efficient photoemitters in the visible and near infrared. The potential application of NEA-GaAs photocathodes as sources for intense cold electron beams was soon realized [2, 3]. Since the conduction band minimum represents a natural barrier for the energy relaxation of excited electrons in the bulk, electron lifetimes in the conduction band are sufficient for the relaxation at the conduction band minimum and the thermalization of the electron ensemble with the bulk temperature. The crystal temperature can be chosen freely, hence it is possible to produce an intense electron ensemble with very low energy spreads *inside* the semiconductor. These electrons thermalized at the conduction band minimum can, in the state of NEA, easily escape from the semiconductor by tunneling through the remaining potential barrier at the surface.

The electron energy distribution of the photoemitted electrons *outside* the material is, however, strongly modified by the processes taking place during the electron transfer through the semiconductor-vacuum interface. In spite of the long time which passed since the discovery of the state of NEA, these processes are still not well understood. The photoelectron energy distribution in the direction perpendicular to the surface (longitudinal

direction) is easily accessed by the conventional energy analyzers, e.g. retarding field analyzers and cylindrical mirror analyzers. It was thus early shown that the narrow energy spread inside the bulk material is, in this direction, indeed inherited by a small fraction of the photoemitted electrons [3, 4]. The largest part of the photoelectrons is, however, distributed over the full range of accessible longitudinal energies down to the vacuum level. The transverse (i.e. the direction parallel to the surface) energy distribution of the photoelectrons remained controversial: reported values for the mean transverse energy (MTE) of electrons emitted from a sample kept at room temperature scatter between 30-100 meV. The physics of the photoemission process from NEA-GaAs remains unclear until today.

The background for this thesis is provided by the study of electron-ion interactions in the heavy-ion storage ring TSR at the Max-Planck-Institut für Kernphysik in Heidelberg [5]. An electron beam immersed in a magnetic field (longitudinal direction) is overlapped with the circulating ion beam in a section of the ring (the so-called 'electron cooler') and serves both for electron cooling of the ion beam and as an electron target [6, 7]. The magnetic field does not only allow the efficient guiding of the electron beam but also separates the longitudinal from the transverse degrees of freedom [8]. Since a high current density, together with a high beam diameter, is desired for the electron beam, a thermionic cathode is conventionally used for these experiments. The initial energy spread of thermionically emitted electron beams is corresponding to the cathode temperature and thus amounts to $k_BT \approx 100$ meV, with k_B denoting the Boltzmann constant. The longitudinal energy spread (in the beam rest frame) is lowered by the acceleration of the electron beam. The transverse energy spread of the electron beam can be lowered by applying the technique of adiabatic transverse expansion (ATE) of the electron beam in a magnetic field with spatially decreasing strength [6].

A new electron target for the TSR which is currently under construction [9, 10, 11] will allow the separation of the electron cooling from the interaction region. It will furthermore permit the extensive use of adiabatic transverse expansion and adiabatic (slow) acceleration, leading to colder electron beams. These techniques, in spite of the optimized experimental arrangement, have practical limits. A reliable alternative source of intense electron beams which produces even colder initial beams is thus advantageous.

Since for the investigation of several particularly interesting resonances in the TSR specially the transverse energy sets a lower limit to the resolution, a photocathode set-up was constructed by Pastuszka et al. in order to study the transverse energy spreads of magnetized electron beams [12, 13, 14, 15]. Broadenings of the electron distributions result-

ing from intra-beam scattering can be minimized by magnetic guiding fields of sufficient strength [16], such that operation with appreciable current densities as well as relatively extended drift regions become possible. The latter fact also admits beam manipulations prior to the analysis, in particular the blocking of low longitudinal energy electrons by external potential barriers and ATE of the electron beam. ATE can be applied to cause a controlled transfer of energy between the longitudinal and transverse degrees of freedom which are well separated due to the magnetic guiding field. Thus it allows one to obtain information about the initial transverse energy distribution by a (in principle straight forward) measurement of the change of the longitudinal energy distributions.

This method was, after a test with a conventional thermionic cathode [15], applied to the study of the transverse energy distribution of electrons photoemitted from NEA-GaAs in order to test the utility of this source for the production of transversely cold electron beams. These studies [12, 13] showed that the mean transverse energy MTE of the photoelectrons strongly depends on the mean longitudinal energy of the emitted electrons: The transverse temperature for photoelectron ensembles with longitudinal energies above the conduction band minimum in the bulk of the semiconductor was found, similar to the longitudinal case, close to the ambient temperature (at about 300 K); electron ensembles with lower mean longitudinal energies showed enhanced MTE. Several measurements indicated a strong further reduction of the MTE of the high longitudinal energy electrons upon a cooling of the cathode with liquid nitrogen.

For the optimization of the cathode parameters in order to improve its performance in specific applications, e.g. as a source of intense cold electron beams, it is thus necessary to further understand the details of the photoemission process. It is in particular desirable to obtain more detailed experimental data concerning the energy spreads of the photoelectrons.

This thesis concerns the detailed investigation of the initial energy spreads of electron beams photoemitted from NEA-GaAs at cryogenic temperatures. The experimental access proved to be tricky, since the shifts of longitudinal energy resulting from ATE are, at least in the present set-up, in the meV-range and have to be measured in a varying magnetic guiding field. Improvements in the resolution and accuracy enabled the first systematic studies of transverse energy spreads of electron beams produced by photoemission from NEA-GaAs at cryogenic temperatures. Furthermore, a new method of differential energy analysis of magnetized electron beams has been developed [17]. By marking an electron subensemble within a narrow interval of longitudinal energies prior to the expansion, the transverse energy distribution of longitudinal 'slices' of the complete two-dimensional energy distribution can be accessed experimentally. Subsequent measure-

ments at different longitudinal marking energies allows the reconstruction of the *complete* energy distribution of electrons over the longitudinal and transverse energy ranges. The application of this new technique permitted the first determination of the complete initial energy distribution of electrons photoemitted from NEA-GaAs.

The following chapter reviews the present understanding of photoemission from NEA-GaAs. Chapter 3 introduces the concepts of magnetized electron beams. Chapter 4 addresses to aspects of the photocathode preparation procedure applied for the experiments reported in this thesis. Experimental details concerning the energy analysis of photoemitted electron beams are presented in chapter 5, whereas the results of the measurements of photoelectron energy distributions at cryogenic temperatures are presented and discussed in chapter 6. Conclusions and an outlook are given in chapter 7.

2. NEA-GaAs and the physics of photoemission

For illumination with photon energies in the vicinity of the band gap, the main part of the electrons is excited far enough from the surface to undergo scattering events in the bulk prior to the emission into vacuum. These bulk effects are, in contrast to the physics related to the semiconductor-vacuum interface, well understood. Thus it is favorable to separate, after an introduction to the concept of negative electron affinity in section 2.1, the discussion orienting on the three-step model of photoemission [18]. Section 2.2 is concerned with steps one and two, i.e. electron excitation respectively transport to the semiconductor surface, including relaxation and thermalization processes. The experimental results and theoretical approaches regarding the third step, the emission process itself, are reviewed in section 2.3. In the closing section 2.4 practical limits for the application of NEA-GaAs photocathodes are discussed.

2.1 The concept and formation of negative electron affinity

The electronic conditions at an intrinsic-semiconductor/vacuum interface are illustrated in figure 2.1 (a). The work function φ is defined as the energy necessary to extract an electron from the solid material, i.e. the distance in energy scale between the vacuum level and the Fermi level (E_{vac} resp. E_F). The height of the potential barrier an electron at the conduction band minimum (CBM) at the surface still has to overcome to escape into vacuum is defined as the electron affinity χ. For undoped, clean GaAs χ amounts to about 4 eV [19].

Figure 2.1 (b) illustrates the condition of NEA invoked on a strongly p-doped material by 'activation', that is a deposition of cesium and an oxidizing species on the crystal surface.

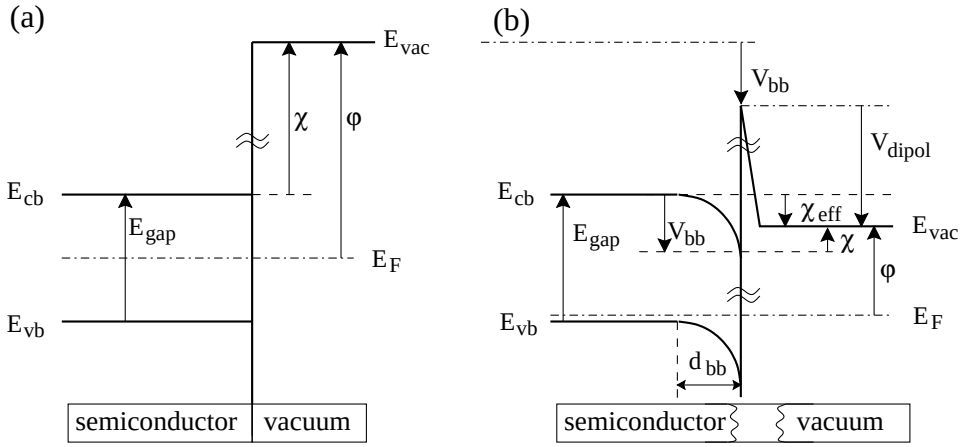

Figure 2.1: Sketch of the electronic conditions at the semiconductor-vacuum interface for (a) intrinsic GaAs, and (b) strongly p-doped material activated to negative electron affinity. The mirror image potential acting on an emitted electron is neglected for clarity.

Several models have been proposed for the structure of the activation layer and thus for the formation of NEA [1, 20, 21, 22]. At least for commonly used thicknesses of the activation layer (i.e. a few monolayers), experimental results concerning the energy spreads of the photoemitted electrons did not show significant dependencies on the applied oxidizing species [12, 23]. The only model consistent with these observations is the (double) dipole layer model [20, 1].

The strong p-doping leads to a position of the Fermi level in the vicinity of the valence band maximum E_{vb} in the bulk. In recent years it could be demonstrated that clean surfaces of p-doped GaAs do, in contrast to the former belief, not show significant band bending [24, 25]. Donor-like surface states originating from the adsorption of cesium contribute their electrons to the bulk, building up a considerable positive charge on the surface[1]. Equilibrium is maintained by a downward band bending V_{bb}. This leads to a partial crossing of these states 'back' below the Fermi level and to an accumulation layer in the surface-near region by a downward shift of bulk acceptors. Since the Fermi level is not affected, the work function φ is decreased by the same amount V_{bb}. The extension d_{bb} of the band bending region does, in opposite to the value of V_{bb}, decrease with increasing doping level. For GaAs-photocathodes it is advantageous to provide a high V_{bb} and a low d_{bb}. The high doping levels of typically 10^{-19} cm^{-3} lead to a value of d_{bb} of about 10 nm with the reported values for V_{bb} of typically between 0.3 eV and 0.5 eV [26, 4].

[1] The evolution of the electronic properties of the semiconductor-vacuum interface during photocathode activation is rather sophisticated. Its detailed discussion is beyond the scope of this thesis, such that only the principle points are discussed here. For more detailed information, see e.g. [24, 26].

The remaining non-ionized cesium is polarized, leading to a dipole layer on the surface; it can, in a simple picture, be imagined as similar to a parallel-plate capacitor. The resulting electric field reduces the electron affinity by decreasing the vacuum level in respect to the bulk levels (see V_{dipol} in figure 2.1 (b)), leaving behind only a thin potential barrier at the surface. This effect is enhanced by a co-deposition of an oxidizing species, which is usually explained with the formation of additional dipoles on top of the initial one [20]. Since the absorption length as well as the mean free path of electrons in the conduction band minimum are much higher than the thickness of the band bending region (see below), the difference of the conduction band minimum *in the bulk* and the vacuum level is of particular relevance. This parameter is defined as the *effective* electron affinity χ_{eff}. Its value can even become negative, a condition which is for simplicity usually referred to as negative electron affinity (NEA) [2]. Electrons that are accumulated at the conduction band minimum (in the bulk) thus have sufficient energy to escape into vacuum by tunneling through the remaining barrier.

2.2 The electron energy distribution in the bulk

Figure 2.2 (a) shows the relevant part of the electronic band structure of GaAs: The minimum distance in energy scale between the highest occupied valence band and the lowest conduction band is located in the center of the Brillouin zone (Γ-point). The width of the band gap E_G amounts to 1.42 eV at 300 K and increases to about 1.51 eV at 77 K (boiling point of nitrogen).

The extinction coefficient for photons with the energy $h\nu$ in the vicinity of the band gap is approximately $\alpha(\nu) \propto \sqrt{h\nu - E_G}$. This factor results from the available phase-space, the matrix element for the transition is nearly constant in the vicinity of the band gap [2]. Thus the mean absorption length $1/\alpha$ amounts to approximately 1 μm for infrared light with a wavelength of 800 nm at room temperature. The optical inter-band transitions are visualized in the band diagram in figure 2.2(a) for illumination with monochromatic light: Conservation of energy and momentum allows the excitation of electrons to the conduction band only for a specific set of $\vec{k}$. The respective difference in energy between one of the valence bands and the conduction band has to match the photon energy. The negligible momentum transfer due to photon absorption further restricts the set to vertical transitions. The initial energy of these excited electrons thus is determined by the band structure and the photon energy.

The excited electrons relax to the conduction band minimum mainly by emission of longitudinal-optical phonons and by scattering with holes. The latter process is particu-

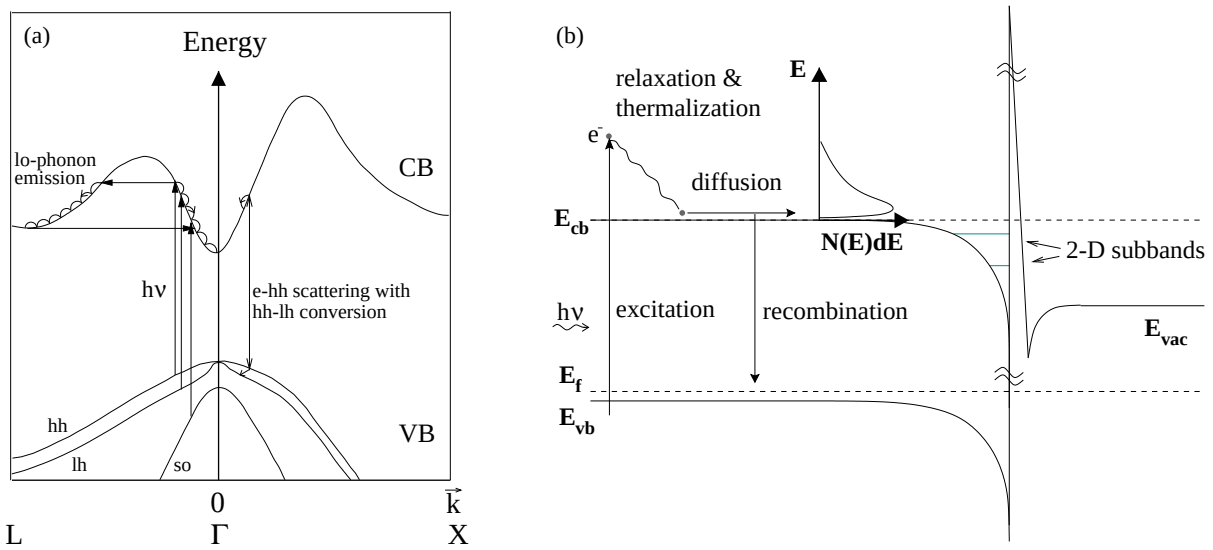

Figure 2.2: Sketches of the electronic structure of NEA-GaAs and the processes relevant for photoemission therefrom. (a) Band diagram of GaAs. 'CB' denotes the conduction band, while 'hh', 'lh' and 'so' denote the heavy-hole, light-hole and the split-off subband of the valence band (VB), respectively. The processes of electron excitation by monochromatic light ($h\nu$) as well as the energy loss mechanisms of longitudinal-optical (lo) phonon emission and scattering by heavy holes (hh) with hh - light hole (lh) conversion are indicated. (b) A simplified cut perpendicular to the surface illustrating the three steps of the photoemission as well as the quantum levels (2D-subbands) in the band bending region. The additional well in front of the cathode results from mirror image forces on the electron.

larly effective if accompanied by heavy-hole/light-hole conversion [27]. These mechanisms are illustrated in figure 2.2 (a). At the conduction band minimum the electron ensemble thermalizes with the bulk temperature by phonon interactions. The time scale for these relaxation and thermalization mechanisms is of the order of 10^{-13} to 10^{-12} seconds and thus much shorter than the lifetime of the electrons in the conduction band, which is within the nanosecond range. The resulting diffusion length is about 3-5 μm and thus comparable to the absorption length, leading to a high probability for an electron excited with front-side illumination (reflection mode operation) to reach the surface. The thickness of the cathode has to be adjusted accordingly in case back-side illumination (transmission mode operation) is desired.

For samples with a thickness in the μm-range, the fraction of electrons that reach the semiconductor-vacuum interface non-relaxed and non-thermalized is negligible in the case of transmission mode operation, or reflection mode operation with infrared light. This fraction can, in contrast, be considerable with shorter wavelength illumination in reflection mode due to the higher absorption coefficient at increased photon energies.

The relaxation and thermalization processes the electrons undergo and the steady-state (non-equilibrium) electron energy distribution *in the bulk* for dc illumination are well understood. They can, for example, be determined very accurately by measuring the photoluminescence of recombining (hot) electrons [27, 28], since this method is rather insensitive to the influence of the semiconductor-vacuum interface. The distribution for the case of photon energies slightly exceeding the band gap very well follows the multiplied density of stated ($\propto \sqrt{E - E_{cb}}$) with the Boltzmann-distribution (note that the CBM is far from the Fermi level). It is furthermore isotropic due to the parabolic nature of the conduction band in the vicinity of the Γ-point [28].

2.3 The semiconductor-vacuum interface and the emission process

To escape into vacuum the electrons have to cross the semiconductor-vacuum interface. Depending on the parameters of the preparation process, in particular the annealing temperature of the crystal prior to activation, the initial GaAs(100) surface shows several distinct reconstructions [29, 30]. The influence of these different initial reconstructions on the photoelectron energy distributions was, probably because of the difficulty to access this parameter, never systematically investigated. For the next generation of experiments regarding the photoemission from NEA-GaAs it is, nevertheless, advisable to control this

parameter since the electronical and geometrical conditions at the surface (e.g. surface states, shape and height of the tunneling barrier) certainly depend on the surface reconstruction.

The current knowledge of this, still not well understood, final step of photoemission from NEA-GaAs is in particular derived from studies of the energy distributions of the photoelectrons.

2.3.1 Longitudinal photoelectron energies

General structure of longitudinal photoelectron energy distribution curves

Figure 2.3 reproduces [31] a comparison of the calculated electron energy distribution in the bulk with experimental results obtained on the distribution of longitudinal photoelectron energies, i.e. the energy corresponding to the photoelectron momentum perpendicular to the surface. The percentages indicated are the values of the quantum yield (QY), a measure of the photocathode efficiency; it is defined as the ratio of emitted electron per incident photon. The intensity of the high energy slope of the measured spectra is about two orders of magnitude lower than the respective intensity of the electron energy distribution in the bulk. The high-energy wing above the position of the conduction band minimum is in good approximation exponential. This indicates that a longitudinally thermalized photoelectron ensemble can be obtained if only this part of the distribution is extracted. The temperature corresponding to the slope of the exponential tail is usually observed to be slightly (few meV) higher than the bulk temperature. The reason for this increased temperature is not understood up to now, a slight influence of the initial electron energy on the transmission of the tunneling barrier at the surface might, however, be contributing. This behavior was also observed at cryogenic cathode temperatures [32, 4]. The three different experimental curves are recorded for different steps of the activation, resulting in different values of χ_{eff} (E_{cb}-E_{vac}). It turns out that the integral current increases due to an extension of the spectra to the respective vacuum level; the high energy tail remains in good approximation constant.

The appearance of this low longitudinal energy shoulder (below CBM) raised particular interest. It was attributed to electron energy losses since the initial energy of the electrons (in the bulk) is about $|\chi_{eff}| + k_B T$ (see figure 2.1). The known energy loss mechanisms in the band bending region are not effective enough to explain an electron energy loss of this order. Multiple reflections of the electrons in the band bending region [33] and temporal trapping of electrons in surface states [31] were thus proposed to account for these suspected electron energy losses. The spectra of longitudinal photoelectron energy alone do, however, not provide information sufficient to address to this question: The contribu-

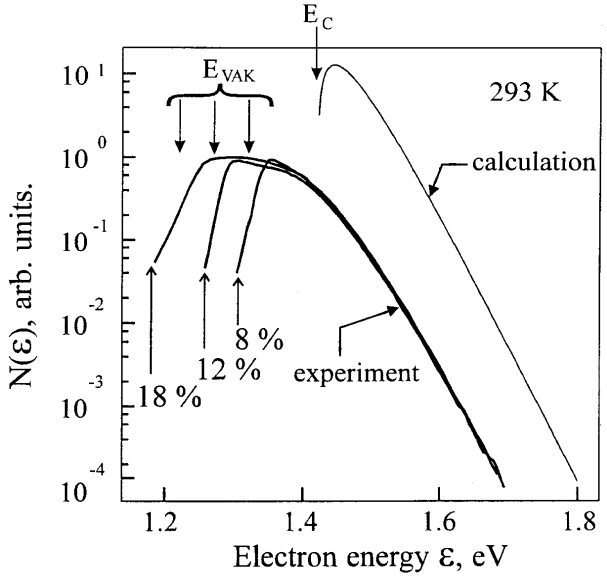

Figure 2.3: Demonstration [31] of the difference of the calculated electron energy distribution in the bulk and the longitudinal energy distribution curves measured at different steps of the activation. The energy scale is referred to the Fermi level. E_C and E_{VAK} indicate the position of the conduction band minimum and the vacuum level, respectively. The percentages denote the values of the quantum yield.

tion of electrons at low longitudinal energies might also be explained by elastic scattering in the semiconductor-vacuum interface and thus a transfer of longitudinal energy to the transverse degree of freedom.

Signatures of the band structure in the longitudinal energy distribution

A longitudinal energy spectrum of photoelectrons measured in reflection mode with a photon energy considerably exceeding the band gap energy is reproduced in figure 2.4 [4]. A strong feature starting at and extending below the CBM (denoted as Γ) is attributed to the emission of electrons which thermalized and relaxed in the bulk. Some peculiarities appear at higher energies: The initial energies of the excited electrons for excitation with the given laser wavelength from both the heavy-hole and light-hole bands, respectively, show up besides a shoulder attributed to the L-minimum of the conduction band minimum (see also figure 2.2). These peculiarities are broadened due to interaction with phonons [4, 27], due to the anisotropic nature of the valence bands and of course due to the limited resolution of the system used for energy analysis. Due to the higher density of states in the two additional conduction band minima (L and X), electrons with sufficient energy are effectively accumulated in these minima. For an ideal GaAs(100)-surface the direct emission from this valley should be forbidden for symmetry reasons [2]. It is thus not clear

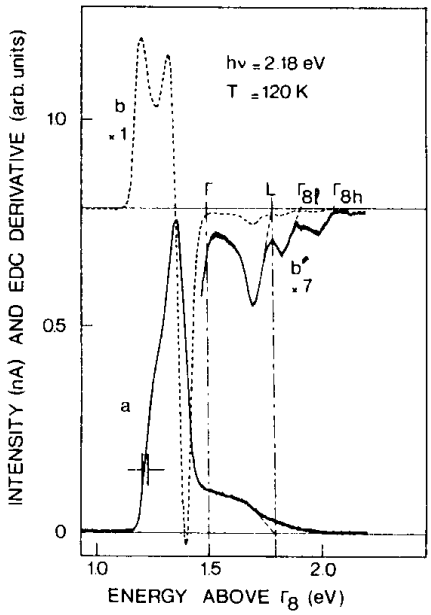

Figure 2.4: Longitudinal energy distribution curve (a) and its derivative (b) of photoemitted electrons from NEA-GaAs under illumination with a photon energy significantly exceeding the band gap [4]. The energy scale is referred to the valence band maximum. Structures assigned to the conduction band minimum (Γ), a side valley of the conduction band (L) and the initial energies of the electrons excited from the light-hole band (Γ_{8l}) and the heavy-hole band (Γ_{8h}) are denoted in the figure.

if the observed feature L appears due to a disturbance of the surface symmetry (e.g. by the activation layer) or as a result of electrons backscattered to the Γ-valley after relaxing in the L-minimum.

Since the band structure of bulk GaAs is well known [19], these features can be used to calibrate the absolute energy scale in the measurements of the energy distributions of photoelectrons from NEA-GaAs, as was demonstrated in [4].

Emission from 2D-subbands in the band bending region

The small dimensions of the potential well in the band bending region give rise to a quantization of longitudinal electron energy and thus to the formation of two-dimensional quantized subbands (see figure 2.2). Experimental evidence for the influence of these bands on the photoemission from NEA-GaAs could recently be provided [34]. Spectra of longitudinal photoelectron energy distributions recorded at liquid helium temperatures showed peaks at an energy well corresponding to the calculated position of the highest of these levels. Additional structures down-shifted by multiples of an energy of about 37 meV indicate the presence of longitudinal-optical phonon emission and thus of pro-

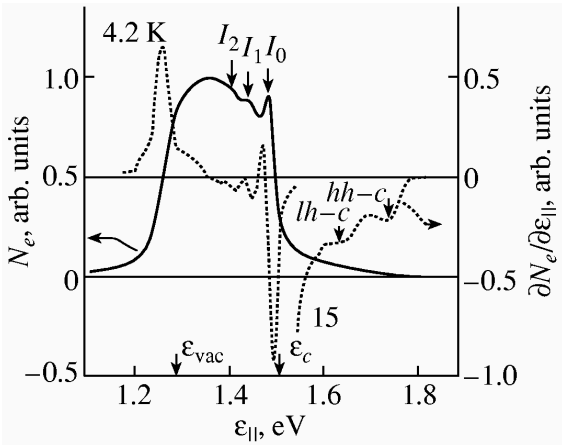

Figure 2.5: Longitudinal energy distribution curve (solid line) of photoelectrons from NEA-GaAs recorded at liquid helium temperature [34]. The energy scale is referred to the Fermi level, the position of the vacuum level and the conduction band minimum are denoted by ε_{vac} and ε_c, respectively. The strong feature I_0 is assigned to the emission from a two-dimensional quantized subband in the band bending region. I_1 and I_2 are separated by about the energy of longitudinal-optical phonons in the bulk and thus interpreted as phonon replica of I_0. The derivative (dotted curve) shows peculiarities resulting from the electron excitation from the light-hole band (lh-c) and the heavy hole band (hh-c) to the conduction band.

cesses accompanied by electron energy loss during the emission process. At liquid nitrogen temperature, probably due to thermal spreads, only slight peculiarities of the corresponding type could be resolved [32].

2.3.2 Transverse photoelectron energies

The two-dimensional translational symmetry in the plane parallel to the surface of a perfect semiconductor-vacuum interface should lead to a conservation of the respective electron momentum during the emission [2]. In the case of NEA-GaAs, the transverse momentum should be decreased by a factor of about 15 due to the small effective electron mass in the Γ-minimum of GaAs (about 0.07 of the free electron mass). This so-called 'effective-mass effect' thus would lead to transverse photoelectron energies of the order of 1-2 meV with a sample kept at room temperature. Experiments performed until the beginning of the 1990s, however [35, 36, 37, 38, 39], showed mean transverse energies

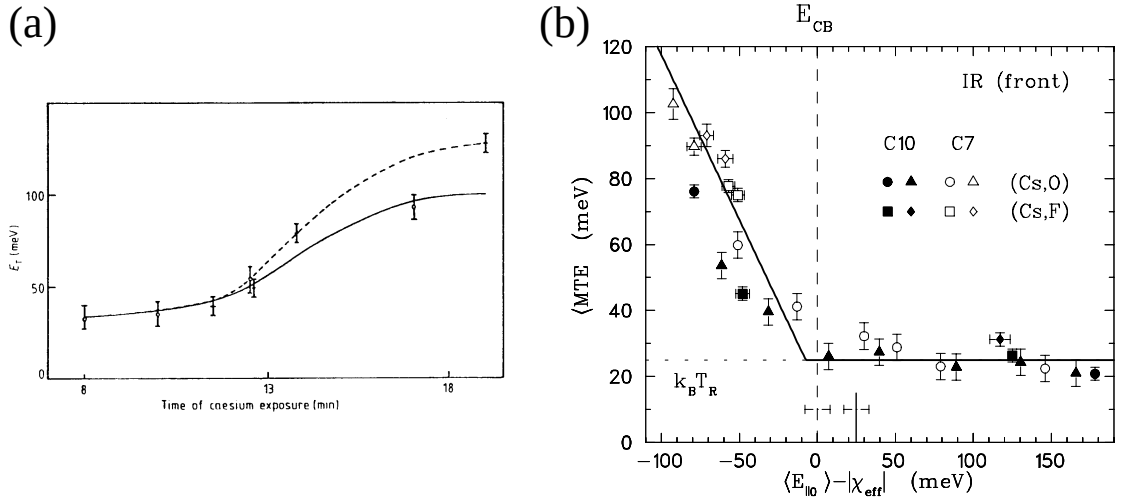

Figure 2.6: Measured mean transverse energies (E_T resp. MTE) of photoelectrons from NEA-GaAs: (a) as a function of activation layer thickness [36] (the line represents the data for the (100)-surface orientation while the dashed curve is measured for a (110)-surface) and (b) for different subensembles of the total electron yield, defined by a certain minimum longitudinal energy, plotted as a function of mean longitudinal emission energy $\langle E_{\parallel 0} \rangle$ [13]. To allow for an easy comparison, the longitudinal energy is referred to the conduction band minimum. The latter data also summarizes results on different cathodes and oxidizing species applied for NEA-formation (O and F).

between 30 meV and 100 meV for cathodes activated for maximum quantum yield[2]. In all of these studies the mean transverse energy was measured for the complete photoelectron yield by evaluating the transverse spread of a dilute photoelectron beam produced by the illumination of a small spot on the photocathode.

The systematic study of the transverse energy as a function of the activation performed by Rodway and Allenson [36] showed an increase of MTE in the course of activation (see figure 2.6 (a)). It was interpreted as a result of a strongly scattering (Cs,O) activation layer.

An azimuthal asymmetry in the photoelectron yield was not observed in any of these studies.

In the middle of the 1990s another study [12, 13, 14] was carried out by Pastuszka et al. at the Max-Planck-Institut für Kernphysik in Heidelberg, in which the MTE was measured

[2]To be precise, one report [40] claims the observation of the effective mass effect. These results were, however, never reproduced and later attributed [35] to systematic errors caused by the unfavorable electric field configuration for measuring the low energy of these photoelectrons in the used LEED-Auger angular energy analyzer.

employing the principle of adiabatic transverse expansion (see chapters 3.1.2 and 5.3) of a magnetized electron beam. The set-up constructed for this purpose also served for the experiments reported in this thesis and is thus described in detail in later chapters. The experimental arrangement in particular permits the controlled exclusion of low longitudinal energy parts of the initial photoelectron beam from the measurement by applying a properly tuned potential barrier. It thus enables the investigation of the transverse energy spreads of different subensembles (characterized by their mean longitudinal energy MLE) of the electrons photoemitted from fully activated samples.

A summary of the results is shown in figure 2.6 (b). They allow the conclusion that the energy distribution does *not* separate into a longitudinal and a transverse one, i.e. the transverse energy distribution is different for electron subensembles with different longitudinal energies.

The electrons with longitudinal energies above the CBM showed a MTE close to the ambient (room) temperature ($k_BT \approx$25 meV). Several experiments with cathodes cooled with liquid nitrogen showed a substantial decrease to about 14 meV. Experiments performed in the course of the present thesis showed that the cathode temperature is about 90 K ($k_BT \approx$8 meV) under these conditions. This temperature dependence and the apparent insensitivity to the applied oxidizing species allow the conclusion that the MTE of this subensemble does not mainly result from scattering by surface roughness or stoichiometric inhomogeneities, rather it seems to stem from a thermalized ensemble crossing the interface without (strong) interaction (but *without* conservation of the transverse momentum).

The largest part of the photoelectron yield, however, at lower longitudinal energies, showed enhanced transverse energies. The complete energy distribution could not be reconstructed from the data in an unequivocal way due to the limited accuracy and the absence of reliable theoretical models for the emission process. The question of electron energy loss during the emission process could thus not be accessed in detail. Nevertheless, the enhancement of transverse energies for low longitudinal energies shows that the low energy part in the longitudinal photoelectron energy spectra is not (only) a result of energy loss. Momentum scattering during the emission process and thus a transfer of longitudinal energy into the transverse degree of freedom (also) contribute strongly to the longitudinal EDC at low longitudinal electron energies. This can be seen from the fact that the increase in MTE is approximately compensating the loss in MLE if the low energy cut-off is lowered. In addition, these results allow a reinterpretation of the data reported by Rodway and Allenson, since χ_{eff} and thus the mean longitudinal energy of the complete set of photoelectrons decreases in the course of the activation.

For the production of transversely cold electron beams the same conclusions as for the longitudinal case were drawn, i.e. measures should be taken to extract only electrons with longitudinal energies above the conduction band minimum.

Recent theoretical approaches based on Monte Carlo simulations of different kinds of scattering in the (Cs,O) activation layer [41, 42] could not reproduce the measured transverse energy distributions. Lowest discrepancies were obtained in the case of assuming the 'same' effective electron mass inside the bulk and in vacuum, but also in this case the deviations from the experimental data were considerable. These authors furthermore concluded that a model, in which a part of the electrons which pass the interface undergo scattering while others do not interact at all, is not an adequate description of the emission process.

2.4 Practical limits of the application of NEA-GaAs photocathodes

Photocathode degradation

GaAs-photocathodes are activated to the state of NEA by depositing as little as a few monolayers of cesium and an oxidizing species onto the surface. This high sensitivity also leads to a practical limitation of the usage of such cathodes: Disturbances of the optimal surface conditions lead to a dropping of the QY with time. The lifetime for NEA-GaAs photocathodes is usually given as the time until the photocurrent under constant illumination power and electron extraction conditions drops to 1/e of the initial value.

The 'dark' lifetime, which is measured with very low light intensities (and thus electron currents) is mainly limited by the composition of the residual gas: Particularly H_2O, O_2, CO_2 have harmful consequences [43]. Under favorable vacuum conditions the dark lifetime can amount to several hundred hours [12, 13, 23]. A second possible mechanism for dark lifetime limitation, a slow restructuring of an initially metastable activation layer structure thus is, if existing, of minor influence for the application of properly activated cathode.

Under high-power illumination and/or high currents, several additional processes come into play: The light illumination itself leads to a heating of the photocathode, which is potentially harmful since Cs desorption starts already at about 70°C. In addition, the excited electrons do recombine at the surface via surface states, possibly giving rise to recombination-induced chemical reactions of the activation layer. A high current drawn can, particularly at high beam energies, lead to electron stimulated desorption from the

components of the vacuum set-up. It thus leads to a deterioration of the vacuum conditions or even to a back-stream of ions which could be accelerated towards the cathode by the applied electron optics and finally be implanted into the photocathode. Results of experiments carried out at room temperature show that currents in the milliampere range can be drawn with lifetimes up to a few tens of hours in optimized vacuum conditions and configurations of electric potentials [12, 13].

The adsorption of species from the residual gas could be strongly enhanced at low temperatures, which are favorable in order to produce cold electron beams. Lifetimes in the high current regime drawn at cryogenic cathode temperatures have, however, not been reported so far.

Surface photovoltage

At moderate light intensities the maximum photocurrent is proportional to the illumination power, corresponding to a constant QY. At higher intensities this dependency is substantially sub-linear; a saturation effect characteristic for semiconductor photocathodes takes place: The slow recombination mechanisms for the fraction of excited electrons trapped by surface states lead to an accumulation of negative charge at the surface. The resulting upward shift of band bending is called the surface photovoltage (SPV) [44]. It decreases the absolute value of the negative electron affinity and thus the QY [45]. Clean, well prepared cathodes do, however, not show photovoltage effects up to illumination power densities of a few W/cm^2 [46].

Multi-mode spreadings

The longitudinal energy spreads of electron beams photoemitted from NEA-GaAs were found to be strongly increased if multi-mode lasers were employed for the illumination of the cathodes (see, e.g. [47, 48]). This effect is still not well understood. It is, however, assumed that the fast intensity fluctuations of the multi-mode lasers (mode beating) are responsible for the observed broadenings. Due to the fast response time of the NEA-GaAs the intensity fluctuations are impressed on the electron beam which, in turn, leads to strong energy relaxations and thus broadenings of the energy distribution of the electron beams [48, 49]. This problem is usually circumvented by employing single-mode lasers for the cathode illumination.

3. Magnetized electron beams

This chapter concerns magnetized electron beams and the measurement of their energy distributions. The concepts of magnetized electron beams are introduced in section 3.1. After a motivation of the usage of a magnetic guiding field, temperature definitions for the decoupled degrees of freedom are given. The principle of adiabatic transverse expansion, which is employed in the measurements of transverse electron energies, is introduced in section 3.1.2. Section 3.2 concerns the possibilities to measure the energy distributions of a magnetized electron beam and to deduce the corresponding source specific values. Section 3.3 discusses beam relaxation effects, which could influence the energy distributions of the electron beam and thus lead to deviations of the measured energy distributions from the initial, source specific ones.

3.1 Concepts of magnetized electron beams

3.1.1 Magnetic confinement and temperature definitions

The divergence of an electron beam due to the Coulomb repulsion of the particles from their common space charge can be suppressed by a longitudinal (z-direction) magnetic guiding field B_z, if the strength of the latter exceeds the so-called *Brillouin*-field [8]:

$$B_B = \sqrt{\frac{2n_e \cdot m_e}{\epsilon_0}}, \tag{3.1}$$

where n_e denotes the electron density. For the electron densities used in this thesis, B_B is of the order of a few Gauss, whereas the magnetic guiding field amounts to several hundred Gauss.

This strong magnetic guiding field in addition leads to a decoupling of the longitudinal from the transverse degrees of freedom [8], such that beam temperatures can be given for the respective directions, defined through the standard deviations of the respective kinetic particle energy (at a given z-position):

$$\frac{1}{2}k_B T_\parallel = \frac{1}{2}m_e\Big(\langle v_\parallel^2\rangle - \langle v_\parallel\rangle^2\Big) \tag{3.2}$$

and

$$k_B T_\perp = \frac{1}{2}m_e\Big(\langle v_\perp^2\rangle - |\langle \vec{v}_\perp\rangle|^2\Big). \tag{3.3}$$

The mean transverse velocity vanishes in the beam center, consequently the transverse temperature directly equals the mean transverse energy (MTE)

$$\langle E_\perp\rangle = \frac{1}{2}m_e\langle v_\perp^2\rangle. \tag{3.4}$$

In the beam rest frame (denoted by the index $'$) the mean longitudinal energy vanishes ($\langle v_\parallel'\rangle = 0$), so that

$$\frac{1}{2}k_B T_\parallel = \langle E_\parallel'\rangle. \tag{3.5}$$

An acceleration of the electron beam leads to a reduction of the longitudinal beam temperature in the beam rest frame. For non-relativistic velocities, this is described by the kinematic transformation:

$$\frac{1}{2}k_B T_\parallel = \frac{(\Delta E_\parallel)^2}{4\langle E_\parallel\rangle}. \tag{3.6}$$

The transverse temperature is, however, unaffected by the acceleration:

$$k_B T_\perp = \langle E_\perp\rangle = \langle E_\perp'\rangle. \tag{3.7}$$

3.1.2 Adiabatic transverse expansion

If an electron is passing through a region of spatially varying magnetic field strength, the Lorentz force $\mathbf{F}_L$ also has a component in the longitudinal direction; the electron is accelerated longitudinally. Since $\mathbf{F}_L \perp \mathbf{v}$ energy conservation holds:

$$E_{total} = E_\parallel + E_\perp = const., \tag{3.8}$$

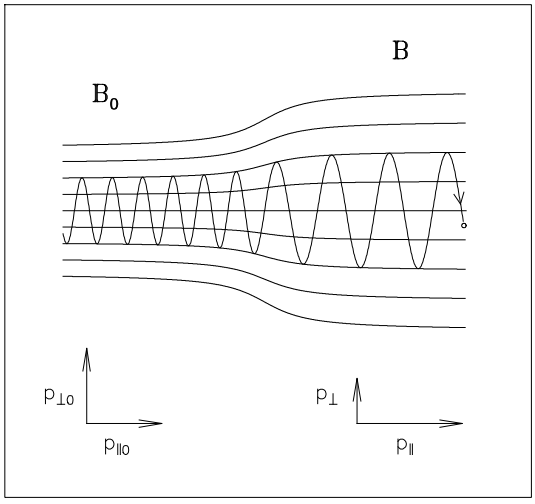

Figure 3.1: Sketch of the transit of an electron through a region with decreasing longitudinal magnetic guiding field and of the resulting changes of the momenta corresponding to the longitudinal and transverse degree of freedom, respectively.

i.e. the increase (decrease) of longitudinal energy is accompanied by a decrease (increase) of transverse energy. This is schematically shown in figure 3.1.

For a sufficiently slow (adiabatic) passage of this region of varying field

$$\frac{E_\perp}{B} = const. \tag{3.9}$$

is an adiabatic invariant [50]. The passage is called adiabatic if the adiabacity parameter ξ, defined as the relative change of magnetic field in the longitudinal extension of a cyclotron revolution λ_c:

$$\xi = \frac{\lambda_c}{B} \cdot \left|\frac{dB}{dz}\right| \quad \text{with } \lambda_c = \frac{2\pi}{eB} \cdot \sqrt{2m_e E_\parallel} \tag{3.10}$$

is small compared to unity. For an adiabatic passage from the initial longitudinal field B_i to the final longitudinal field B_f, the final longitudinal energy $E_{\parallel f}$ is given as a function of the initial energies $E_{\parallel i}$ and $E_{\perp i}$ by energy conservation to

$$E_{\parallel f} = E_{\parallel i} + (1-\alpha)\, E_{\perp i} \tag{3.11}$$

where the expansion parameter α denotes the ratio of final and initial longitudinal field strength:

$$\alpha = \frac{B_f}{B_i}. \tag{3.12}$$

For a dense electron ensemble the single electron approximation does not hold, since the electrons interact via the Coulomb force. It can, however, be shown [51] that

$$\frac{\langle E_\perp \rangle}{B} = const. \tag{3.13}$$

stays an adiabatic invariant for a strongly magnetized electron ensemble.

This holds as long as relaxation effects (see section 3.3) can be neglected: $\frac{\langle E_\perp \rangle}{B}$ as an adiabatic invariant is *not* a constant of the motion, it rather changes exponentially slow.

An additional adiabatic invariant is given by

$$R^2 \cdot B = const., \tag{3.14}$$

with R denoting the electron beam radius. Hence a spatial increase of the magnetic field strength leads to a decrease of the beam diameter. This process is thus called adiabatic transverse compression. The opposite case, expansion, is obviously achieved by a spatially decreasing magnetic guiding field.

3.2 Energy distributions and measurement principles

In the general case (neglecting azimuthal asymmetries) the two-dimensional energy distribution of an electron beam can be written as

$$N(E_\parallel, E_\perp). \tag{3.15}$$

All distributions are assumed to be normalized to an integrated value of unity for the following discussion. The longitudinal energy distribution

$$N_\parallel(E_\parallel) = \int_0^\infty dE_\perp \cdot N(E_\parallel, E_\perp) \tag{3.16}$$

of a magnetized electron beam can be accessed via a retarding field method. The current which is still able to overcome a potential barrier of the height $e \cdot U_{ret}$, with U_{ret} denoting the retarding voltage, amounts to the retarding curve $I(U_{ret})$:

$$I(U_{ret}) = I_t \cdot \int_{e \cdot U_{ret}}^\infty dE_\parallel \cdot N_\parallel^m(E_\parallel), \tag{3.17}$$

where $N_\parallel^m(E_\parallel)$ denotes the measured longitudinal energy distribution and I_t the total electron current. The longitudinal energy distribution curve (EDC) is thus yielded by a differentiation of $I(U_{ret})$:

$$\frac{dI(U_{ret})}{dU_{ret}} = -I_t \cdot N_\parallel^m(E_\parallel). \tag{3.18}$$

This measurement reverses, due to the deceleration, the kinematic transformation of the acceleration, such that the initial longitudinal energy spread is measured in the case of negligible beam relaxations.

The measured longitudinal energy distribution of the accelerated electron beam $N_\parallel^m(E_\parallel)$ is connected to the initial longitudinal energy distribution of the emitted electrons $N(E_\parallel)$ by

$$N_\parallel^m(E_\parallel) = N_\parallel(E_\parallel - e \cdot (U_a - U_{off})), \tag{3.19}$$

where U_a is the acceleration voltage and U_{off} is an offset voltage caused by the different work functions of the cathode and the analyzer and, in addition, by the a-priori unknown deviation of the *effective* retarding potential from the applied retarding voltage (see section 5.1, pages 46f).

Mean transverse energy

Since the transverse motion of the electrons is, due to the magnetic guiding field, as a mean undirected, it cannot be accessed by a retarding field method. In addition, a strong magnetic guiding field suppresses the divergence of the electron beam, such that a beam projection on a position sensitive device does not allow one to calculate the initial mean transverse energies.

The principle of adiabatic transverse expansion, however, allows to transfer a specific amount of energy between the degrees of freedom (formula 3.11). This can be applied to measure the initial transverse energy of an electron by determining the shift of longitudinal energy upon beam expansions with different α:

$$E_{\perp i} = -\frac{dE_{\parallel f}}{d\alpha}. \tag{3.20}$$

In case of an electron ensemble, it still allows the measurement of the initial mean transverse energy, as long as relaxation effects (see section 3.3) can be neglected :

$$\langle E_{\perp i} \rangle = -\frac{d\langle E_{\parallel f} \rangle}{d\alpha}. \tag{3.21}$$

This method was first applied by Pastuszka et al. [15], who tested it on the well known energy distribution of thermionically emitted electrons and later applied it to the measurement of the mean transverse energy of electrons photoemitted from NEA-GaAs [12, 13].

However, in cases like photoemission from NEA-GaAs, the distribution of the electron energies $N(E_\parallel, E_\perp)$ does not factorize into $N_\parallel(E_\parallel)$ and $N_\perp(E_\perp)$: Not only the mean of the longitudinal energy distribution changes due to expansion, but also its higher moments do, reflecting the fact that the transverse energy distributions vary for subsets with different longitudinal energies. The reconstruction of the initial energy distribution is, in such a case, tedious (if not impossible), particularly if no reliable (semiquantitative) model of the energy spreads exists, as is the case for photoemission from NEA-GaAs up to now.

The differential transverse energy distribution for fixed longitudinal energy

The marking of electrons within a narrow interval of longitudinal energies prior to the expansion permits, in the limit of negligible electron interactions, the analysis of the effect of expansion on this particular subensemble of the electron beam.

The ideal case of δ-like marking is discussed in this section in order to clarify the principle; the practical application is described in chapter 5.4. The energy distribution $N(E_\parallel^b, E_\perp)$ of an electron subensemble with fixed longitudinal energy $E_\parallel^b$ is given by

$$N(E_{\parallel}^{b}, E_{\perp}) = \int dE'_{\parallel} \cdot N(E'_{\parallel}, E_{\perp}) \cdot \delta(E'_{\parallel} - E_{\parallel}^{b}). \tag{3.22}$$

Upon adiabatic transverse expansion, all electrons of the marked subensemble will undergo a shift in longitudinal energy according to equation 3.11, such that $E_{\parallel f} = E_{\parallel}^{b} + (1-\alpha) \cdot E_{\perp i}$. Hence the longitudinal energy distribution after expansion is given by

$$N_f(E_{\parallel}) = N_{\perp i}(E_{\parallel}^{b}, \frac{E_{\parallel} - E_{\parallel}^{b}}{1-\alpha}), \tag{3.23}$$

i.e. it is a transformation of the distribution of initial transverse energies within the marked subensemble.

Re-transformation by

$$E_{\perp i} = \frac{E_{\parallel} - E_{\parallel}^{b}}{1-\alpha} \tag{3.24}$$

yields the distribution of initial transverse energies $N_{\perp}(E_{\parallel}^{b}, E_{\perp})$ for electrons with the longitudinal energy $E_{\parallel i} = E_{\parallel}^{b}$.

3.3 Relaxations

The Coulomb interaction of the electrons contributing to the beam can lead to substantial modifications of the ideal case of negligible electron density discussed in the preceding sections. The important processes can be separated into longitudinal-longitudinal relaxations (LLR) and transverse-longitudinal relaxations (TLR) [16].
The longitudinal temperature $T_{\parallel}^{r}$ after the relaxation is enhanced by two terms:

$$\frac{1}{2} k_B T_{\parallel}^{r} = \langle E'_{\parallel} \rangle^{r} = \langle E'_{\parallel} \rangle + \delta E_{\parallel}^{\prime TLR} + \delta E_{\parallel}^{\prime LLR}. \tag{3.25}$$

Also the width of the longitudinal energy distribution measured by the retarding method is affected [12]:

$$\Delta E_{\parallel}^{r} = \sqrt{(\Delta E_{\parallel i})^2 + (1-\alpha)^2 \ (\Delta E_{\perp i})^2 + 4 \langle E_{\parallel} \rangle \ \delta E'^{\,r}_{\parallel \alpha}}. \tag{3.26}$$

Longitudinal-longitudinal relaxations

The acceleration leads to a non-equilibrium state of the electron beam: Hence the electrons tend to minimize their potential energy. The excess potential energy is converted into kinetic energy; the electron beam is longitudinally heated, leading to an increase of the longitudinal beam temperature of [8, 16]:

$$\delta E_{\parallel}'^{LLR} = \frac{1}{2} \cdot C \cdot \frac{e^2 n_e^{1/3}}{4\pi\epsilon_0}. \tag{3.27}$$

The dependency of this term on the particular mode of acceleration is quantified by the value of C which is of the order of one.

Transverse-longitudinal relaxation

Anisotropic energy distributions, particularly present after longitudinal acceleration of an initially isotropic distribution, tend to equilibrate. The process is called transverse-longitudinal relaxation (TLR) and is mediated through binary collisions of the electrons [52].

Since the longitudinal temperature is, due to the beam acceleration, lowered, this process leads to a heating of the beam in the longitudinal degree of freedom, whereas the transverse temperature is decreased. This effect may thus lead to an underestimation of the initial transverse electron temperature.

Experimental data for the case of strong anisotropies (as in an accelerated beam) is scarce. However, TLR is increasing for increasing electron density and drift time, but can be suppressed by strong magnetic guiding fields [52].

Influences on the measurements

For the measurements of mean transverse energies in the given set-up it was shown by Pastuszka et al. that the influences of the stated relaxation effects are already negligible for electron beams with $k_B T_{\perp i} \approx k_B T_{\parallel i} \approx$100 meV at similar acceleration conditions and magnetic field settings for current densities of about 1 mA/cm^2. The current densities used for the measurements concerning energy spreads reported in this thesis are below 2 μA/cm^2. Falsifications of the measured mean transverse energies by relaxation effect can thus be excluded.

For the measurement of $N_{\parallel}(E_{\parallel}^b)$ and $N_{\perp}(E_{\parallel}^b, E_{\parallel})$, the situation is more complicated since a small subensemble of the complete electron beam is under investigation. The measured $N_{\parallel}(E_{\parallel}^b)$ in this case were well described by a Gaussian with $\sigma_{\parallel} \approx$17 meV. A strong contribution to this width is connected with the limited resolution of the retarding field analyzer (see section 5.5). This width did not change within the range of current

densities applied in the measurements. It did also not decrease further with decreased current density. Influences of electron interactions on these measurements can thus be estimated to be lower than $\sigma_{\parallel}$.

4. Aspects of the photocathode preparation

Photoemission from NEA-GaAs is an extremely surface-sensitive process. It is thus important both for the investigation and application of the respective emitters to operate under very clean conditions and to carefully control the parameters of the multi-step cathode preparation procedure: Difficulties in reproducing and even interpreting published results are often caused by the lack of information about these parameters. In addition, contaminations of the photocathode surface could limit the performance of the cathodes, e.g. by lowering the achievable QY, by decreasing the lifetime of the activated photocathodes or by increasing the transverse energies of the emitted electrons. Hence the initial GaAs surface is directly produced in the vacuum chamber. This is accomplished in a reproducible manner by a combination of wet-chemical etching under nitrogen atmosphere and annealing in ultra-high vacuum (UHV), in which also the activation takes place.

The photocathodes and the relevant components of the vacuum set-up used in this thesis are introduced in section 4.1. Further details of the set-up have been published elsewhere [12, 13, 23]. Section 4.2 describes the applied photocathode preparation procedure.

4.1 Description of the experimental set-up

Photocathode structure

The photocathodes used in the experiments reported in this thesis were developed at the Institute of Semiconductor Physics in Novosibirsk. Figure 4.1 (a) shows a schematic cut through these emitters. They consist of a GaAs/AlGaAs double-heterostructure grown by liquid phase epitaxy. Since transmission mode operation facilitates the application of photocathodes at the new electron target, the structure is thermo-compression bonded to a transparent glass substrate. In order to further optimize the efficiency, an anti-reflection layer of silicon-oxide is included between the glass substrate and the semiconductor mate-

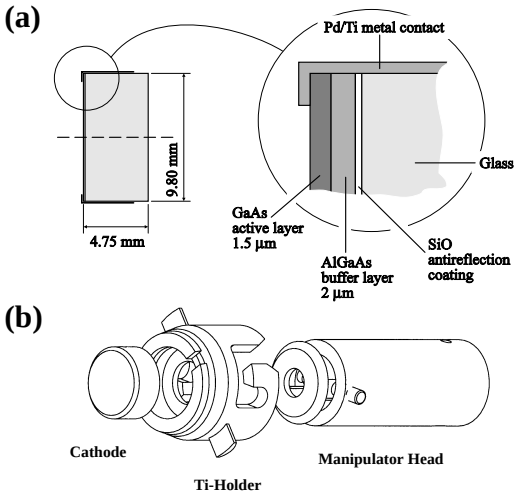

Figure 4.1: (a) Schematic cut through the photocathodes, (b) illustration of holder and manipulation concept (taken from [13]).

rial. It minimizes optical reflection losses in case of back-side illumination of the cathodes (The reflection coefficient of GaAs in the relevant wavelength range of approximately 780 nm to 650 nm is about 30%). The production principle of these devices is described in reference [53].

The active p^+- GaAs layer has a surface orientation of (100)$\pm$0.5° and a thickness of about 1.5 μm. The Zn-doping concentration is about $5{\cdot}10^{18}$ cm^{-3}. The bandgap of the AlGaAs buffer layer exceeds the bandgap of the active layer, resulting in a potential barrier avoiding the diffusion of excited carriers too far away from the surface and thus leading to a higher QY. The electron recombination rate at this additional interface is negligible for the application as photocathodes. The electrical contact is ensured by a palladium coating of both the sides of the cathodes and the outer part of the front surface.

Figure 4.1 (b) illustrates the principle used to manipulate the cathodes inside the vacuum set-up: The mounting in titanium holders via a circular spring on the latter provides mechanical fixation as well as electrical contact. The holders can be picked up by magnetically coupled manipulators employing a bayonet-joint-like design. The two wings of the holders permit the fixation of the cathodes in different positions of the vacuum set-up.

The vacuum set-up

The main chamber of the photocathode preparation system, the so-called preparation chamber (sketched in figure 4.2), is used for final heat cleaning, activation, testing and storage of the samples. It is pumped by an ion getter pump and several NEG-modules, supplying, after careful bake-out, a base pressure below 10^{-12} mbar. Figure 4.3 shows a spectrum of the residual gas composition measured with a quadrupole mass spectrometer

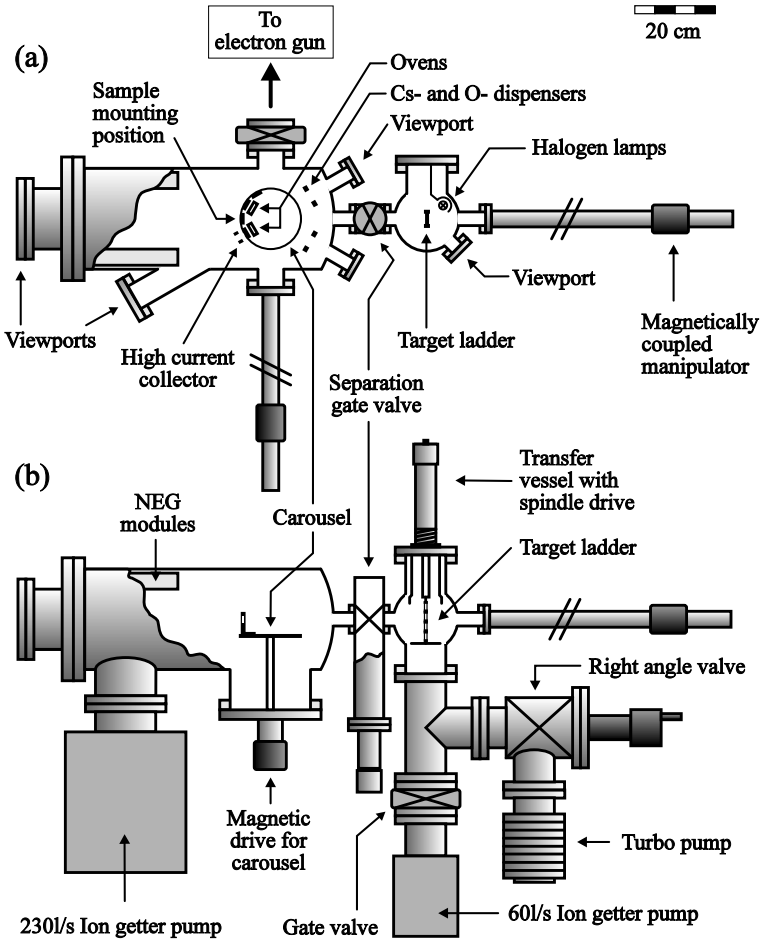

Figure 4.2: Sketch [13] of the preparation system consisting of preparation chamber, loading chamber and attached transfer vessel. This part of the set-up is separated from the gun chamber (see chapter 5.1) by an all-metal gate valve.

attached to the preparation chamber. It is dominated by hydrogen; the presence of other species, in particular the harmful H_2O and CO_2, limit the 1/e dark lifetime of activated photocathodes to typically several 100 hours.

Up to four cathodes can be stored on the carousel. The latter can be rotated such that the cathodes can be placed at different positions: Filament ovens serve for the heat cleaning by thermal irradiation from the back-side, Cs- and Oxygen-dispensers for the activation of the cathodes. A magnetically coupled manipulator permits the transfer of the samples to the gun chamber (not shown in figure 4.2, see chapter 5.1) which is separated from the preparation chamber by an all-metal gate-valve.

The 'loading chamber' serves as a load lock for the introduction (extraction) of cathodes into (from) the preparation chamber via a magnetically coupled manipulator. It is separated from the main chamber by an all-metal gate-valve. This part of the set-up is

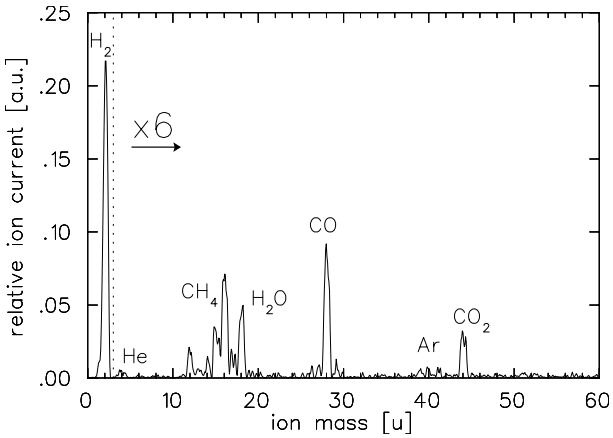

Figure 4.3: Relative ion currents measured with a quadrupole mass-spectrometer representing the residual gas composition of the preparation chamber. The data is multiplied by a factor of six for masses higher than 3 u . The total pressure was below 10^{-12} mbar.

pumped down by an turbo-molecular pump which is backed by a diaphragm pump. When the pressure reaches the 10^{-8} mbar range an ion getter pump takes over the pumping, providing a final pressure in this chamber in the 10^{-10} mbar range (without bake-out). Also in the target ladder of the transfer vessel up to four cathodes can be stored. The installed halogen lamps are used to illuminate the chamber for visual control during manipulator operation. Furthermore, they are used to heat and thus pre-clean holders and tools in vacuum before insertion into the preparation chamber. It proved disadvantageous to pre-clean the cathodes this way, probably due to a partial removal of the protecting excess As^0 layer provided by the wet-chemical treatment (see section 4.2) in combination with the relatively poor vacuum conditions in the loading chamber.

4.2 The photocathode preparation procedure

The photocathode preparation procedure is a multi-step process which can be separated into three main parts: Wet-chemical treatment, heat-cleaning and activation. Once prepared, the samples are kept in a 'closed cycle' without exposure to the laboratory atmosphere. In order to avoid uncontrolled oxidation of the cathodes, the chemical treatment is performed in a glovebox filled with pure nitrogen. A hermetic, all-metal transfer vessel filled with nitrogen serves for the transport to/from the vacuum set-up, where the heat-cleaning and the activation take place. The treatment in the glovebox is not necessary prior to every single activation of a cathode; samples which have already been activated and did undergo some degradation can be prepared for a new activation by simple heat-cleaning. Only if this procedure alone does not allow one anymore to reach a high QY

and a stable activation (after typically about five cycles), the cathodes are removed from the vacuum set-up and wet-chemically treated again.

This combined 'wet-chemical treatment and vacuum-annealing' cleaning procedure, proposed in a similar form in reference [54], can provide a surface with an atomically flat step-terrace structure extending over a macroscopic area [55] and a reproducible low contamination concentration on an atomical level [30]. The particular procedure used in the experiments reported here has recently been studied in detail [29, 30]: HCl etching removes oxides from the surface after about 10 seconds. Nevertheless, a longer time interval is advisable since a partial dissolution of $GaCl_x$ in the etching leaves behind an excess layer of As^0 (insoluble in pH<3) on the surface. The thickness of this amorphous layer depends on the etching time, two minutes being enough to yield an As^0-layer thickness that safely protects the GaAs bulk from oxidizing and carbon-contaminated species, particularly during the transfer from the glove-box to the preparation chamber. Due to the lower binding energies on As^0 compared to an adsorption on the GaAs, removing contaminations on the former is possible at lower temperatures ($\approx$ 400°C for ten minutes) and to a much higher extent [30, 29]. Roughening of the surface by thermal effects or even non-congruent evaporation due to high temperatures can thus be minimized. The resulting structural defects would not only distort the surface morphology, leading to a heating of the drawn electron beam by transverse field components [56], they would also induce surface states energetically located in the band gap [29] which can give rise to surface photovoltage effects [44] (see below).

Wet-chemical treatment and insertion into the vacuum set-up

Cathodes which are to be inserted into the closed cycle are pre-cleaned by boiling them for five minutes in toluene and Isopropanol, respectively[1]. They are kept in pure Isopropanol during the directly following transport and loading to the glove-box. The actual wet-chemical treatment consists of an etching in a solution of HCl in Isopropanol (1:60) for two minutes. The cathodes are then rinsed two times for one minute in fresh pure Isopropanol and blown dry with flowing nitrogen. All chemicals used comply with the high purity standards used in (large scale integration-) semiconductor technology.

After mounting the cathodes in the holders (which are kept under nitrogen atmosphere after pre-annealing in vacuum) and fixing them in the target ladder of the transfer ves-

[1] The etching of the emitters in a solution of H_2SO_4 in H_2O_2 and H_2O, which was routinely applied in this case in previous studies [12, 13], effectively removes GaAs from the surface. This strong etching leads to a deterioration of the surface quality and should therefore be used only in cases of *very* polluted samples [46]. Thus it was not applied for the preparation of the cathodes used in the experiments reported in this thesis.

sel, the latter is closed hermetically, detached from the load lock of the glove box and connected to the loading chamber. The nitrogen-filled transfer vessel is opened only after the pump-down provides a pressure in the 10^{-3} mbar range in the load lock. When the pressure reaches approximately 10^{-8} mbar it is possible to transfer the cathodes to the preparation chamber without medium-term deterioration of the vacuum in the latter.

Heat-cleaning

The cathodes are heat-cleaned by thermal irradiation from the filament ovens. In order to avoid thermal stress the oven power is increased slowly during approximately 40 min. The cathodes are then kept on a constant temperature of about 420°C for about 40 minutes to remove surface contaminations. If desired, a short 'jump' to higher temperatures is added at the end of the plateau in order to provide a particular surface reconstruction. The rise in pressure caused by this procedure does not exceed 10^{-9} mbar. It is only slightly lower if no cathode is installed and thus is mainly caused by a heating of the surroundings and the resulting thermal desorption. It is desirable to minimize the oven-power necessary to reach a certain temperature of the sample: Firstly, the heating of the surrounding leads to deterioration of the vacuum conditions, and secondly the lifetime of the tantalum filaments of the ovens is limited at high powers. One of the cathode fixing positions on the carousel was thus replaced by one optimized for low thermal contact.

The maximum temperature of the heat cleaning procedure not only influences the effectiveness of the photocathode cleaning but also determines the surface reconstruction of the GaAs(100)-surface. Keeping the crystal at the respective temperature for ten minutes is sufficient to provide an irreversible change in surface reconstruction [29]. In the work of Pastuszka et al. [12, 13] the cathode temperature as a function of the oven power was estimated by observing the power necessary to melt thin wires of different metals applied to a dummy cathode. This procedure allows a rough estimation of the cathode temperature. In order to better control the parameters of the initial surface a detailed calibration procedure of the cathode temperature as a function of the oven power was developed and implemented [57, 58]. This was accomplished by in-situ measurements of the band-gap energy by an analysis of the photoluminescence of the samples. The functional temperature dependence of the band-gap energy of GaAs is well established [59]. The remaining free parameters which depend on the particular device (primarily on its doping level) were determined by calibration measurements at different, well controlled temperatures. During the radiative heating of the photocathodes they are illuminated with modulated red laser light (λ=685 nm, peak power of about 50 mW). The additional heating of the photocathode resulting from the laser illumination is corrected for by measurements at different

laser powers and an extrapolation of the obtained data to zero illumination power. A set of lenses serves for the collection of light which is emitted from the cathode out of the direction of specular reflection of the incident laser beam. It is wavelength-analyzed by a monochromator, detected by a photo-diode and phase-sensitively registered employing a lock-in amplifier. The upper limit of GaAs-temperature determination by the photoluminescence technique reported in the literature (about 700 K) could be extended to 900 K. These in-situ, contact-less temperature measurements thus allow the determination of the cathode temperature in the whole relevant temperature range for GaAs photocathode preparation. The accuracy amounts to ± 15 K and is sufficient to adjust the oven power to a specific temperature interval necessary to produce a desired surface reconstruction on HCl-Isopropanol treated GaAs(100) [30]. The stated accuracy is limited by the applied calibration procedure and could hence still be enhanced by undertaking a more elaborate calibration procedure in case it showed desirable.

With the correlation of oven power and cathode temperature once established, it is only rarely necessary to perform the described calibration procedure in order to account for a degradation of the ovens or a change of the sample type.

Photocathode activation

The cathode activations were performed by means of a method similar to the so-called 'Yo-Yo'-technique [2], where cesium and oxygen are alternately deposited on the substrate. Here the Cs-exposure was kept constant, only the oxygen sources were switched on and off. The employed cesium-chromate and oxygen-peroxide dispensers permit a precise control of the exposure to the respective species and release very pure material. They are, in addition, cleaned prior to each activation by direct current flow (and thus heating) with currents higher than the ones used for the activation.

The evolution of the QY is supervised by setting the carousel (and thus the cathode) on a potential of -27 V (which proved sufficient to extract all emitted electrons) and by illuminating the sample with a modulated red laser (λ=670 nm, P$\approx$ 1 μW, ν_{mod} $\approx$29 Hz) in reflection mode. The photocurrent resulting from the laser illumination of the sample is detected by a lock-in analysis of the current flowing from the carousel to ground potential. The red laser is particularly suitable since its focus can be controlled by eye and because it allows the control of the QY also while NEA-conditions are not yet reached (and the QY thus is negligible for IR-illumination).

It also showed possible to qualitatively characterize the cathode's surface quality in the early stages of the activation, when the QY for red light is still negligible. On not optimally prepared GaAs(100)-surfaces, an increase in excited carrier density due to a pulse

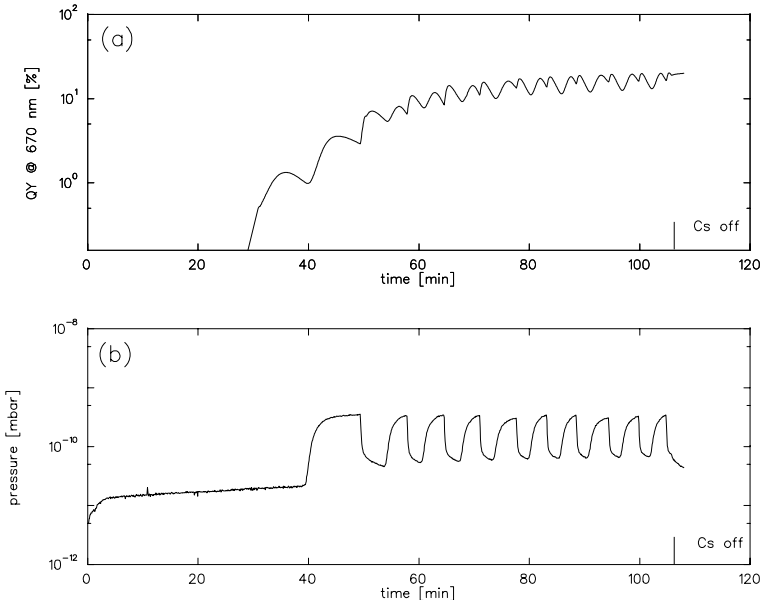

Figure 4.4: (a) Typical evolution of QY in the course of the activation and (b) the corresponding total pressure in the vacuum chamber. The time at which the current through the Cs-dispensers was set to zero is denoted by vertical lines. The final total yield at 670 nm amounted to 19%.

of the red laser can lead to surface photovoltage (SPV) an thus to an increase of the work function. The (significant) presence of this effect can be tested by phase-sensitively measuring the photocurrent from the cathode resulting from light with higher photon energies, e.g. white light from the surrounding of the set-up: Since the increase of work function is correlated with the laser pulse, the photocurrent resulting from white light is modulated with the reference frequency; it is, however, phase shifted by π.

Cathodes which showed low QY and low stability after activation indeed showed this effect. This easily performed qualitative test thus allows one to identify these cathodes prior to the activation, such that they can be marked down for wet-chemical treatment and the preparation of another cathode can be started.

Figure 4.4 shows a typical evolution of the photocurrent (a) and pressure (b) during activation of a properly prepared photocathode which did not show SPV-effects. At the beginning (t=0), the current through the cesium dispensers is switched on. The emission of cesium is rather directed and starts immediately, the rise in pressure is due to the heating of the surrounding (mainly desorbed hydrogen). The photocurrent rises, peaks and drops again (first Cs-peak). At a photocurrent of 80% of the peak value the oxygen sources are switched on. This is followed by a pressure rise (almost exclusively due to oxygen) and a peaking of the photocurrent (first oxygen-peak). The current through the

oxygen-dispensers is switched off at a photocurrent value of 85% of the respective peak value. The repetition of this procedure results in an initially strong rise of the peak values, which saturates at about three times the time of the first Cs-peak (full activation). If the activation procedure is continued even further, the peak values begin to slowly decrease (over-activation, not shown in figure 4.4). The quantum yield for full activation is usually higher for the second activation than for the first after wet-chemical treatment. This behavior was also observed in other studies [36, 12] and can be attributed to an increased removal of contaminations of the surface or, alternatively, to the creation of a favorable surface structure by the presence of Cs during the heat-cleaning. With this 'two-step activation' the QY for full activation usually was in the range of ≈18-22% (reflection mode, λ=670 nm). The higher QY observed in the same set-up before (up to 25% [12, 13]) were obtained after heat-cleaning a cathode activated with NF_3 as oxidizing species and can thus be attributed to additional surface cleaning in the presence of fluorine.

The activation layer thickness can not be accessed directly in the described set-up. Other studies [60], however, showed a linear increase of the thickness with the time of Cs-exposure, the time of the first Cs-peak corresponding to 'half a monolayer' [2].

[2]The term 'monolayer' is, in this context, to be understood as a unit of coverage rather than of thickness.

5. Energy analysis of electron beams

This chapter describes and characterizes the experimental techniques applied for the high accuracy measurements of longitudinal and transverse energy distributions of electron beams photoemitted from NEA-GaAs. The relevant components of the experimental set-up are introduced in section 5.1. The measurements of longitudinal electron distributions are discussed in section 5.2; it also includes a description of the calibration procedure for the longitudinal energy scale. The improvements of the measurement of the mean transverse energy of electron beams, which enable systematic studies at cryogenic cathode temperatures and the resulting low energy spreads, are described in section 5.3. The topic of section 5.4 is the new differential method, by which the transverse energy distribution of a well-defined subensemble of the electron beam, characterized by a narrow interval of longitudinal energies, can be measured. Resolutions and accuracies are discussed in section 5.5.

5.1 Description of the experimental set-up

The 'gun chamber', schematically shown in figure 5.1, was designed by Pastuszka et al. [12, 13] for the analysis of the initial, source specific energy spreads of magnetized electron beams. The electron beam is extracted from the cathode, accelerated and guided to a retarding field analyzer by a variable axial magnetic field (z-direction).

Two ion-getter pumps and two NEG-modules provide a base pressure in the low 10^{-11} mbar range. Viewports allow the illumination of the cathodes from the front (reflection mode) as well as from the back (transmission mode)[1]. All measurements of energy spreads of photoelectron beams reported in this thesis were performed under illumination with single-mode lasers in reflection mode. In the following paragraphs the important components for the experiments of this thesis are described, further details have been published elsewhere [13, 12].

[1] A prism installed on a linear motion feedthrough serves for the feasibility of the latter option.

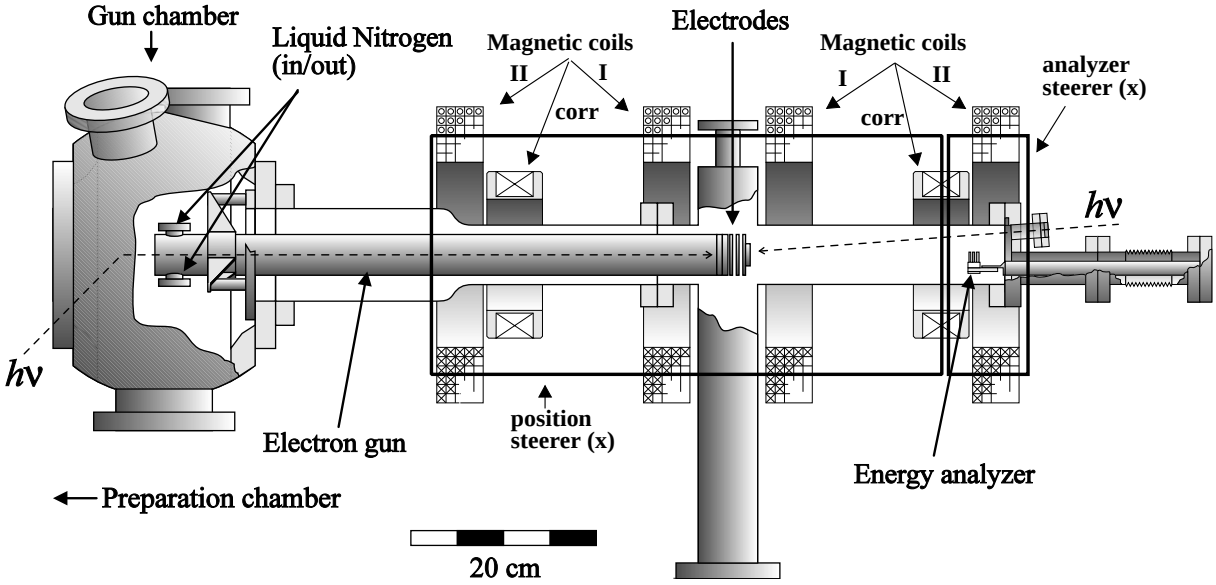

Figure 5.1: Sketch of the gun chamber including the vacuum system and the magnetic coil arrangement (adapted from [13]). The flat solenoid coils are driven in pairs (denoted as I, II and corr). The extensions of the analyzer steerers and the position steerers (both only for the x-direction) are delineated by rectangles. The pumping sections are not shown; they are attached to the two flanges below.

Magnetic guiding field

The cathode is positioned in the inversion center of a symmetric three-pair coil arrangement. The inner pair (pair I) has Helmholtz configuration to ensure the homogeneity of the field at the cathode as well as in the acceleration region, while the outer pair (pair II) provides the main part of the desired field strength in the analyzer region. The smaller correction coils are necessary since the magnetic field at the analyzer position must be homogeneous also for different expansion parameters. In the opposite case energy transfer from the longitudinal to the transverse degree of freedom would lead to systematic falsifications of longitudinal electron energies measured by the retarding field analyzer. The additional steerer coils are discussed in section 5.3.2.

Cooling system

The cathode mounting assembly is connected to a double-walled tube (see figures 5.1 and 5.2). The space within the walls can be filled with liquid nitrogen. The cooling is usually started with the cathode already installed, reaching the lowest temperature after about two hours. In the course of the experiments realized for this thesis, the cooling system proved insufficient for the operation under cw-illuminations of a power of the order of 1 W,

necessary to produce *cold* continuous electron beam currents in the milliampere range[2]. A quantum yield spectroscopy technique was implemented to in-situ supervise the cathode temperature [57]: For NEA-devices, a sharp onset of photoemission is observed if the photon energy reaches the energy of the band gap. The change of the respective photon energy with changed sample temperature, obtained by an illumination of the cathode with monochromatic light and recording the quantum yield as a function of the illumination-wavelength, coincides with the well understood temperature variation of the band gap [19]. Consequently, the absolute crystal temperature could, after additional calibrations of the device dependent parameters, be determined with an accuracy of ± 3 K. A detailed calibration at low temperatures has not been performed yet. However, the temperature during continuous operation at the illumination powers used for the experiments reported in this thesis (few ten milliwatt) could be estimated to be about 90 K.

The reliable operation of the photocathodes as sources of cold electron beams requires a high flexibility of the cathode fixing system in the gun position. Furthermore, due to constructional constraints of the new electron target for the TSR, transmission mode illumination would be of great advantage for the planned photocathode application. These requirements, however, contradict directly the pre-requisite of good thermal contact. Work towards a system satisfying both requirements is in progress [61, 57].

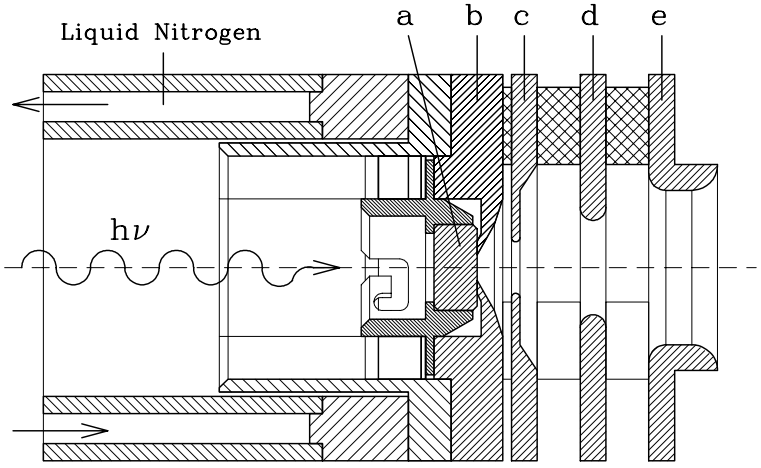

Figure 5.2: Sketch of the acceleration region [13]: (a) photocathode, (b) Pierce electrode, (c) extraction electrode. The outer electrodes (d) and (e) are grounded.

[2]The *effective* quantum yield is, for this application, strongly reduced compared to the possible overall yield since a large fraction of the emitted electron ensemble must be filtered out from the beam (see chapter 2.3).

Acceleration region

Figure 5.2 illustrates the electron extraction- and acceleration-region. All electrodes are characterized by a rotational symmetry. In order to minimize field distortions resulting from chemisorbed and physisorbed residual gas components, all electrodes are gold plated, taking advantage of the low binding energies of adsorbates on the noble metal. Nevertheless, heat-cleaning this area with an infrared laser of a power of about 1 W for several minutes prior to the installation of a cathode proved advantageous to achieve low transverse energy spreads of the electron beams. This stresses the importance of clean electrodes for an optimum field configuration in the extraction region.

The installed photocathode is pressed to a Pierce shield by a spring mechanism. The hole of this electrode restricts the effective cathode region to a circular spot with a diameter of 3 mm. The special design of the Pierce electrode simulates, for space charge limited emission, the equipotential lines of an infinitely extended cathode and space charge cloud in the x-y-plane [62]. Consequently, transverse electric field components vanish due to symmetry reasons. These components would cause a transverse acceleration and thus a transverse heating of the drawn electron ensemble. Cathode (a) and Pierce shield (b) are set on the acceleration potential U_a, the outer electrode (e) is grounded. The remaining electrodes (c) and (d) can be set on an intermediate potential to apply a specific extraction potential and to allow a 'slow' acceleration. In the experiments reported in this thesis electrode (d) was kept on ground potential, since at the applied acceleration voltages and current densities longitudinal-longitudinal relaxations could be neglected (see chapter 3.3). Furthermore, numerical simulations [12] showed that transverse heating of the electron beam in the beam center is negligible under these conditions (in the given set-up) also in the case of current limited emission. The extraction voltage is defined as $U_{extr} = U_c - U_a$.

In this particular set-up, however, the potential situation differs from the ideal Pierce conditions: Different work functions of the cathode and the Pierce shield ($\varphi \approx 1.2$ eV for NEA-GaAs and $\varphi \approx 5.1$ eV for gold) lead to contact potentials and thus electric fields (schematically shown in figure 5.3). In the longitudinal direction these fields lead to an additional potential barrier in front of the cathode, in particular if low extraction voltages are applied (see figure 5.4).
Since the potential barrier radially increases, the beam profile evolves from an almost rectangular one to a sharp Gaussian-like when the extraction voltage is decreased. Only a subensemble of the electrons emitted from the cathode, defined by a r-dependent minimum longitudinal energy, is thus accelerated and, eventually after expansion in the variable magnetic field, detected by the retarding field analyzer.

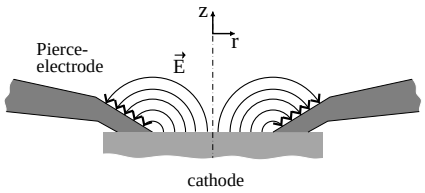

Figure 5.3: Schematic representation of the electric field caused by the different work functions (contact potential) of the cathode and the Pierce electrode.

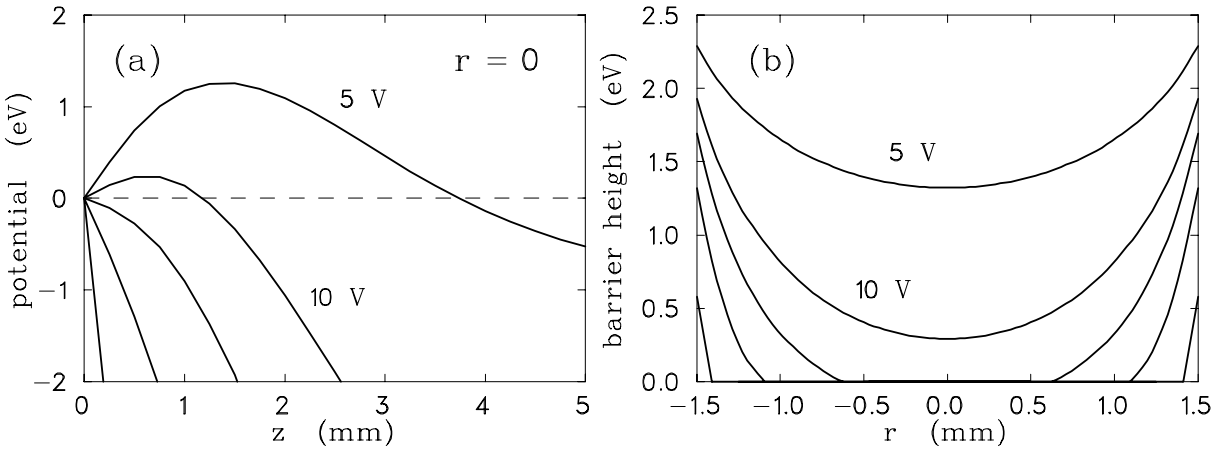

Figure 5.4: Calculated potentials in front of the photocathode for different applied extraction voltages [12]: (a) in z-direction on the symmetry axis (r=0) and (b) maximum of the potential barrier as a function of r (cutting potential).

It should be stated here that this 'cutting' is not ideal, i.e. the potential barrier slightly influences the high energy ($E_{\parallel} > e \cdot \Phi^b$) part of the energy distribution. This effect is discussed below. Nevertheless, it is small such that the potential barrier is assumed to act effectively as an achromatic energy filter, blocking (cutting) electrons with a longitudinal energy below the barrier height. This process is illustrated in figure 5.5.

Out of the beam axis the transverse components of the resulting electric fields lead to transverse heating of the extracted electron ensemble, falsifying the initial energy spreads. Due to the radial dependency of the cutting barrier, the comparison of electron energy spectra is also affected by a systematic error if the respective spectra are not taken at the same point. Both problems are obviously best circumvented by measuring the electron energy distributions in the beam center. This can be accomplished with sufficient accuracy by adjusting the position of the movable analyzer, which has a sufficiently small entrance diaphragm (diameter 25 μm, see below). Alternatively, the electron beam can be steered by additional transverse magnetic fields in a way that the analysis of the central part is ensured in all cases.

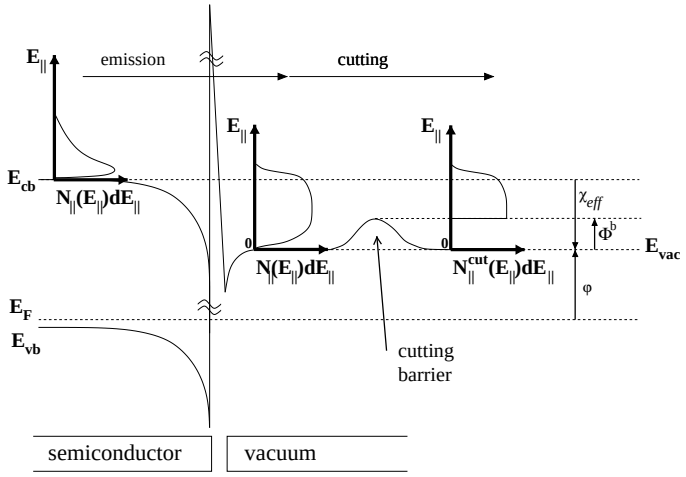

Figure 5.5: Illustration of the usage of the cutting barrier to exclude electrons with longitudinal energies below the value of $e \cdot \Phi^b$ from the extracted electron ensemble.

Retarding field analyzer

A sketch of the retarding field analyzer is shown in figure 5.6. This device consists of three electrodes made from stainless steel: An entrance electrode, a retarding electrode and a collector. The aperture of the retarding electrode has a diameter of 1 mm. The first electrode is covered by a tantalum foil with a circular hole which has a diameter of 25 microns: The largest part of the electron beam flows to ground potential over this entrance diaphragm and an amperemeter ($\approx$ total current I_{tot}). Only a small fraction, the collector current I_c, is used for the actual energy analysis in order to prevent space-charge effects which would limit the accuracy of the analyzer. The device is mounted on a flange connected to the set-up via a bellow (see figure 5.1). A motorized x-y translational stage allows, due to the small width of the entrance diaphragm, measurements at positions corresponding to the photoelectrons emitted at different points of the cathode. In particular, it permits x-y profile scans of the beam and thus the determination of the beam center with an accuracy of ± 30 μm. This accuracy is sufficient to exclude possible systematical measurement errors resulting from the influence of the contact potential induced transverse fields in the acceleration region discussed on page 44.

Figure 5.7 illustrates the calculated ideal retarding potential of the analyzer for both grounded entrance diaphragm and collector and for a retarding potential of U_{ret}=20 V applied to the retarding electrode (SIMION simulations [63]). Since the parabola-like *effective* retarding potential (shown in figure 5.7 (b)) depends on the x-y position of the electron beam at the z-position of the retarding electrode, the *measured* longitudinal energies as well as the energy spread of the electron beam (the latter due to its finite

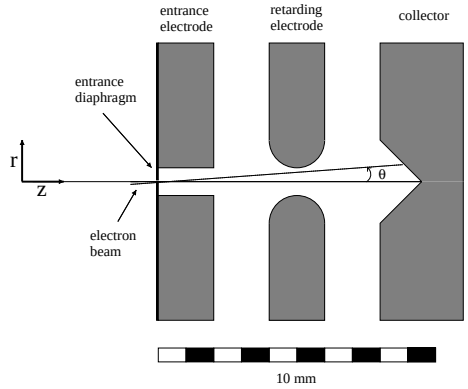

Figure 5.6: Sketch of the retarding field analyzer. The angle θ between the magnetic guiding field (and thus the electron path) and the z-axis obviously influences the radial beam position at the aperture of the retarding electrode.

dimensions) depend on its angle θ inside the analyzer (measured as the angle between the z-axis and the mean electron momentum, see figure 5.6).

Imperfections of the multi-coil arrangement could lead to small variations $\delta\theta_c$ of this angle for different settings of the magnetic guiding field. It is also clear that the limited accuracy of the manufacturing process of the analyzer leads to a deviation of the x-y position of the entrance diaphragm from the center. In addition, the mounting system of the analyzer (sketched in figure 5.1) could lead to asymmetries in the y-direction. This, in turn, could lead to a high sensitivity in respect to $\delta\theta$, since in this case the electron beam would not pass in the parabolic minimum of the retarding potential.

A reasonable estimation for the accuracy of manufacturing is 0.1 mm. At this value of r the tangential on the parabola has already a slope of about 15 meV/100 μm. Since the aperture of the retarding electrode is placed 5 mm behind the entrance diaphragm, an angular change of $\delta\theta$=1° leads to a change in r of about 90 μm (for small θ). This, in turn, results in a shift of the effective retarding potential of about 14 meV.

The shifts in longitudinal energy caused by adiabatic transverse expansion (or compression) which are used as a signature of the initial transverse electron energy are of the same order. For an accurate measurement of initial transverse energies of the order of 10 meV it is thus vital to take imperfections of the retarding field analyzer and the magnetic guiding field into account. The measures taken to investigate and minimize this systematic source of errors are described in section 5.3.2.

The resolution function of the analyzer could be determined to be in good approximation Gaussian with $\sigma_{\parallel} \approx$17 meV (see section 5.5).

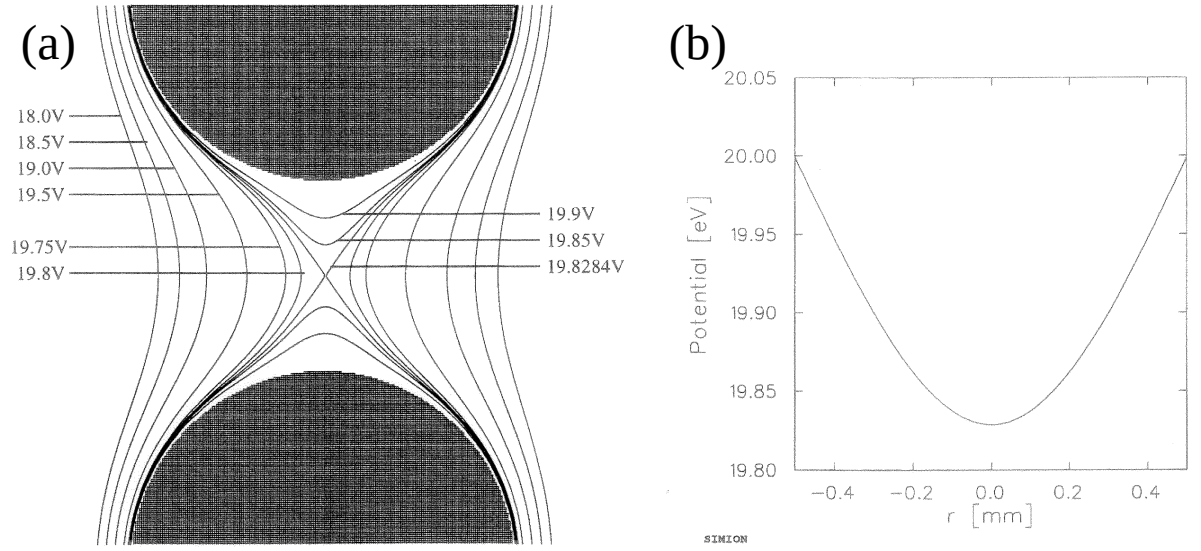

Figure 5.7: Sketch [63] of the saddle-like potential at the retarding electrode of the analyzer. Entrance diaphragm and collector are both grounded, the retarding electrode is set on a potential of 20V (SIMION simulations): (a) Equipotentials in the x-z plane, (b) maximum potential as a function of r (effective retarding potential).

5.2 Measurements of the longitudinal energy distribution

The principle of the measurement of longitudinal EDCs has already been introduced in chapter 3.2. Figure 5.8 shows a block diagram of the electronic set-up which is used to measure the longitudinal energy distribution. The integral retarding curve

$$I(U_{ret}) = I_c \cdot \int_{e \cdot U_{ret}}^{\infty} dE_{\parallel}^{m} \cdot \int_{0}^{+\infty} dE_{\perp} \cdot N^{m}(E_{\parallel}^{m}, E_{\perp}) \tag{5.1}$$

could be obtained by scanning the voltage applied to the retarding electrode and recording the electron current still being able to overcome the barrier. I_c denotes the total collector current ($U_{ret} = 0$). The measured energy distribution is denoted as N^m since the real, initial longitudinal energy can only be accessed after an additional calibration procedure (see section 5.2.1).

By modulating the retarding voltage (with an amplitude small compared to the applied retarding voltage and the resolution of the analyzer) and analyzing the collector current with a lock-in amplifier (i.e. frequency- and phase-sensitive detection), the differentiated retarding curve, i.e. the longitudinal energy distribution curve, is yielded in-situ:

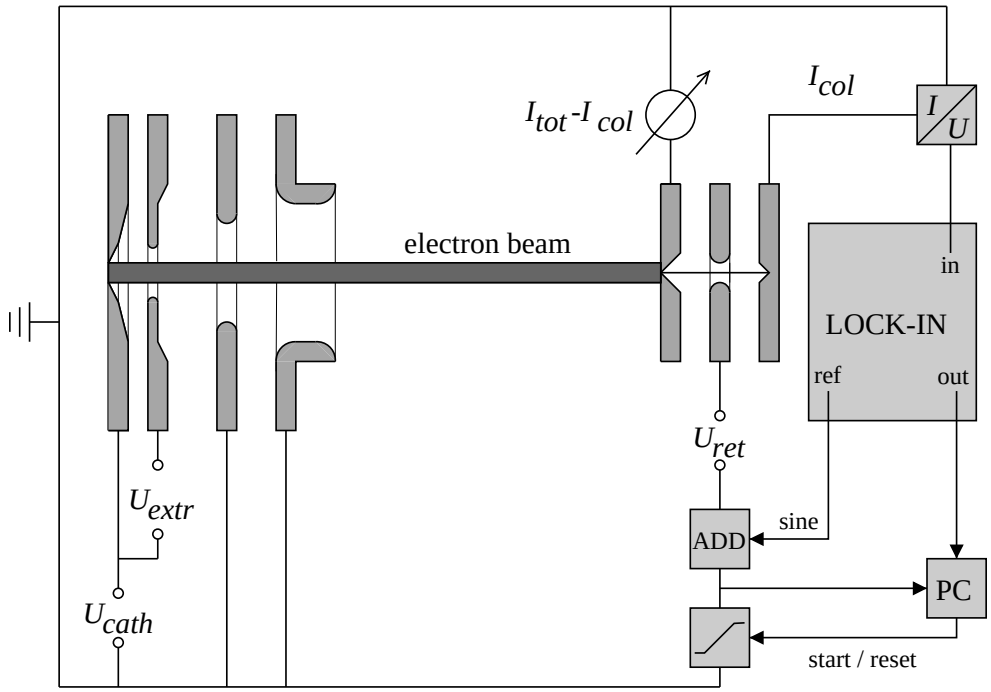

Figure 5.8: Sketch of the electronic arrangement used for the measurement of longitudinal electron distribution curves.

$$\frac{dI}{dU_{ret}}(U_{ret}) = -I_c \cdot \int dE_\perp \cdot N^m(e \cdot U_{ret}, E_\perp) = -I_c \cdot N^m_\parallel(e \cdot U_{ret}). \tag{5.2}$$

This procedure is particularly advantageous since the lock-in detection effectively suppresses contributions outside a rather narrow interval around the reference frequency (e.g. noise), leading to higher accuracies compared to a numerical ex-situ differentiation. In this experimental arrangement there is also an inductive signal resulting from the modulation of the retarding voltage and the finite capacity of the analyzer system. This signal is, however, phase shifted by approximately $\pi/2$ in respect to the modulated photoelectron current and thus easily removed by phase-sensitive analysis.

Figure 5.9 shows two longitudinal EDCs as a function of bias voltage $U_{bias} = U_a - U_{ret}$. The bias voltage of about -2.7 V is caused by the different work functions of cathode and analyzer, and by the difference of the effective retarding potential from the applied U_{ret}. The EDCs were recorded under identical experimental conditions, just that for the measurement of curve (b) the cutting barrier was risen. The resulting shift in low-energy cut-off is easily identified, whereas the high energy tail stays, in first approximation, equal. A closer look furthermore reveals a slight inflation of the EDC measured with increased cutting at bias voltages (and thus longitudinal energies) exceeding the low-energy cut-off.

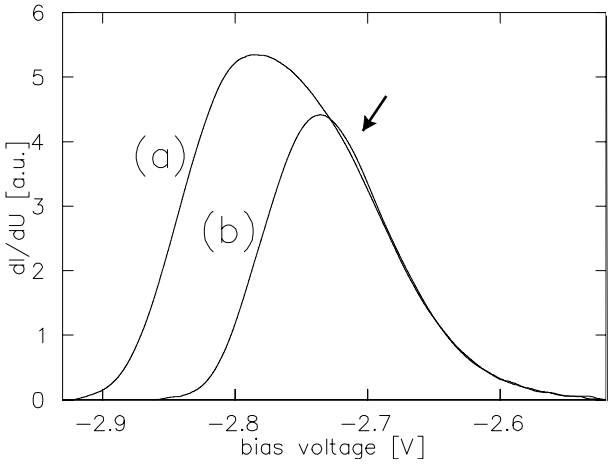

Figure 5.9: Longitudinal EDCs demonstrating the effect of the cutting barrier: It is clearly seen that the low-energy cut-off of curve (b) is shifted to higher energies in respect to the cut-off of curve (a) by an increased cutting barrier height. All other experimental conditions were kept the same. The high energy slope is in good approximation equal for the two curves, except for the slight inflation of (b) emphasized by the arrow. The collector current amounted to approximately 10 pA in the case of full extraction.

This effect was reproducibly observed; its origin, however, remained unclear. It might be resulting from the blocked electrons which are trapped in between the cathode and the cutting barrier (see figure 5.5). Some of them may undergo scattering events, gaining enough energy to overcome the barrier. Clearly, further investigations are necessary to clarify this point.

5.2.1 Calibration of the longitudinal energy scale

The one to one correspondence of a change of applied retarding potential and the resulting change of the effective potential was proved to be fulfilled very well (deviation $\ll$1 meV) in the range of used applied potential (about -20 V). This was checked by measuring the change in the retarding potential corresponding to the first moment of the EDCs which is induced by a change in acceleration voltage (and thus longitudinal beam energy). The calibration procedure thus reduces to the determination of the right offset, i.e. to a 'pinning' of the scale of retarding voltage U_{ret} (or bias voltage U_{bias}) to the absolute scale of the longitudinal energy. Since the work function of the analyzer system potentially changes with time, this calibration procedure has to be performed for every set of measurements. In particular, the knowledge of the bias voltage U_{bias}^{vac} corresponding to the vacuum level enables one to reconstruct the initial distribution of electrons over the longitudinal emission energies. The position of the vacuum level is conventionally determined

by the position of the maximum of the derivative of the longitudinal EDC [2, 4]. The according bias voltage could be determined with an accuracy better than ±10 meV.

The method of the determination of the position of the conduction band minimum used in this thesis was first reported by [4] and was already introduced in chapter 2.2. The first step is a matching of the photon energy and the $\vec{k}$-dependent magnitude of the band gap. The used laser had a wavelength of 685 nm, resulting in $h\nu$=1.81 eV. The band gap of GaAs at 90 K was taken as 1.51 eV. The conduction band minimum is well isotropic in the vicinity of the band gap, the nonparabolicity was accounted for according to reference [64]. The heavy-hole band is parabolic in the vicinity of the band gap. It is, however, necessary to take into account its anisotropy. Since the resolution of the analyzer did not permit to resolve contributions from different $\vec{k}$, the average effective mass of m_{hh}=0.55 m_e [19] was used.

In order to account for the deviation due to the heavy doping of the material (band tailing), the effective minimum of the conduction band was taken to be 10 meV below the value stated above. This shift is in good agreement with the values obtained at the Institute of Semiconductor Physics in Novosibirsk on samples with the same material parameters [65]. The resulting energy of the excited electrons above the conduction band minimum amounts to (255±5) meV. The mean transverse energy of photoelectrons with longitudinal energy of the corresponding minimum of the derivative of the EDC amounts to about 15 meV (see chapter 6.3.1). The position of the conduction band minimum thus is (240±5) meV below the longitudinal energy corresponding to the minimum. Together with the accuracy of determination of the position of the peculiarity corresponding to the heavy-hole band - conduction band transitions, the accuracy of determination of the position of the conduction band minimum amounted to typically ±10 meV.

To exemplify this procedure, figure 5.10 shows a typical example: Reflection mode illumination with a red laser (λ =685 nm) leads to the emission of non-relaxed and non-thermalized electrons. Curve (1) in figure 5.10(a) shows a longitudinal EDC recorded under full extraction (extraction electrode grounded). The corresponding high energy tail measured under infrared illumination under the same conditions is plotted as the dashed curve (2) for comparison. The relevant high energy tail of (1) has a relatively low signal to noise ratio. A strong increase of illumination would lead to very high total currents and thus to a degradation of the cathode and to broadenings of the spectrum resulting from beam relaxation effects. In order to improve the signal to noise ratio in the high energy tail without these harmful consequences, the laser power is increased only after reducing the total current by adjusting the cutting potential accordingly, yielding curve (3). In the derivative (4,5) of the latter longitudinal EDC (figure 5.10 (b)) the signatures

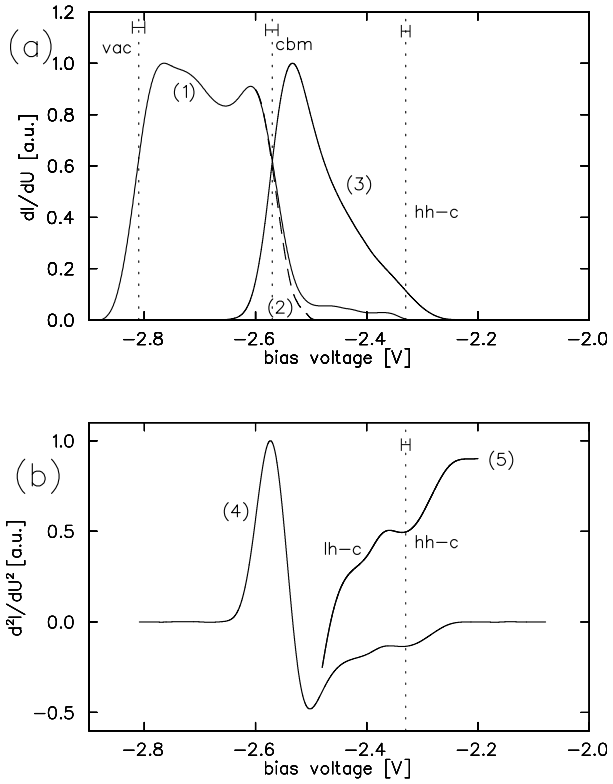

Figure 5.10: Example for the applied calibration procedure for the longitudinal energy scale. (a) The longitudinal EDC (1) was recorded at a sample temperature of 90 K under red laser illumination (λ = 685 nm) for full extraction. To show the modification in the high energy tail of the EDC due to short wavelength illumination the corresponding EDC for infrared illumination is included (dashed curve (2)). Curve (3) was recorded with applied cutting barrier and increased light intensity. (b) Derivative (4) of the latter curve. The relevant range is rescaled (5) for better visibility. The features corresponding to transitions form the heavy-hole band and light hole band to the conduction band are indicated as hh-c and lh-c, respectively. $|\chi_{eff}|$ amounts to approximately 240 meV. (The matching of the position of the conduction band minimum and the maximum in the derivative is coincidental.)

of the different transitions induced by the monochromatic light illumination are indicated. While the signature of the transition from the heavy-hole band to the conduction band (hh-c) is clearly resolved as a minimum in the derivative of the EDC, the signature of the transition from the light-hole band to the conduction band (lh-c) can be attributed to the additional shoulder approximately 80 meV below. The determined positions of the conduction band minimum and the vacuum level are also indicated in the figure.

The value of $|\chi_{eff}|$ is determined as the distance of the conduction band minimum from the vacuum level and thus has an inaccuracy of $\approx \pm 14$ meV.

5.3 High accuracy measurements of the mean transverse energy

As shown in chapter 3.1.2, an adiabatic passage of an electron beam through a region with varying magnetic field strength leads to a well defined transfer of energy between the longitudinal and transverse degrees of freedom of the electron beam. The resulting shifts in mean longitudinal energies can, in principle, be accessed easily by the measurement of longitudinal energy distributions discussed in the preceding section. The set-up also allows one to cut off a defined low energy part of the photoelectron longitudinal energy distribution with the potential barrier in front of the cathode, so that certain subensembles of the photoemitted electrons can be analyzed. Mean transverse energies of electron beams photoemitted from NEA-GaAs at cryogenic temperatures are expected to be as low as a few meV. This section describes the measures taken to reach both the accuracy and the resolution necessary to investigate initial transverse energies of this order in the set-up described above.

The necessarily serial nature of a text as the present one requires an artificial separation of this section into two parts. For the explanation of the improvements of resolution in section 5.3.1, it is assumed that the systematic errors which are addressed in section 5.3.2 are already suppressed. The latter section deals with the problem to accurately identify and suppress artificial shifts of longitudinal energies in the measurements performed with a retarding field analyzer in a variable magnetic guiding field.

5.3.1 Increasing the resolution of the given set-up

The system was originally designed to provide an expansion factor α (see equation 3.12 on page 23) between 0.5 and 1 with a total magnetic field of up to B_0=1300 G. Only adiabatic transverse *expansion* was thus applied by Pastuszka et al. for the measurements.

According to formula 3.21, the experimentally accessible signature of the initial MTE, i.e. the shift of MLE, is proportional to $\delta\alpha$. The maximum *absolute* value of (1-α), which thus determines the resolution of the technique[3], can be increased by employing the opposite of adiabatic transverse expansion, i.e. adiabatic transverse *compression*. In fact, in case of expansion, α is always smaller than unity but larger than zero, leading to a maximum of $|1-\alpha|$ smaller than unity. In the case of compression, α is larger than unity but has no restricted maximum as a matter of principle.

Practical limits for a stronger expansion are, on the low field side, set by the necessity to supply a sufficient longitudinal magnetic field strength to avoid a strong onset of transverse-longitudinal relaxation and to dominate over stray-fields. It showed to be disadvantageous to lower the strength of the magnetic guiding field below approximately 400 G at the used current densities of below 5 μA/cm^2. The maximum longitudinal field strength which could be applied with the requirement of homogeneous field at both the cathode and analyzer region is limited by the maximum current allowed by the water cooling system of the correction coils; it amounts to about 1300 G for both the cathode- and the analyzer-positions. It proved possible to provide an adiabatic passage of the electron beam with an initial magnetic field of 500 G and a varied field strength at the analyzer region between 500 G and 1250 G. This leads to a range of α of 1 to 2.5. Figure 5.11 illustrates the longitudinal field strength as a function of the z position, parameterized by the value of the corresponding alpha. While (a) shows the conventional case used by Pastuszka et al., (b) displays the new settings for the magnetic field.

The adiabacity parameter of the passage is increased only by a factor of 1.5, amounting to

$$\xi < 3 \cdot \frac{10^{-5}}{\sqrt{eV}} \cdot \sqrt{E_{\parallel}} \tag{5.3}$$

and thus for the employed $E_{\parallel}$=20 eV to

$$\xi < 1.4 \cdot 10^{-4} \tag{5.4}$$

which is still small compared to unity, such that the adiabacity of the passage is ensured. Since the used magnetic field configuration is corresponding to a magnetic mirror, it should be stated here that electrons will not be reflected in the region of rising field strength. The loss of longitudinal energy an electron suffers is maximum for an adiabatic passage and amounts to $(\alpha-1)\cdot E_{\perp}$. It is thus of the order of the initial transverse energy. $E_{\perp}$ is, except for the Maxwellian tail of the distribution of transverse energies at high $E_{\perp}$, smaller than a few hundred meV, since the emission energy for most electrons is about

[3] A measurement at $\alpha = 1$ should be possible in order to determine the longitudinal EDC.

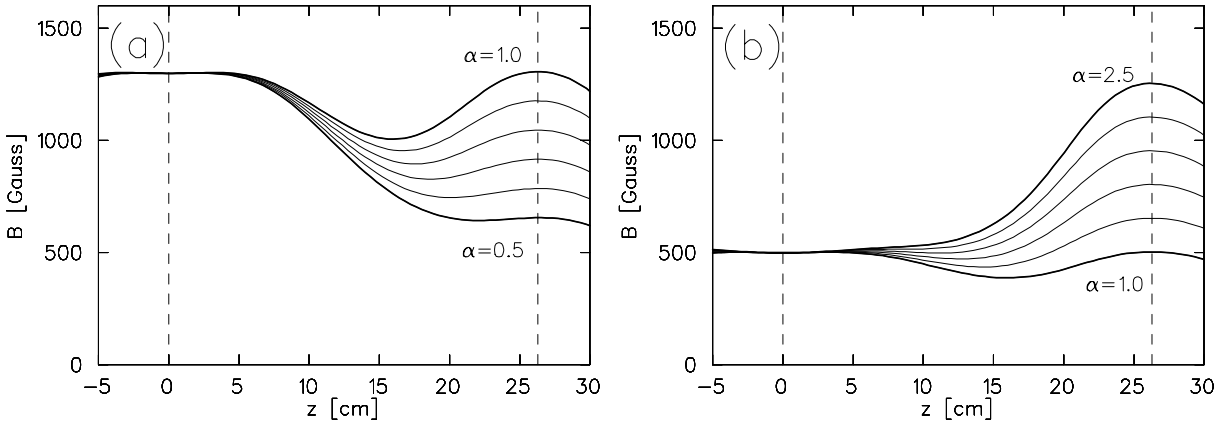

Figure 5.11: Plots of the longitudinal magnetic field strength as a function of α for (a) expansion with B_i=1300 G (conventional) and (b) compression with B_i=500 G (new). The coordinates of the cathode (z_c=0) and of the analyzer (z_a=26.2 cm) are indicated by dashed lines.

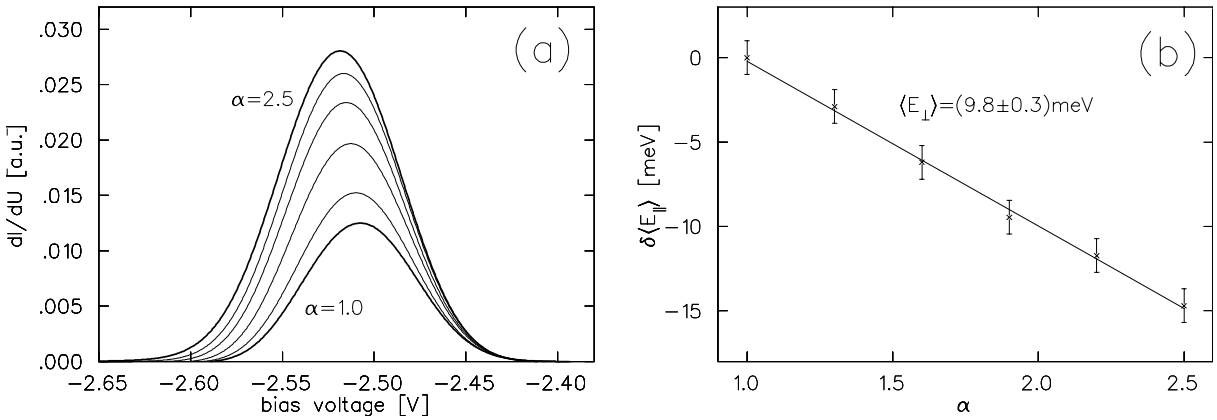

Figure 5.12: Example for a high accuracy MTE measurement using the new compression method. The longitudinal energy distribution curves are plotted in (a), while (b) shows the shift in mean longitudinal energy as a function of α. The error bars may seem overestimated: They denote the combined reading accuracy of the millivolt-meters used for the determination of U_a and U_{ret}, respectively. The fit yields a mean transverse energy of (9.8±0.3)meV.

the value of $|\chi_{eff}|$. The distribution at high $E_\perp$ is characterized by a slope about the sample temperature, i.e. much smaller than 100 meV. The longitudinal energy is, due to the acceleration, of the order of 20 eV and thus two orders of magnitude higher than the transverse energy of practically all electrons.

To illustrate the strong improvement of the resolution achieved by the usage of adiabatic transverse compression instead of the conventional case of expansion, figure 5.12 shows a

measurement of MTE performed with an initial magnetic field of 500 G and a maximum compression to α=2.5. The cathode was cooled to 90 K and the potential barrier height was adjusted to be approximately corresponding to the conduction band minimum. The slope of the linear fit to the mean longitudinal energy as a function of α amounts to (9.8±0.3) meV. The shift itself is about 14.7 meV, a factor of three larger than the shift which would have to be observed in the case of expansion from α=1 to 0.5.

Figure 5.12 (a) also illustrated that compression leads to an increase of the collector current. Thus it is, notwithstanding the particular magnetic field configuration, advantageous to use compression instead of expansion in all cases with a limited initial current density. This is particularly the case for photoemission from NEA-GaAs, since the lifetime of these emitters depends on the drawn current. Furthermore, the electron yield at longitudinal energies exceeding the conduction band minimum drops dramatically, such that the investigation of the respective subensembles of the photoelectron beam requires an increase of illumination power for the measurements. The resulting potentially harmful consequences can thus be minimized by using adiabatic transverse compression instead of expansion.

The strong dependence of the transverse energy of the photoelectrons on their longitudinal energies can be seen from the MTE-measurement shown in figure 5.13. It was performed at low temperatures under current limited emission. The MTE of the electron beam was determined to be (49.1±3) meV. The transformation of the longitudinal energy distribution upon expansion to α=2.5 reveals a low shift in the high longitudinal energy region, and a strong shift for the low longitudinal energies. Since no reliable, quantitative model for the photoemission from NEA-GaAs has been reported, it is practically impossible to reconstruct the total distribution of electron energies from the measurements of MTE in an unequivocal manner.

5.3.2 Measuring small energy shifts with a retarding field analyzer in varying magnetic guiding fields

In order to reach the accuracy and reproducibility necessary to measure shifts of a few meV in longitudinal energy, it is vital to take the practical imperfections of the retarding field analyzer into account, in particular the dependence of the effective retarding potential on the entrance angle of the electron beam, a possible deviation of the radial position of the entrance diaphragm from the center of the aperture of the retarding electrode and a possible disturbance of the symmetry due to the analyzer mounting system

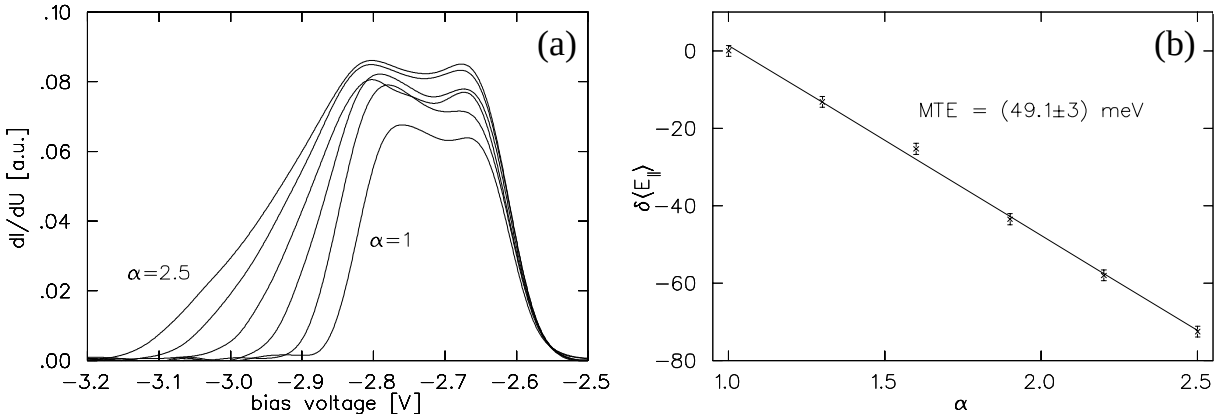

Figure 5.13: MTE measurement with full extraction and adiabatic transverse compression up to α=2.5. (a) EDCs measured with compression and (b) shift of mean longitudinal energy upon compression as a function of α.

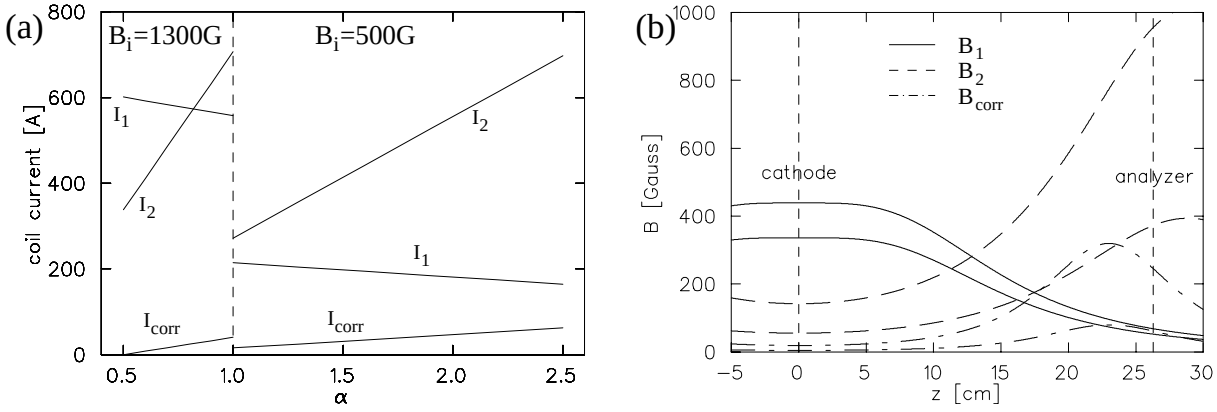

Figure 5.14: (a) Settings for the driving currents of the three pairs of coils at two different initial B-fields and different expansion parameters α and (b) the contributions of the separate pairs of coils at B_i=500G at α=1 and α=2.5 as a function of z. The subscript '1' ('2') denotes the inner (outer) pair of coils, 'corr' the correction coils.

as discussed on pages 46f. The x-y position of the beam center at the z-position of the entrance diaphragm does indeed move if α is changed, indicating a change of the beam angle in the drift region. (The retarding curve has, however, always to be measured in the beam center, such that systematic errors due to varying cut-offs resulting from the blocking barrier in front of the cathode can be neglected.)

The magnetic guiding field strength has to exceed a certain minimum value of approximately 400 G at the used current densities and beam energies to avoid relaxation effects and disturbances due to stray fields. As long as these conditions were met, measured shifts in longitudinal energy (measured in the respective beam center) for different B_0 are

far below 1 meV. Thus, for varied total magnetic field with constant expansion factor, eventual variations of the entrance angle have negligible effect. The change of the beam center position at the entrance diaphragm amounts to about 0.1 mm if the magnetic guiding field strength B_0 is changed from 650 G to 1300 G (both α =1), indicating a mean transverse stray field of the order of 1 G.

Imperfections of the coil arrangement

The separate coil currents are set according to $I_l = I_{l0} + c_l \cdot (\alpha - 1)$ for the adjustment of different expansion parameters (the subscript denotes the specific coil, see figure 5.14 a). The change of the magnetic field invoked by a single coil upon an expansion to α is thus linear in $(\alpha - 1)$. This leads to a change of the relative contribution of the single coils to the total magnetic field $\vec{B}_t$ (see figure 5.14 b). This, in turn, could lead to a change of the angle θ between $\vec{B}_t$ and the z-axis at a given z-position, in particular at the analyzer.

Imperfections of the multi-coil arrangement (in particular slight tilting of the individual coils) thus lead to a change of the electron beam's entrance angle to the analyzer. This causes an artificial shift $\delta E_{\parallel c}$ in longitudinal energy which masks the signature of the initial transverse energy.

The following discussion is based on the assumption of small angles between $\vec{B}_t$ and the z-axis ($\theta \ll 1$). In addition, a single transverse component of $\vec{B}$ is discussed for simplicity. The total longitudinal field component as a sum of the contributions of the single coils (denoted by l), is not affected:

$$B_{t\parallel}(z) = \sum_l B_{l\parallel}(z) \approx \sum_l |\vec{B}_l(z)|. \tag{5.5}$$

A change of the transverse component

$$B_{t\perp}(z) = \sum_l B_{l\perp}(z) \text{ with } B_{l\perp}(z) \propto |\vec{B}_l(z)| \tag{5.6}$$

has, in contrast, to be taken into account. The change of the transverse component of the magnetic field invoked by the separate coils is proportional to the change of driving current, i.e. it is linear in $(\alpha - 1)$:

$$\delta B_{l\perp}(z) = a_l(z) \cdot \delta I_l = a_l(z) \cdot (\alpha - 1). \tag{5.7}$$

This proportionality also holds for the total transverse field, since the latter is a linear superposition of the contributions of the single coils. Since the angle of the electron beam relative to the z-axis, θ, is (in the small angle approximation) given by

$$\theta(z) = \frac{B_{t\perp}(z)}{B_{t\parallel}(z)}, \tag{5.8}$$

the change of angle $\delta\theta_c$ due to the coils with a change of the expansion parameter from 1 to α consequently amounts, at the analyzer position z_a (i.e. $B_{\parallel\alpha}(z_a) = B_{\parallel\alpha=1}(z_a)/\alpha$), to

$$\begin{aligned}
\delta\theta_c(z_a) &= \frac{B_{\perp\alpha}(z_a)}{B_{\parallel\alpha}(z_a)} - \frac{B_{\perp\alpha=1}(z_a)}{B_{\parallel\alpha=1}(z_a)} && (5.9)\\
&= \frac{B_{\perp\alpha}(z_a)}{\alpha \cdot B_{\parallel\alpha=1}(z_a)} - \frac{B_{\perp\alpha=1}(z_a)}{B_{\parallel\alpha=1}(z_a)} && (5.10)\\
&= \frac{1}{\alpha \cdot B_{\parallel\alpha=1}(z_a)}(B_{\perp\alpha}(z_a) - \alpha \cdot B_{\perp\alpha=1}(z_a)) && (5.11)\\
&= \frac{1}{\alpha \cdot B_{\parallel\alpha=1}(z_a)}\left(\sum_l a_l(z_a)[I_{l0} + c_l(\alpha-1)] - \alpha \cdot \sum_l a_l(z_a) I_{l0}\right) && (5.12)\\
&= \frac{\alpha-1}{\alpha} \cdot \frac{\sum_l (c_l a_l(z_a) - a_l(z_a) I_{l0})}{B_{\parallel\alpha=1}(z_a)} && (5.13)\\
&= \xi_c \cdot (1 - \frac{1}{\alpha}), && (5.14)
\end{aligned}$$

i.e. it is proportional to $(1 - \frac{1}{\alpha})$, ξ_c denoting the proportionality constant.

Effect of steerer coils

A first correction was already performed by Pastuszka et al. [12, 13] by means of steerer coils extending from beyond -z_a up to beyond z_a supplying correction fields in the x- and y-direction. They were applied to steer the beam center to a fixed position of the entrance diaphragm for all expansion factors applied. This procedure is, however, not sufficient for measuring energy shifts in the low meV-range with increased resolution: The z-dependent changes in the transverse B-field invoked by linearly independent variations of the different coil currents are compensated as a *mean* (at least up to the entrance diaphragm), it is, however, not a priori clear that the transverse fields and thus the angle of the electron beam *inside* the analyzer equals the average over the whole drift region.

Hence, the adjustment of the beam position at the entrance diaphragm of the analyzer and of the beam angle while passing the retarding potential were separated. For this

purpose, the present steerer coils were shortened in order not to overlap the analyzer region (position steerers), while additional steerers were applied in that region in order to allow an adjustment of the angle in the analyzer (analyzer steerers). This arrangement is illustrated in figure 5.1 on page 42.

It was found that the measured EDCs remained unshifted with an accuracy of $\ll 1$ meV when only the driving currents of the position steerers were changed (at least in the range relevant for the experiments, i.e. resulting in shifts below about 1 mm apart from the initial beam axis). This is easy to understand since the shift in beam position at the analyzer is the result of the integrated effect of these steerers over the whole drift region. The position steerers are thus mainly used to simplify the experimental procedure by keeping the position of the beam center at $z = z_a$ constant for all α.

The analyzer steerers, if alone varied, also have a slight influence on the beam center position at the entrance diaphragm. This had to be accepted in order to allow for a reasonable effectiveness of these steerers. It can easily be compensated by the position steerers since this shift is low and linear with the analyzer steerer currents.

In order to investigate the possible influence of the practical nature of both coils and retarding field analyzer, measurements of longitudinal EDCs were performed with different currents applied to the analyzer steerers. They were analyzed regarding the resulting shift $\delta E_{\parallel s}$ in measured mean longitudinal energy. In order to avoid shifts in mean longitudinal energy caused by an upshift of the vacuum-level due to degradation of the cathode, a scan of the electron beam profile prior to each measurement was avoided. Instead, a high cutting barrier was applied, resulting in a quite Gaussian beam profile, and the position of the entrance diaphragm was adjusted to the beam center only approximately by adjusting the position steerers to the point of maximum collector current. The resulting error in the determination of the shift of mean longitudinal energy due to different low-energy cut-offs caused by the cutting potential were estimated to be ± 2 meV. Only very small changes (< 1 meV) were observed in the x-direction. Results for the y-direction are shown in figure 5.15.

Notwithstanding the large inaccuracies, the results show that $\delta E_{\parallel s}$ is approximately linear with the applied current and anti-linear with the strength of the longitudinal field in the analyzer region. Changes of the width and shape of the longitudinal distributions were found to be negligible.

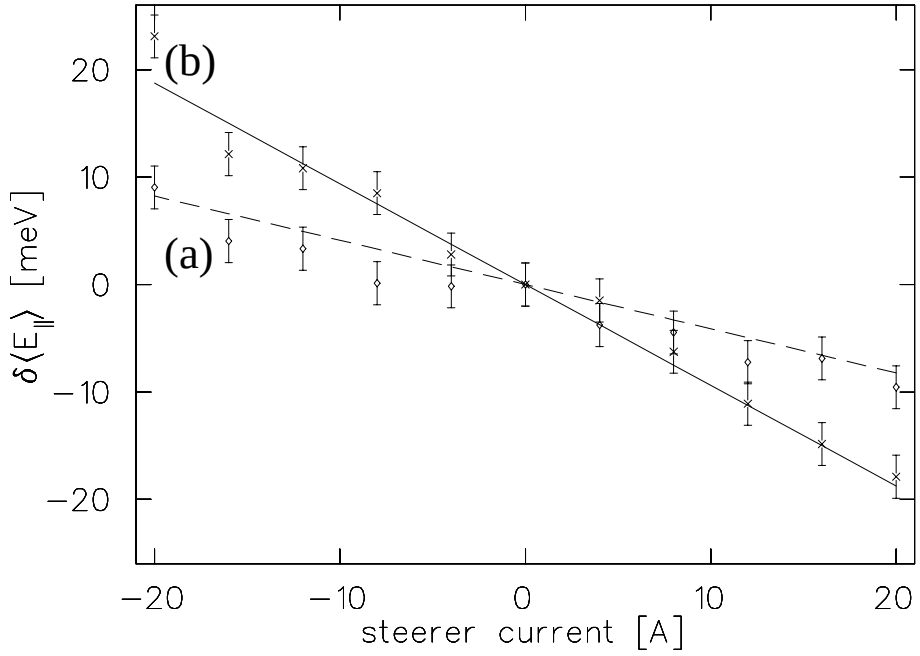

Figure 5.15: Change of mean longitudinal energies of EDCs ($\alpha = 1$) resulting from a change of the electron beam angle inside the analyzer, invoked by different currents applied to the analyzer steerers. The longitudinal magnetic field strength amounted to a) 1300 G and b) 670 G. The slopes of the fitted lines result in (35 ± 2) meV/40 A and (16 ± 2) meV/40 A, respectively.

The additional change of angle $\delta\theta_s$ invoked by the analyzer steerer is, in the approximation of small angles θ, given by

$$\delta\theta_s \approx \frac{B_{s\perp}}{B_{t\parallel}} = \xi_s \cdot \frac{I_s}{B_{t\parallel,}}, \text{ since } B_{s\perp} \ll B_{t\parallel}, \tag{5.15}$$

i.e. it is proportional to the steerer current. We can thus assume a passing of the beam on an approximately linear potential ramp in the y-direction. The sign of the steerer current is defined as the direction of its action, such that a positive y-steerer current leads to a shift of the electron beam in positive y-direction. Figure 5.15 indicates that such a positive shift leads to a decrease in measured longitudinal energies, i.e. the *effective* retarding potential for a given voltage applied to the retarding electrode is higher.

The linearity of the shift indicates that the electron beam does not pass in the minimum of the retarding potential in y-direction. This could be caused by an entrance diaphragm of the analyzer which is not properly centered. In this model, the electron beam passes the parabola-like retarding potential at (or close to) the minimum only in x-direction. The steerer field can be estimated to be approximately 10 G for 20 A, resulting in a change of angle of $\arctan(\frac{B_{s\perp}}{B_{t\parallel}}) \approx 0.45°$ for $B_{t\parallel}$=1300 G. An offset of the order of 100

microns in y-direction, a misalignment quite in the range of the manufacturing accuracy of the device, could explain the experimental findings of $\delta\langle E_\parallel\rangle \approx (16 \pm 2)$ meV/40 A at $B_{t\parallel}$=1300 G (see figure 5.7). Alternatively, the mounting of the analyzer electrodes could disturb the symmetry in y-direction, potentially contributing to the observed deviation from the ideal case.

Singling out the contribution of the transverse electron energy

The *measured* shift of longitudinal energy with an expansion α, $\delta E_\parallel^m(\alpha)$, thus separates into three additive terms:

$$\delta E_\parallel^m(\alpha) = \delta E_{\parallel,E_\perp}(\alpha) + \delta E_{\parallel c}(\alpha) + \delta E_{\parallel s}(\alpha), \tag{5.16}$$

where

- $\delta E_{\parallel,E_\perp}$: The shift of the mean longitudinal energy due to the transfer of energy between the longitudinal and transverse degrees of freedom. It is linear in $(\alpha - 1)$, as can be seen from equation 3.21.

- $\delta E_{\parallel c}$: Since the electron beam passes on a linear ramp in the analyzer, the resulting shift in longitudinal energy is proportional to the change of the beam angle in the analyzer (as long as the latter is small), and thus (with equation 5.14):

$$\delta E_{\parallel c} \propto \delta\theta_c \propto \left(1 - \frac{1}{\alpha}\right). \tag{5.17}$$

  Figure 5.16 illustrates the functional dependence of the resulting shift of longitudinal energy caused by this second term of equation 5.16.

- $\delta E_{\parallel s}$: Also the change of measured longitudinal energy resulting from an applied analyzer steering current is proportional to the change of beam angle in the analyzer, and thus, with equation 5.15:

$$\delta E_{\parallel s}(\alpha) \propto \delta\theta_s \propto \frac{\delta I_s}{B_{t\parallel}(z_a)} = \frac{\delta I_s}{\alpha \cdot B_0}. \tag{5.18}$$

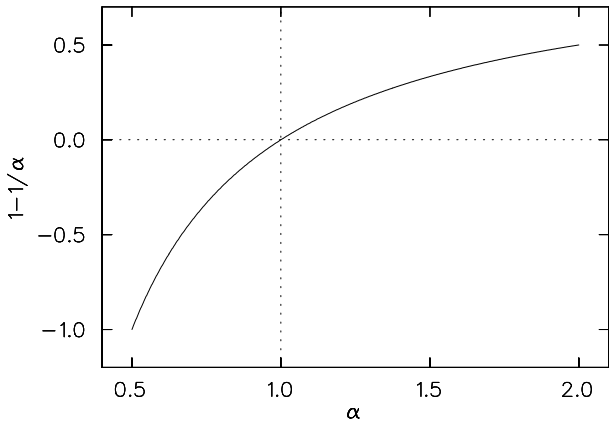

Figure 5.16: A plot of α vs. $\left(1-\frac{1}{\alpha}\right)$, the functional dependence of the artificial shift in longitudinal energy due to a changed angle of the electron beam in the analyzer, caused by imperfections in the magnetic coil arrangement (under the assumption of small angles).

In order to single out the shift caused by the transfer of energy between the longitudinal and the transverse degrees of freedom due to the adiabatic passage of the region of varying magnetic field strength, or equivalent, to find the conditions under which

$$\delta E_{\parallel c} + \delta E_{\parallel s} = 0, \tag{5.19}$$

$\delta E_{\parallel s}$ has to follow the same proportionality as $\delta E_{\parallel c}$, that is $\delta E_{\parallel s} \propto (1-\frac{1}{\alpha})$. The change of analyzer steerer currents with expansion to α thus has to be proportional to $(\alpha-1)\cdot B_0$, that is

$$I_s = I_{0s} + c_s \cdot (\alpha - 1) \cdot B_0. \tag{5.20}$$

To find the remaining proportionality factor c_s, measurements of MTE with different c_s have been performed. Figure 5.17 shows results for c_s=0 (a), c_s= -16 A/1300 G (b) and c_s=-28 A/1300 G (c). The lines correspond to fits according to $\delta\langle E_\parallel\rangle = E_\perp \cdot (\alpha-1) + b \cdot \left(1-\frac{1}{\alpha}\right)$ with $E_\perp$ and b varied.

Several aspects can be observed. Firstly, a linearity of a fitted slope of $\delta\langle E_\parallel\rangle$ is, within the given accuracy, a necessary, but not sufficient criterion for the correct determination of the initial MTE. Secondly, the deviation from a linear slope indeed follows the dependence depicted in figure 5.16, as is particularly explicit on the expansion-side of the figure ($0.5 < \alpha < 1$). The results published in [12] do indeed show a slight upward bending of the shift of mean longitudinal energy if α is lowered from 1 to 0.5. This leads to an systematic overestimation of $\langle E_\perp\rangle$ by an additive term. This additional term becomes particularly important at low overall shifts. The high results on $\langle E_\perp\rangle$ (approximately 14 meV) of electron ensembles emitted with longitudinal energies above the conduction

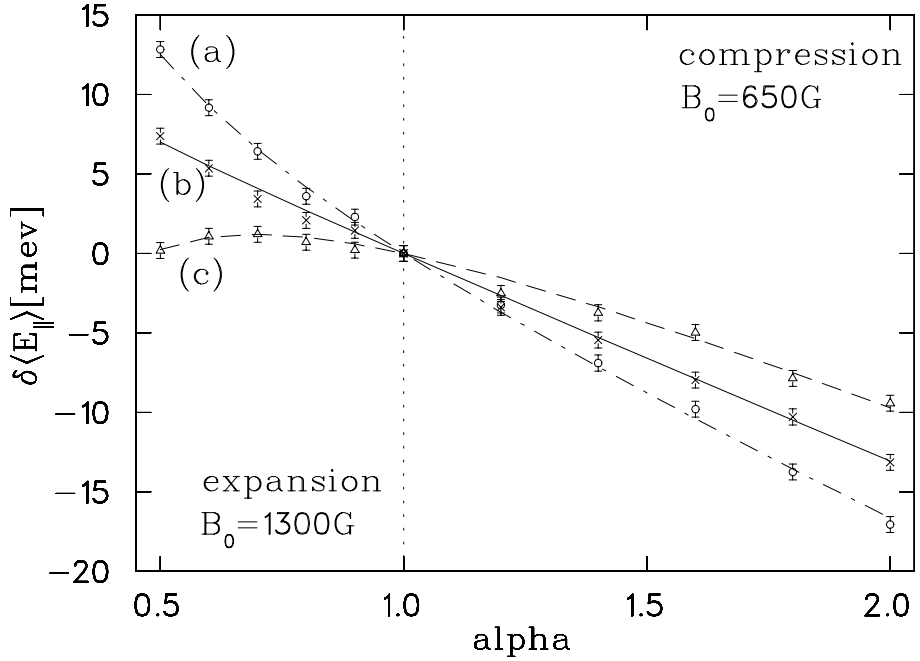

Figure 5.17: Measured shifts of $\langle E_\parallel \rangle$ upon expansions with different steerer current coefficients: c_s=0 (a), c_s= -16 A/1300 G (b) and c_s=-28 A/1300 G (c). The lines correspond to fits assuming a linear shift due to the initial mean transverse energy and an additional shift proportional to $\left(1 - \frac{1}{\alpha}\right)$.

band minimum from a cathode cooled with liquid nitrogen compared to the results obtained in this thesis (about 7.8 meV) are probably, at least to a large extent, caused by this source of systematic errors (note that a measured shift of 1 meV is converted to 2 meV of mean transverse energy in this case, see equation 3.21).

The correct MTE is obviously obtained from the measurements with that analyzer steerer currents obeying the above condition, which lead to the same linear slope over the whole range of α. It amounts to (13.5±0.5) meV in the given example. It corresponds to a slope *between* the measured one for the case of expansion and compression, respectively, as is also clear from figure 5.16, since the functional dependence of the systematic artificial shift changes its sign at $\alpha = 1$. It can be seen that the accuracy is greatly enhanced by the usage of compression instead of expansion: The discrepancy of the last point of the curve from the correct value is, for a comparison of compression to α=2 to an expansion to α=0.5, indeed proportional to $|1 - \frac{1}{\alpha}|$ and thus half as large in the case of compression. Since for the determination of the MTE the shift in mean longitudinal energy is multiplied by a factor of $\frac{-1}{\alpha - 1}$, the error is even reduced by a factor of four. For an expansion up to $\alpha = 2.5$ the respective error in $\langle E_\parallel \rangle$ is 0.6, for the determination of $\langle E_\perp \rangle$ it is, however, reduced by a factor of 5.

5.4 The transverse energy distribution of electrons with a fixed longitudinal energy

The lock-in technique is employed in the measurements of longitudinal EDCs in order to obtain the longitudinal energy distribution in-situ, with higher accuracy. It is, however, possible to exploit the advantages of lock-in techniques to a much larger extent if an electron subensemble is 'marked' *earlier* in the experiment, particularly before the *actual* measuring process, i.e. the adiabatic transverse expansion respectively compression, takes place.

Figure 5.18 illustrates the principle of the measurements described in this subsection: The potential barrier is set to the desired value of longitudinal energy $E_{\parallel}^{b} = e \cdot \Phi^{b}$ and modulated with a small-amplitude sine ($\approx$ 10 meV peak to peak). Consequently, the current I^{b} of the subensemble of the electron beam with longitudinal energies within the range the modulated barrier crosses is modulated. The retarding curve of the I^{b} is recorded by lock-in analysis of the collector current as the retarding voltage is ramped. The value of $E_{\perp i}$ corresponding to a longitudinal energy after the expansion is determined according to equation 3.24, yielding the energy distribution $N_{\perp}(E_{\parallel}^{b}, E_{\perp})$ of the marked subensemble with $E_{\parallel} = E_{\parallel}^{b}$.

Figure 5.19 shows the electronic solution used in the reported experiments: By adjusting

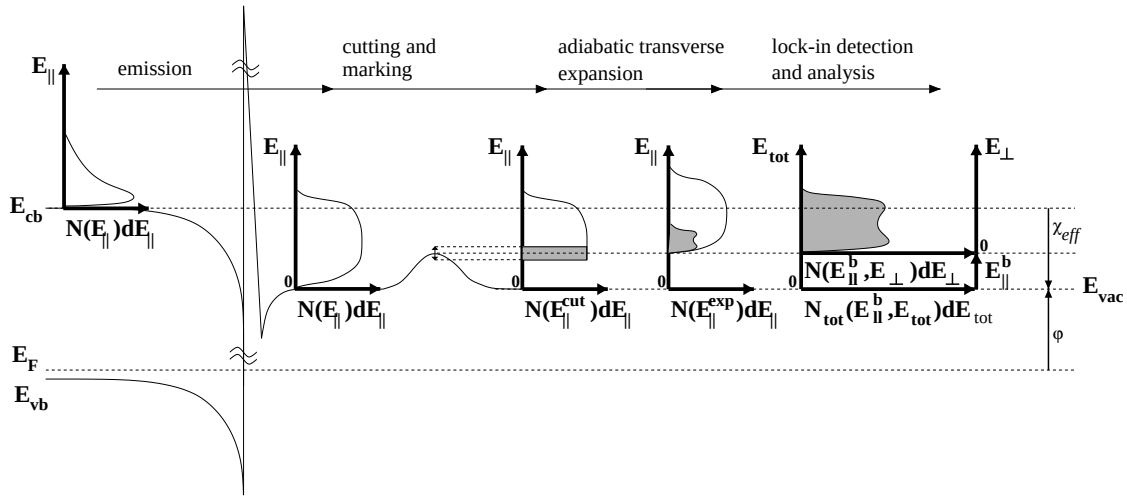

Figure 5.18: Sketch of the principle of measuring the transverse energy distribution for a subset of the electron beam, defined by its longitudinal energy. The processes are shown for the case of adiabatic transverse expansion *since the resulting up-shift in longitudinal energies is better suited to illustrate the measurement principle.*

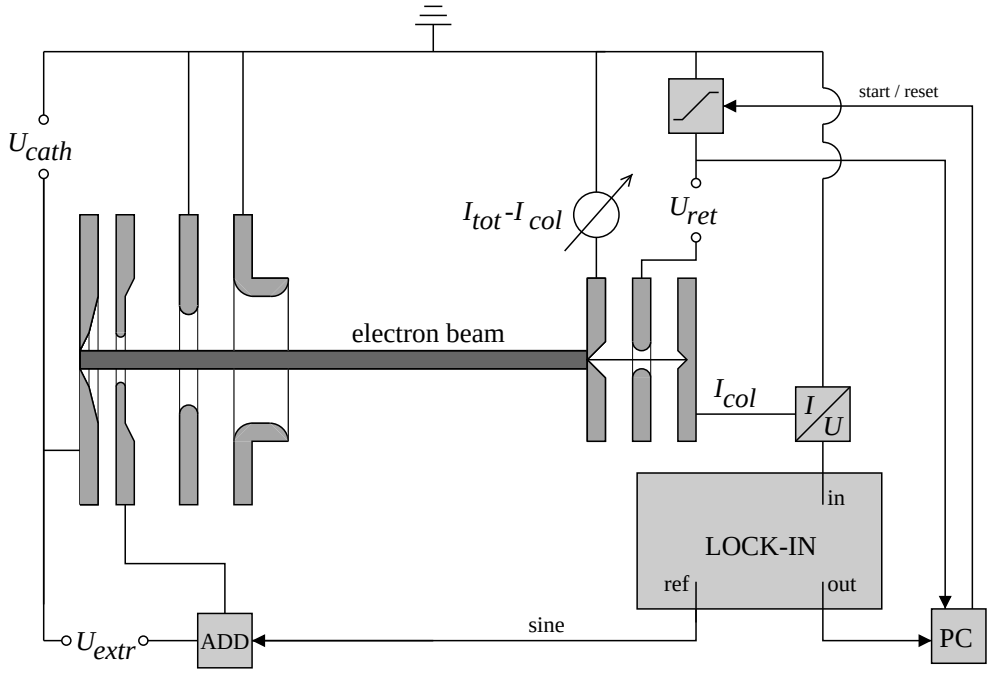

Figure 5.19: Block diagram of the electronics used for $N_\perp(E_\parallel^b, E_\perp)$-measurements.

the extraction voltage to the desired longitudinal energy and adding a modulated voltage, the respective subensemble is marked. Phase-sensitive registration of the collector current yields the retarding curve for the specific subset.

Figure 5.20 shows an example of a measurement of $N_\perp(E_\parallel^b, E_\perp)$: (a) shows the longitudinal EDC of the photoelectrons for full extraction; (b) and (c) depict the retarding curves for two different longitudinal marking energies $E_\parallel^b$ at $\alpha = 1$ (thin lines) and $\alpha = 2.5$ (thick lines). The retarding curves were normalized to the same maximum: For better visibility the increase of collector current upon compression was not taken into account in the presentation. According to the discussion of the ideal case leading to equation 3.22, the distribution of longitudinal energies of the modulated current should be a δ-function. The corresponding retarding curve, i.e. the integral, should thus yield a step function. A broadening of the thin curves is, however, easily identified. It is caused by the limited resolution of the retarding field analyzer ($\sigma_\parallel \approx 17$ meV) and the finite amplitude of the barrier height modulation ($\approx$5 meV). The retarding curves of I^b after compression is shifted to lower energies, and the step is further broadened, particularly in case (c). The corresponding derivatives are shown in figure 5.20 (d) and (e): While the thin lines represent the respective $N_\parallel(E_\parallel^b)$, the thick lines correspond to $N_\perp(E_\parallel^b, \frac{E_\parallel - E_\parallel^b}{1-\alpha})$. The scale transformation $E_\perp = \frac{E_\parallel - E_\parallel^b}{1-\alpha}$ yields the second abscissa included in (d) and (e) and thus the distribution of transverse energies of the marked subensemble. It is seen that $N_\perp(E_\parallel^b, E_\perp)$ is narrow in case (b,d), while it extends from transverse energies of zero to

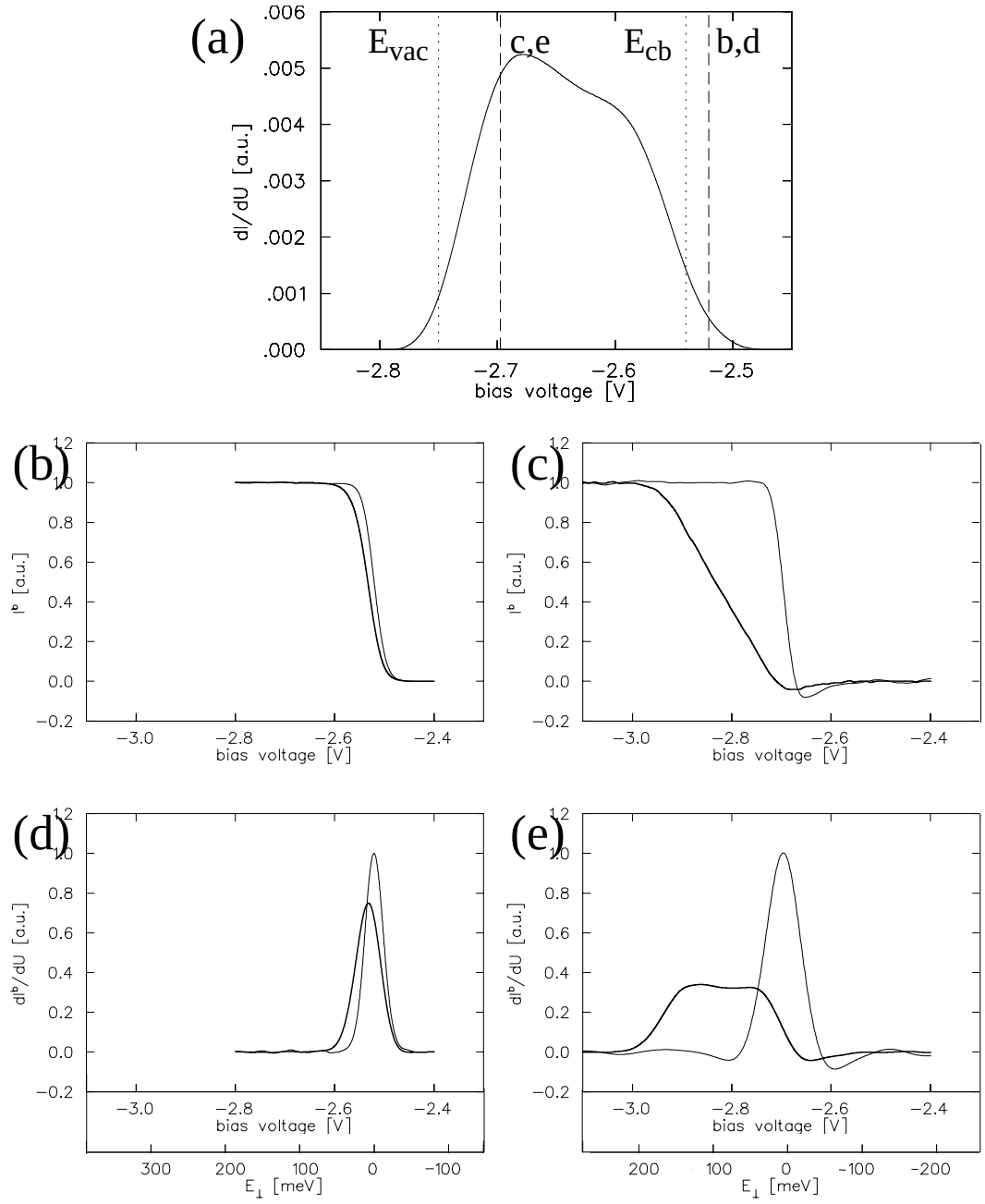

Figure 5.20: Examples for measurements of $N_\perp(E_\parallel^b, E_\perp)$: (a) Corresponding longitudinal EDC without applied blocking barrier. The longitudinal energies corresponding to the vacuum level, the conduction band minimum, and the two examples shown in (b-e) are marked by vertical lines. (b) and (c) show retarding curves for the case of α=1 (thin lines) and α=2.5 (thick lines). These curves are normalized to the same maximum. The corresponding derivatives are plotted in (d) and (e), respectively. They are normalized to the same integral. The transverse energy scale included is according to $E_\perp = \frac{E_\parallel - E_\parallel^b}{(1-\alpha)}$.

about 200 meV in case (c,e). The differential mean transverse energy (dMTE), defined as the mean transverse energy of electrons with a certain longitudinal energy, amounts to (11.2 ± 2) meV and (88.1 ± 2) meV, respectively.

The spectra measured at low barrier height, i.e. (c,e), show a slight negative contribution at longitudinal energies exceeding the barrier height. This is attributed to the non-ideal nature of the cutting barrier as discussed on page 50: The increase of transmission of higher energy electrons by an increase of the barrier height is phase-shifted by π with respect to the purposely marked electron current. This effect leads to a systematic error. The contribution, however, never exceeded 5% of the total integral signal. For higher $E_{\parallel}^{b}$ this effect reproducibly vanishes (see e.g. (b,d)). This can be explained by the fact that the ratio of electrons with longitudinal energies exceeding $E_{\parallel}^{b}$ to the amount of marked electrons drops drastically as $E_{\parallel}^{b}$ is increased.

The initial longitudinal energy is extracted as the first moment of the best fitted Gaussian to the derivative of the retarding curve measured in the case of α=1. This value also corresponds to the longitudinal energy complying with the height of the cutting barrier.

5.5 Resolutions and accuracies

Resolutions

The point spread function of the analyzing system for energy analysis in the longitudinal direction could be investigated by employing a longitudinally 'monoenergetic' electron beam, produced by a slightly modulated cutting barrier. Derivatives of the retarding curves of the marked electron current, measured by lock-in detection, are shown in figure 5.21. Curve (b) was measured under the same conditions as curve (a), just that the analyzer was cleaned by electron bombardment with 10 μA at 100 V for 20 minutes. The width of the curve is considerably decreased by this procedure. This width does not decrease further for decreased amplitudes of the modulation of the barrier height. Curve (b) is fitted well by a Gaussian with $\sigma_{\parallel}$=17 meV. The analyzer has been cleaned accordingly prior to the measurements reported in this thesis.

The remaining width of the longitudinal distribution can only partly be explained by the misalignment of the entrance diaphragm with the center of the retarding potential. The finite width of the electron beam which enters the analyzer through the entrance diaphragm, about 25 μm, leads to a spread of the *effective* retarding potential of about 5 mV if the center of the electron beam passes about 100 μm out of the radial minimum of the retarding potential (see figure 5.7). The remaining discrepancy could be resulting from a spread of the electron beam upon the passing of the entrance diaphragm caused by lens effects. Additionally, remaining pollution of the surfaces of the electrodes or asymmetries

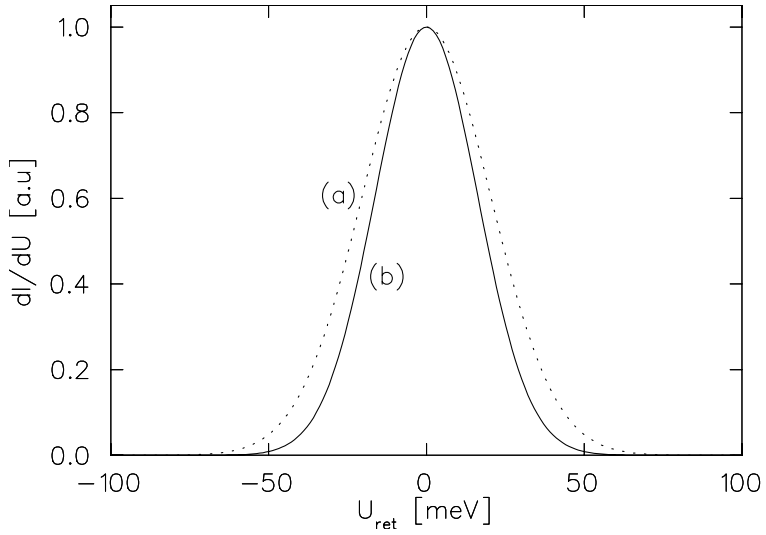

Figure 5.21: Longitudinal point spread function of the system of analysis (a) prior to, and (b) after electron bombardment of the analyzer with 10 μA at 100 V for 20 minutes. Curve (b) is fitted well by a Gaussian with $\sigma_{\|}$=17 meV. The retarding voltage is referred to the first moment of the narrowest curve.

resulting from the analyzer mounting system could lead to a deviation of the retarding potential from the ideal one. Clearly, further investigations are necessary to clarify this point. In particular a reconstruction of the analyzer in order to ensure the passing of the electron beam in a broad minimum of a retarding potential should prove advantageous in order to further increase the resolution of the system.

The resolution for the measurements of the initial *transverse* electron energy distribution of electrons with fixed longitudinal energy is, due to the relation $E_{\perp i} = (E_{\|f} - E_{\|i})/(1-\alpha)$ a factor of $|(\alpha - 1)|$ better, for the case of a compression to α=2.5 the transverse resolution is thus described by a Gaussian with $\sigma_{\perp} \approx$11 meV.

Several measures were taken to increase the signal to noise ratio: One of the most predominant noise sources was found to be the microphone effect in the short cable which connects the feedthrough for the connection of the collector electrode of the analyzer and the picoamperemeter, resulting from mechanical vibrations induced by the cooling water for the flat solenoid coils. This effect could be suppressed strongly by connecting the system to a different cooling cycle. Additionally damping vibrations, in particular near the analyzer and the pre-amplifier, by applying soft material, proved useful, as also the careful grounding of the set-up. By additionally adjusting the frequency used in the lock-in measurements to a value with low amplitude in the noise spectrum, to 203 Hz (previously about 1kHz), the signal to noise ratio could be further improved. The higher frequency

noise is probably caused by neighboring experimental set-ups, since its amplitude varied on a long time scale.

This noise reduction lead to a considerable increase of the dynamic range of the measurements of longitudinal energy distributions, which also serve for the determination of transverse energies of the photoelectrons. The system was previously operated [12, 13] in the collector current regime of typically 100 pA, still the measured EDCs had to be smoothed considerably. The measurements reported in this thesis were performed with collector current of the order of 10 pA or even slightly below. Even with these low currents the signal to noise ratio was well enough to usually require only very slight smoothing (if at all) of the measured longitudinal EDCs. Possible beam relaxation effects during the drift of the electron beam from the acceleration region to the analyzer were thus be further minimized, since the electron densities in the beam could be kept below 10^5 cm^{-3}.

Accuracies

As stated in section 5.2, the matching of the scale of retarding voltage and the absolute energy scale connected to the electronic conditions of the photocathode (e.g. the conduction band minimum) could be performed with an accuracy of $\pm$ 10 meV. The retarding voltage itself, as well as the acceleration voltage, were controlled with digital multi-meters with a reading accuracy of $\pm$ 1 meV. Adjustment of the corresponding power-supplies about one hour before the actual measurements proved to be useful to suppress long-term drifts of these voltages to approximately 1 meV per hour. The linearity of the ramp applied to the retarding electrode was found to be well fulfilled, such that the resulting error is below 1 meV and thus can be neglected. Furthermore, the longitudinal EDCs were well reproducible. Intensity fluctuations of the laser, which could lead to current densities varying during the course of a measurement of an EDC and thus influencing its first and higher moments, are thus negligible.

Aging of the photocathodes, leading to a increasing low-energy cut-off of the longitudinal EDCs due to the rising vacuum level and thus to an increase in the measured first moment, were also negligible. For stable activations the resulting shifts were much smaller than 1 meV during the course of a measurement. Measurements with applied cutting barrier should not be strongly affected by cathode aging, since in this case the low-energy cut-off, performed by this barrier, is usually much higher than the vacuum level. The corresponding correction procedure introduced by Pastuszka et al. [12] was thus not necessary to apply. The other advantage of that particular procedure, a minimization of statistical errors by averaging over several measured spectra, has become superfluous due to the strong reduction of noise mentioned above. The estimated error of the accuracy of the retarding voltage during the single measurements of $\pm$1.4meV (corresponding to the

combined reading accuracy) is thus conservative.

The initial transverse energies are determined from the shift of longitudinal energies of an electron (sub-) ensemble upon the expansion. Several factors could lead to an error in the measurement and will be discussed below:

1) beam relaxation effects

2) deviations of the experimental expansion parameter α from the calculated one

3) possible deviations of the energy spreads prior to expansion from the initial energy spreads of the photoemitted beam

4) artificial shifts of $E_{\parallel}$ due to changes of the angle of the electron beam inside the analyzer

1) Relaxation effects in the electron beam have been shown not to affect the measurement of mean transverse energies performed at current densities much higher than the ones used in the corresponding experiments reported in this thesis [12, 15].

For the determination of the *distribution* of transverse electron energies of electron beam subensembles with fixed longitudinal energy, the situation is more complicated, since the underlying equation is, strictly speaking, only valid for noninteracting electrons. Relaxation effects inside the electron beam, leading to a mixing of the marked subensemble with the rest of the electron beam (usually contributing the main part to the total current), are not understood well enough to be a priori excluded. The width of the derivatives of the retarding curves did, however, not change strongly within the range of the current densities used in the experiments reported in this thesis. The opposite should be the case if the mentioned 'mixing' effect is present. It is thus assumed that these relaxation effects are also not affecting the measurement of the transverse energy distribution of electrons with fixed longitudinal energy within the resolutions given by the discussion above.

2) The uncertainty of the exact expansion factor can be estimated by observing the change of the current density upon expansion. The measurement of the increase (decrease) of the collector current in the beam center for grounded retarding electrode, resulting from adiabatic transverse compression (expansion), yielded an accuracy of the adjustment of (1-α) of ± 2 %. These deviations could, however, also be enhanced by the analysis of different spots on the photocathode surface, since the respective current densities could change due to a slightly varying work function.

3) A possible deviation of the electron energy distribution prior to the expansion from the distribution of the initial photoelectron energies could be caused by non-optimum field configurations in the extraction region and the acceleration region. Transverse electric fields may result from non-optimum acceleration conditions or from the cutting barrier. The influence of the latter can, however, be neglected if the electron beam is analyzed on the beam axis. The statistical deviations in adjusting the analyzer diaphragm to the beam axis did not show any influence on the measured transverse energy distributions. On the other hand, distortions of the electric potential can also be caused by the cathode itself, in particular if the surface shows roughness. Since the surface is an equipotential plane, the electric field vector is, in this case, not aligned with the z-axis, leading to a transverse acceleration of the photoelectrons and thus to a transverse heating of the electron beam. Transverse electric field components may also be caused by slightly different work functions at different spots of the surface, since they lead to contact potentials. These effects should lead to a contribution to the transverse energy of the photoelectrons which is independent on the bulk temperature.

For cathodes which showed clean and mirror-like surfaces upon visual inspection and no, or very small, surface photovoltage effects, the results on transverse electron energies were well reproducible. Degraded cathodes, however, showed enhanced transverse energy spreads. The results thus have to be understood as cathode specific. The transverse energy spreads of subensembles of the electron beam with longitudinal energies above the value of $|\chi_{eff}|$ reproducibly showed to be close to the bulk temperature. In particular, the reduction of the latter from 300 K to about 90 K was accompanied by a lowering of the mean transverse energy well corresponding to this change. This observation proves that the influence of the effects discussed above is *not* a limiting factor in the determination of the initial energy spread of electron beams photoemitted from GaAs (down to the temperatures of liquid nitrogen), at least for properly prepared photocathodes.

4) The accuracy of the measurement of the shift in longitudinal energy upon expansion is mainly limited by the adjustment of the proper analyzer steerer currents. A detailed calibration of the right settings prior to each set of measurements would be too time consuming. The practical accuracy of the determination of the transverse energy as performed in this thesis is thus a compromise and limited to about ± 2 meV.

The overall error in the determination of the transverse energy is thus mainly resulting from two factors: A relative error of ± 2 % due to the inaccuracy of the exact expansion factor and an absolute uncertainty of ± 2 meV caused by a possible remaining change of

the angle of the electron beam inside the retarding field analyzer.

6. Results and discussion

This section presents and discusses the results obtained on the energy distributions of photoelectrons from NEA-GaAs. All measurements reported in this section were performed using reflection mode illumination. If not stated otherwise, the cathodes were cooled with liquid nitrogen ($T_{final} \approx 90$ K).

The first section concerns the longitudinal energy distributions, whereas results of the measurements of the mean transverse energy are discussed in section 6.2. Section 6.3 is dedicated to the results obtained by the new differential method, in particular the complete initial energy distribution of the photoelectrons. The closing section reports the photocathode lifetime under the practical vacuum conditions of the gun chamber.

6.1 Longitudinal energy distributions

Figure 6.1 shows examples of longitudinal EDCs recorded under current limited emission from the samples CR 59 (a) and CR 106 (b) at room temperature (thin lines) and after cooling to about 90 K (thick lines). The integral collector current in the cryogenic case amounted to about 10 pA. The figures show the raw data, no smoothing has been applied for the illustration of the good signal to noise ratio even at these low collector currents. In order to permit an easy comparison, the spectra are normalized for the same maximum. The positions of the conduction band minimum and of the vacuum level for the cryogenic case were determined as described in section 5.2.1. While cathode CR 106 was fully activated up to the saturation of the photocurrent, the activation was stopped at about 2.2 times the time of the first cesium-peak in case of CR 59 in order to investigate the changes inferred by a relatively thin activation layer. Both activations were the first activations after wet-chemical treatment of the cathodes, explaining the relatively low QY for the full activation (see table 6.1). The cathodes were both annealed at 580°C, corresponding to a Ga-stabilized surface reconstruction [66, 30]. For simplification, the combinations of the samples and these particular activations will be referred to in this chapter only by stating the name of the sample.

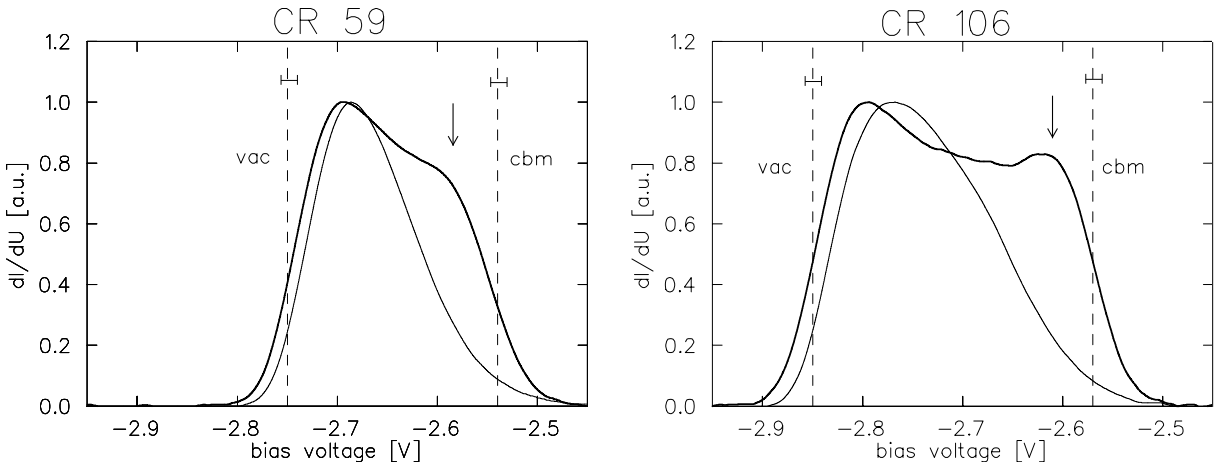

Figure 6.1: Longitudinal EDCs (raw data) measured at 90 K with infrared illumination for full extraction with (a) sample CR 59 and (b) sample CR 106. Longitudinal EDCs recorded at room temperature prior to the cooling are included as thin curves. The curves are normalized to the same maximum. The integral collector current amounted to about 10 pA. The position of the vacuum level and of the conduction band minimum for the cryogenic case are indicated as vertical lines denoted 'vac' and 'cbm', respectively. The arrows indicate the estimated position of the high-energy peak after subtraction of a continuous background.

The longitudinal EDCs obtained at low temperatures are in good qualitative agreement with the ones obtained in other studies [67, 32, 34]. Several features can be separated and are discussed below, including the influence of the cooling of the crystal:

- The most obvious change of the longitudinal EDCs upon cooling is the considerable increase in width. The shift of the vacuum level, representing the shift of the low-energy cut-off, amounts to approximately 10 meV. A similar shift was observed in [32] and assigned to small changes of the work function of the cathode. The dominant effect is the shift of the high-energy cut-off; it is caused by the increase of the band gap ($\Delta E_{gap} \approx$80 meV for cooling from 300 K to 90 K, see e.g. [57]). As a result, $|\chi_{eff}|$ increases, leading in turn to an increase of QY.

  The values of $|\chi_{eff}|$ and the increase of the photocurrent at constant light intensity observed when cooling the photocathodes are summarized in table 6.1.

- A structure is clearly seen in the spectra recorded at 90 K: A shoulder at the high energy side of the EDC appears already in case (a), and a peak is clearly resolved in case (b). These features can be estimated to be (45±10) meV (a) and (40±10) meV (b) below the determined position of the conduction band minimum,

case	cathode	$\lvert\chi_{eff}\rvert$ at 90 K	$\lvert\chi_{eff}\rvert$ at 300 K	QY_{670nm}^{300K}	$I_{tot}^{90K}/I_{tot}^{300K}$
(a)	CR 59	$\approx$ 210 meV	$\approx$ 120 meV	$\approx$ 10%	$\approx$ 1.4
(b)	CR 106	$\approx$ 280 meV	$\approx$ 215 meV	$\approx$ 16%	$\approx$ 1.25

Table 6.1: Characteristics of the two cathodes used in the measurements shown in figure 6.1. The initial QY was measured in the preparation chamber under reflection mode illumination while the current increase upon cooling denotes the ratio of photocurrents prior and after cooling obtained under the same (low) IR illumination powers.

which, however, also has an accuracy of $\pm$10 meV. The more evident appearance in case (b) is probably caused by the higher value of $\lvert\chi_{eff}\rvert$.

The peak position is in reasonable agreement with the observed peak position in [34] ($\approx$35 meV below CBM, see figure 2.5). In that study also the position of the highest two-dimensional quantized sub-band in the band bending region was calculated to be about 20 meV below CBM (for photocathode structures with similar material parameters as the ones used in the present thesis). The peak might thus possibly be assigned to the highly effective capture of electrons at the bottom of the conduction band by a two-dimensional sub-band in the band bending region and the subsequent emission to vacuum from there[1].

The rather pronounced second peak resolved in the case of high $\lvert\chi_{eff}\rvert$ (b) at about 200 meV below the one at higher energies was not observed in [32, 34]. $\lvert\chi_{eff}\rvert$, however, was smaller in those studies. Spectra published in [67], which were recorded at liquid nitrogen temperature with high $\lvert\chi_{eff}\rvert$, show such a structure also about 200 meV below the first peak. Calculations [34] indicated this position in longitudinal energy for the second quantized level in the band bending region. It might thus be that a second two-dimensional sub-band contributes to the photoemission for high values of $\lvert\chi_{eff}\rvert$.

Peculiarities in the derivatives of longitudinal EDCs measured at liquid nitrogen temperatures observed in another study [32] could not be resolved in this system: The EDCs are broadened by the point spread function of the analyzer which is in good approximation Gaussian with a $\sigma_{\parallel}$ of about 17 meV, as shown in chapter 5.5. In the mentioned study, a vacuum photo-diode was used in the measurements, and the resolution was better than $\sigma \approx$10 meV [65].

- A further change of the longitudinal EDCs upon cooling is the increase of the slope

[1] The band bending is not affected strongly anymore in the later stage of the activation [26], such that a different position of the subband due to the differently activated cathodes would not be expected.

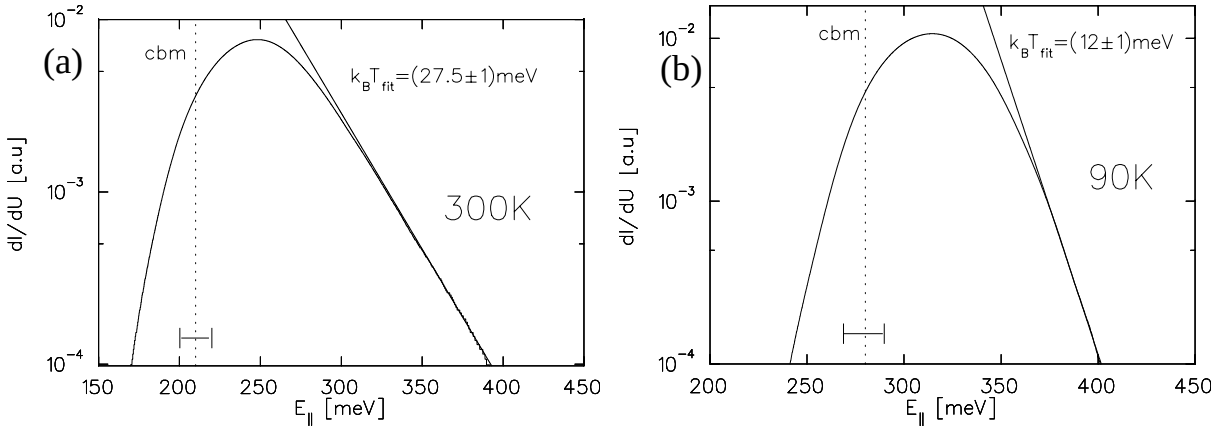

Figure 6.2: Longitudinal EDCs measured with applied cutting barrier in order to reach a considerable signal at high longitudinal energies without strong increase of the total current. The longitudinal energy is referred to the vacuum level. (a) Room temperature measurement, (b) measurement at 90 K. The high energy tail is fitted well by a Maxwell-Boltzmann function with k_BT close to the cathode temperature. The integral collector current amounted to 5.6 pA and 17.34 pA, respectively.

of the high energy tail. In order to accurately determine the slope of these tails and thus the longitudinal temperature of the contributing electrons, spectra were recorded with increased light intensity and applied cutting potential. By doing so the signal related to these high energy electrons can be enhanced without increasing the total current, which, in turn, often showed to be reducing the photocathode lifetime. Figure 6.2 shows examples for a room temperature measurement (a) as well as data obtained from a cathode cooled with liquid nitrogen (b). The high energy slope is in good approximation exponential, the characteristic temperatures amount to (27.5±1) meV and (12±1) meV. These values were, within the given accuracy, reproduced in other cases of stable activations. The value measured at 300 K is in reasonable agreement with the temperature ($k_BT_{RT} \approx 25$ meV), whereas the value obtained in the low temperature regime significantly exceeds the theoretical value of $k_BT_{90\ K} \approx 7.8$ meV. These differences are, however, in good agreement with the values found in other studies [4, 32] in which the temperature was determined the same way. For instance, [32] reports an excess energy of 2.5 meV at liquid nitrogen temperature and 4 meV at room temperature. These differences are, however, not yet understood.

Figure 6.3 shows two longitudinal EDCs measured at 90 K under illumination with the red laser (λ=685 nm). The tail of photoemitted hot electrons extending to the initial

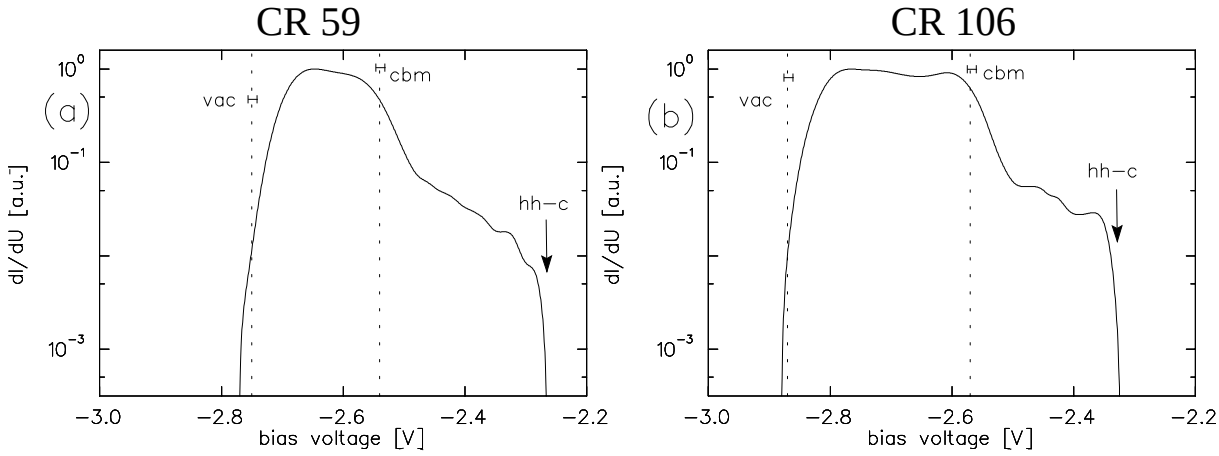

Figure 6.3: Longitudinal EDCs measured at 90 K under illumination with a red laser (λ=685 nm). (a) Sample CR 59, (b) sample CR 106. The positions of the conduction band minimum (cbm) and the vacuum level (vac) are indicated by lines. The arrows (hh-c) denote the initial energy of electrons excited from the heavy-hole band.

energy of electrons excited from the heavy-hole band is clearly resolved.

6.2 High accuracy measurements of MTE at cryogenic cathode temperatures

Figure 6.4 (a) shows an assortment of longitudinal EDCs recorded for different settings of the cutting potential barrier height. The corresponding changes of the low energy cut-off and of the mean longitudinal energy $\langle E_{\parallel} \rangle$ are easily identified. The light intensity was kept constant for the first six curves with increasing cutting, but it was changed for the following curves. Hence, the latter have been rescaled by arbitrary factors for better visibility of the shift of the mean longitudinal energy.

The mean transverse energies of the respective subensembles, measured by adiabatic transverse compression to α=2.5, are plotted in figure 6.4 (b) as a function of $\langle E_{\parallel} \rangle$ in the case of α=1 (i.e. the initial MLE). Similar to the data obtained at room temperature by Pastuszka et al. [12, 13], $\langle E_{\perp} \rangle$ decreases quite linear as $\langle E_{\parallel} \rangle$ increases. At a mean longitudinal energy corresponding to the value of $|\chi_{eff}|$ (and thus to the position of the conduction band minimum), a distinct change is observed: For further increased $\langle E_{\parallel} \rangle$, $\langle E_{\perp} \rangle$ reaches a constant value. The value of $\langle E_{\perp} \rangle$ in this case is in the vicinity of the bulk temperature; the latter is denoted as a horizontal line.

Figure 6.5 (a) shows a summary of the results obtained from the cathodes CR 59 and CR 106. For a better comparison of the data from the two cathodes, $\langle E_{\parallel} \rangle$ is referred to the conduction band minimum.

For each cathode two values obtained at room temperature directly before the cooling

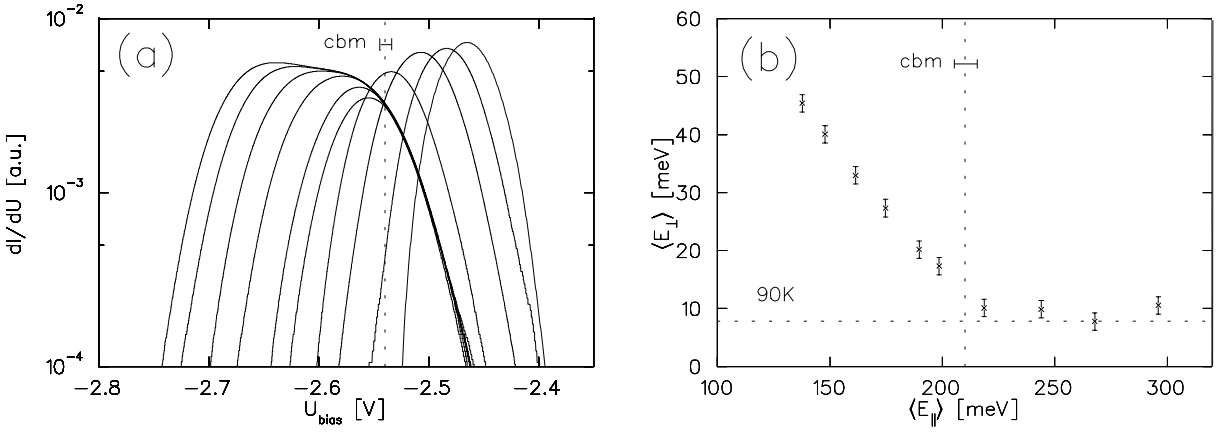

Figure 6.4: (a) Assortment of longitudinal EDCs measured with increased cutting barrier height on sample CR 59. The four EDCs with the highest mean longitudinal energy have been rescaled by arbitrary factors for better visibility. (b) Corresponding values of $\langle E_{\perp} \rangle$ as a function of the mean longitudinal energy which is referred to the vacuum level.

are included. The mean longitudinal energy (referred to the CBM) of these data points has a higher inaccuracy than the low temperature ones: The longitudinal energy scale at room temperature could not be determined with reasonable accuracy by the methods applied at cryogenic temperatures since the energy distribution of photoemitted hot electrons is smoothed due to the stronger phonon scattering at elevated temperatures. Instead, the longitudinal energy scale was obtained by shifting the position of the conduction band minimum (determined in the cryogenic case) down by 80 meV; this is with high precision (about ± 2 meV) the change of the band gap with the respective temperature change.

Since the intensity of the high energy tail is increased at high temperatures, it was possible to measure at considerably higher mean longitudinal energies. The corresponding values are near the lattice temperature and thus in good agreement with the data obtained by Pastuszka et al. [12, 13]. The room temperature data at low $\langle E_\parallel \rangle$ was obtained under full extraction and thus represents $\langle E_\perp \rangle$ of the complete photoemitted electron ensemble. Curiously, it is clearly seen that the values for $\langle E_\perp \rangle$ obtained under full extraction (data at lowest $\langle E_\parallel \rangle$) are increased considerably with the cooling of the emitters to 90 K.

The general behavior of the data is well described by a mean transverse energy corresponding to the cathode temperature for $\langle E_\parallel \rangle$ above the conduction band minimum and by a linear increase of $\langle E_\perp \rangle$ below. The slope of this line indicates that the increase in $\langle E_\perp \rangle$ is about half the decrease in $\langle E_\parallel \rangle$. Since the initial electron energy is approximately the value of $|\chi_{eff}| + k_B T$, this leads to the conclusion that energy loss takes place; hence inelastic processes contribute to the emission process of the electrons with longitudinal emission energies below $|\chi_{eff}|$. Also the room temperature data indicate the same slope. The higher values at room temperatures could be caused by the higher starting positions of these electrons in the bulk due to the higher temperature or by a higher probability of elastic scattering. This is in contradiction with the slope about unity determined in [12, 13]. In these studies, however, very few data points were obtained for each particular activation. In addition, the procedure by which the position of the conduction band minimum was determined was of a more approximate nature which possibly partly explains this discrepancy: The data obtained for the *separate* activations in these studies (see figure 2.6 on page 16) could also be taken as indicator of a slope as the one found in the present thesis.

For $\langle E_\parallel \rangle$ below $|\chi_{eff}|$, the values of $\langle E_\perp \rangle$ apparently differ for the two cathodes. This could, in particular, be caused by surface roughness or compositional disorders of the activation layer, leading to a transverse heating of the emitted electron beam due to transverse electric fields. This contribution should be temperature-independent. The similarity of

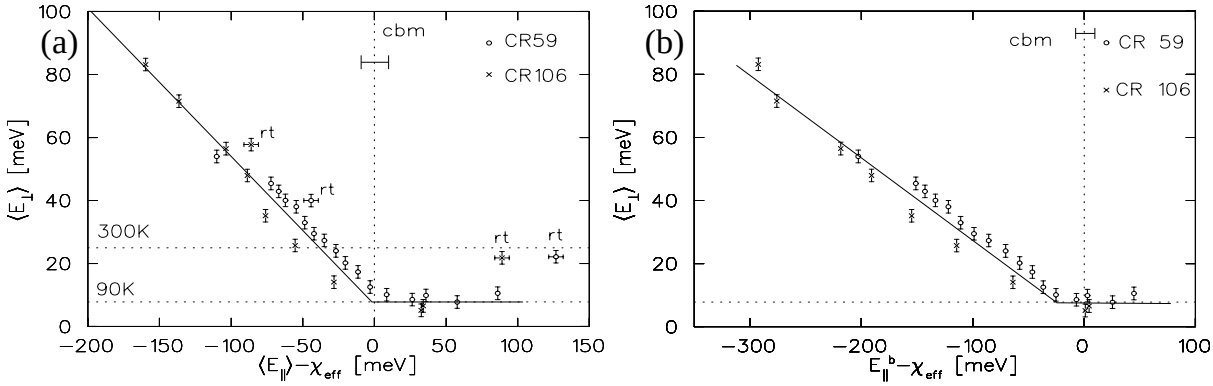

Figure 6.5: Values of $\langle E_\perp \rangle$ obtained from measurements with two different samples as a function of the mean longitudinal energy (a) and of the longitudinal energy $E_\parallel^b$ corresponding to the cutting barrier height (b). In order to compare the data, the longitudinal energy scale is referred to the conduction band minimum. The solid lines are drawn to guide the eye. Four points measured at room temperature are included in (a), marked by 'rt'.

the slope indicates another possible explanation: The relatively low accuracy of the determination of the conduction band minimum can be visualized as an uncertainty of the placement of the sets of data points obtained from different samples in the horizontal scale of mean longitudinal energies. The inaccuracy of ±10 meV for the determination of the CBM for one sample could thus contribute to the deviation of the data in the low $\langle E_\parallel \rangle$ regime.

The mean transverse energy of electrons with longitudinal energies above the conduction band minimum is, in general, in good agreement with the lattice temperature of the crystal also at 90 K, in contrast to the higher values (about 14 meV) reported by Pastuszka et al. [12, 13]. This deviation is probably caused by the increased accuracy achieved in the measurements reported here. Nevertheless, the values obtained are about 3 meV higher for CR 59 than for the other sample, indicating that influences of the semiconductor surface may be important.
The mean transverse energy obtained in the room temperature measurements ((22.5±2) meV) as well as in the cryogenic case of CR 106 ((5.5±2) meV) are even slightly below $k_B T$. This behavior was also found in some results obtained at room temperature in [12] and could indicate a (partial) presence of a sub-thermal emission process. Clearly, further investigations are necessary to clarify this point.

For practical purposes it is advantageous to know the dependence of $\langle E_\perp \rangle$ on the cutting

barrier height. This parameter is now accessible by a determination of the cutting barrier height as presented in chapter 5.4. Figure 6.5 (b) shows the data of mean transverse energy at 90 K as a function of the longitudinal energy corresponding to the cutting barrier height which is referred to the position of the conduction band minimum in the bulk. It is seen that the mean transverse energy stays within the range of k_BT as long as the cutting barrier is placed higher than about 20 mV *below* the conduction band minimum. The comparison with the respective longitudinal EDCs (see figure 6.1) shows that the gain of *effective* quantum yield is considerable compared to the case when only electrons with longitudinal energies above $|\chi_{eff}|$ are extracted. The *effective* QY in this case amounts to about 6% of the total QY, determined as the ratio of the collector current in the case of the application of this particular cutting barrier height and in the case of full extraction. The difference of this ratio for the two cathodes is negligible. Hence CR 106 has a higher effective QY, since it has a higher overall QY. This could indicate that a full activation is better suited for an effective source of cold electrons. The data, however, is too scarce to thoroughly address this point. Further studies are planned to be performed subsequent to this thesis.

6.3 Differential energy analysis of photoelectron beams from NEA-GaAs

This section is devoted to the results obtained with the new differential method and the resulting insights on the photoemission from NEA-GaAs. For the sake of presentation, section 6.3.1 is dedicated to the differential energy distributions at fixed longitudinal emission energy. The data obtained in these measurements is, however, only partly discussed in that section, since the reconstructed two-dimensional energy distributions $N(E_\parallel, E_\perp)$ yield more detailed information. They are discussed in section 6.3.2.

6.3.1 Differential transverse energy distributions

Examples of the transverse energy distribution of electrons within a narrow interval of longitudinal energies under infrared illumination of the cathode have already been shown in chapter 5.4 on page 67. The width of the distribution was smaller for higher longitudinal energies. The general nature of this trend is easily recognized in the summary of the data obtained on CR 106, presented in figure 6.6 (a). Results for red laser illumination of CR 106 are shown in figure 6.6 (b). The data was rebinned for presentation, data analysis was performed in meV-steps. The transverse energy distributions for different longitudinal energies are normalized such that

$$\int dE_\perp \cdot N_\perp(E_\parallel^b, E_\perp) = 1 \text{ for all } E_\parallel^b. \tag{6.1}$$

To obtain these data, the height of the cutting/marking barrier was subsequently raised with a step-width of about 20 mV, and the transverse energy distribution of the subensemble with the corresponding longitudinal energy was measured employing an adiabatic transverse compression to α=2.5. The range of longitudinal energies which could be covered by this method was limited both on the high energy and on the low energy side by the requirement of a reasonable signal to noise ratio. These limits restricted the measurements to longitudinal energies between about 50 meV above the vacuum level and typically 100 meV above the conduction band minimum in the case of infrared illumination.

Due to the higher contribution at longitudinal energies above the conduction band minimum (see figure 6.3), measurements in the case of red laser illumination could be performed up to the longitudinal energy corresponding to the emission of ballistic electrons excited with λ=685 nm, i.e. about 240 meV above the CBM. They were continued down to a longitudinal energy of about the value of $|\chi_{eff}|$, i.e. to the position of the

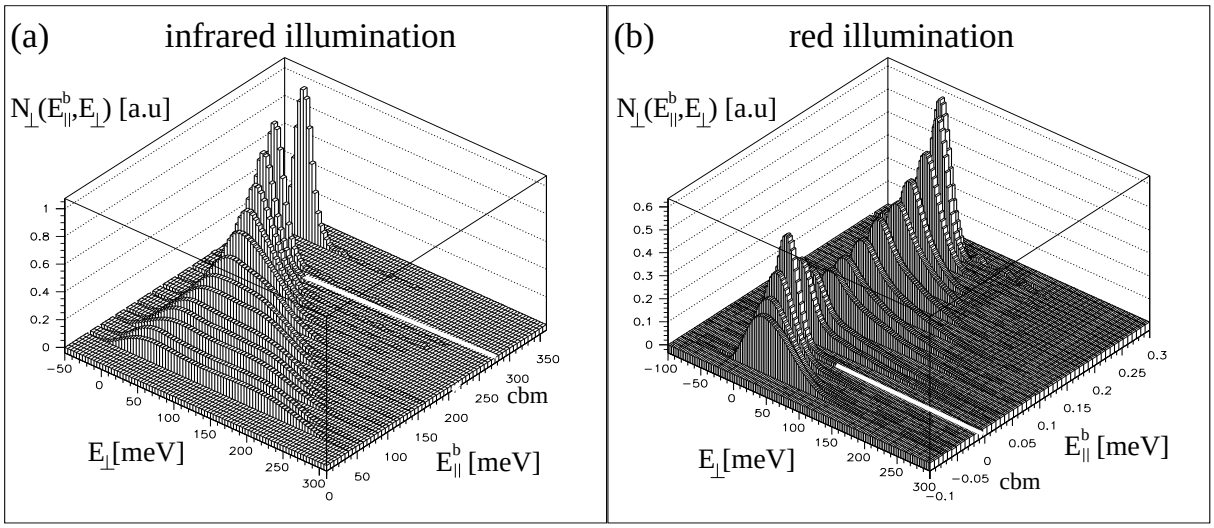

Figure 6.6: Lego plots of the measured transverse energy distributions $N_\perp(E_\parallel^b, E_\perp)$ of electrons with fixed longitudinal energy $E_\parallel^b$ photoemitted from cathode CR 106. All curves are normalized to same value of $\int dE_\perp \cdot N_\perp(E_\parallel^b, E_\perp)$. The position of the conduction band minimum is indicated by a solid white line (cbm). (a) Infrared illumination, (b) red light illumination. The longitudinal energy is referred to the vacuum level (conduction band minimum) in case (a) ((b)).

conduction band minimum.

Infrared illumination

In the case of infrared illumination it is seen that $N_\perp(E_\parallel^b, E_\perp)$ is narrow for $E_\parallel^b > |\chi_{eff}|$, and broadens significantly for $E_\parallel^b$ below this value. In the latter case the distributions extend from about $E_\perp = 0$ to a bisecting line in the $E_\parallel^b - E_\perp$ plane, corresponding to a constant total energy.

The data obtained by the differential analysis does in particular allow the extraction of the differential *mean* transverse energy (dMTE) for electrons with fixed longitudinal energies. These results are presented in figure 6.7 as a function of the longitudinal energy corresponding to the marking barrier height. This, in turn, represents the longitudinal energy of the respective electrons. To permit easy comparison, the longitudinal energy is referred to the conduction band minimum ($E_\parallel^b - \chi_{eff}$).

The dMTE has a constant value of about k_BT for electrons with longitudinal energies above the conduction band minimum. For low longitudinal energies, the dMTE amounts to about half the value of $E_\parallel^b - |\chi_{eff}|$, i.e. the energy lost in the longitudinal degree of freedom (referred to the initial value of $|\chi_{eff}| + k_BT$) is converted to transverse energy on

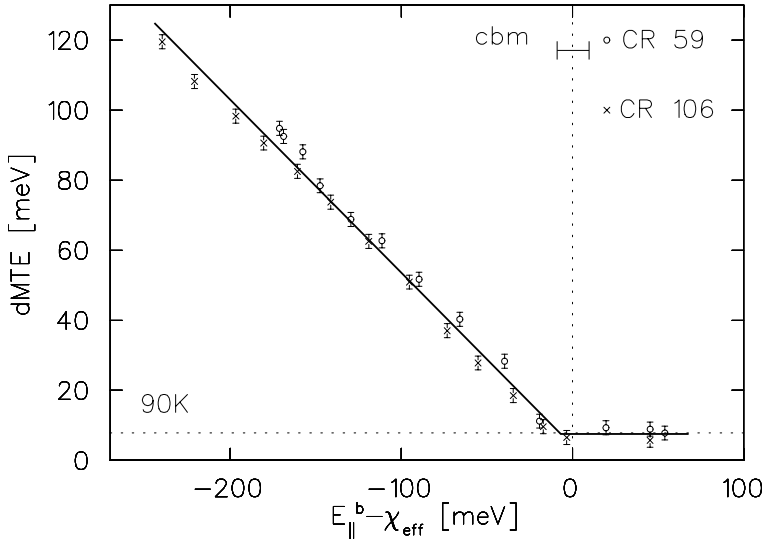

Figure 6.7: Summary of dMTE-results for different cathodes. For comparison the longitudinal energy is referred to the CBM. The solid line is drawn to guide the eye.

the average only by about 50%. This result again proves the considerable contribution of energy loss mechanisms during electron transfer through the semiconductor-vacuum interface. Similar to the data obtained by the integral MTE-method, the data for longitudinal marking energies slightly below the conduction band indicates that a considerable increase in dMTE with decreasing longitudinal energy only starts slightly below CBM.

The data show, similar to the low longitudinal energy measurements of MTE, increased values for the sample CR 59. This result may be explained by the same reasons as in the stated case: An error in the determination of the position of the conduction band minimum would lead to a horizontal shift of the data, possibly leading to a better matching. On the other hand, this increase could be caused by stronger scattering mechanisms in the case of CR 59 and by a transverse heating of the electrons emitted from this sample due to transverse electric fields, which could, in turn, be resulting from surface roughness or chemical inhomogeneities of the semiconductor surface and/or the activation layer.

Red laser illumination

The values of dMTE obtained under illumination with a red laser (λ=685 nm) are shown in figure 6.8. The range of $E_{\parallel}^{b}$ covered in these measurements exceeds the maximum energy of the excited electrons obtained from the calibration procedure. This is due to two effects: Firstly, the initial energy distribution is broadened by phonon interaction [27], and secondly the calibration procedure applied uses the average mass of the heavy holes. Electrons excited from a direction of the heavy-hole band with a higher mass have higher

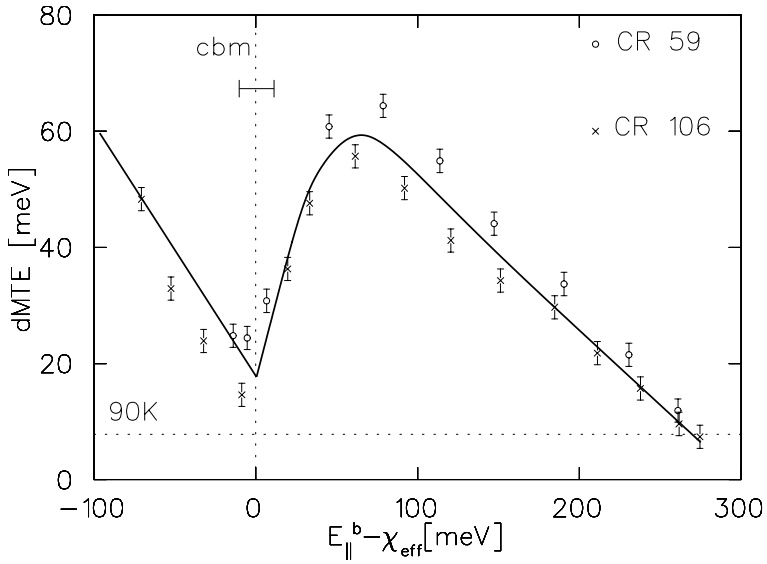

Figure 6.8: Summary of dMTE-results for red laser illumination. Different plot characters denote different cathodes. The longitudinal energy scale is referred to the conduction band minimum (cbm), the solid line is drawn to guide the eye.

initial energies. These electrons thus contribute to the yield at high longitudinal energies.

It is seen that the dMTE is low for longitudinal energies at about 240 meV above the conduction band minimum. This is easily understood since this point is close to the maximum energy electrons could gain due to the excitation with the stated laser wavelength. Energy conservation demands that electrons with a longitudinal energy of this (or close to this) value do not have high transverse energy. The increase in transverse energies with decreasing longitudinal energy is lower than unity as would be expected from constant total energy prior to the emission. This is qualitatively understood by the fact that also electrons contribute to the emission at $E_{\|} = E_{\|}^{b}$ which lost a part of their initial energy in the bulk. The trend of increasing dMTE with decreasing $E_{\|}^{b}$ is counteracted as the longitudinal energy approaches the vicinity of the conduction band minimum. This fact can be understood regarding the results obtained for the longitudinal energy distribution and the normalized complete distribution (see below) for electrons with energies in this range: The mean transverse energy of non-relaxed and non-thermalized electrons is further increased, the yield at a fixed longitudinal energy is, however, more and more dominated by the contribution of electrons which relaxed and thermalized at the conduction band minimum prior to the emission. Their energy distribution should, in turn, correspond to the data obtained in the case of infrared illumination. The data obtained for longitudinal energies below CBM (sample CR 106) is in line with this interpretation, since the dMTE rises, as in the referred case, with a slope of about 1/2 for decreasing $E_{\|}^{b}$.

The coincidence of the longitudinal energy at a minimum value of dMTE with the position of the CBM furthermore indicates a low deviation in the determination of the longitudinal energy scale. This fact, as well as the systematically higher values for CR 59, support the interpretation that the transverse energies of the photoelectrons emitted from this cathode are enhanced due to effects of the semiconductor-vacuum interface and/or the emitter surface.

Reconstruction of the two-dimensional energy distribution

The changes of the distributions of transverse energies as $E_{\parallel}^{b}$ is varied by this step-width are continuous. The data were thus interpolated. This was performed by fitting the data binned in meV^2-bins of transverse and longitudinal energies for all respective transverse energies by cubic splines under a given maximum tension. The resulting data were normalized according to condition 6.1. Figure 6.9 shows the interpolated data obtained by the application of this procedure on the distributions measured for sample CR 106.

In the case of infrared illumination an extrapolation over the relevant range of longitudinal emission energies (corresponding to the range of the longitudinal EDC) was performed as the next step in the data analysis. No extrapolation was undertaken in the case of red laser illumination, since the fraction the interesting hot photoelectrons contribute to the total yield is very small.

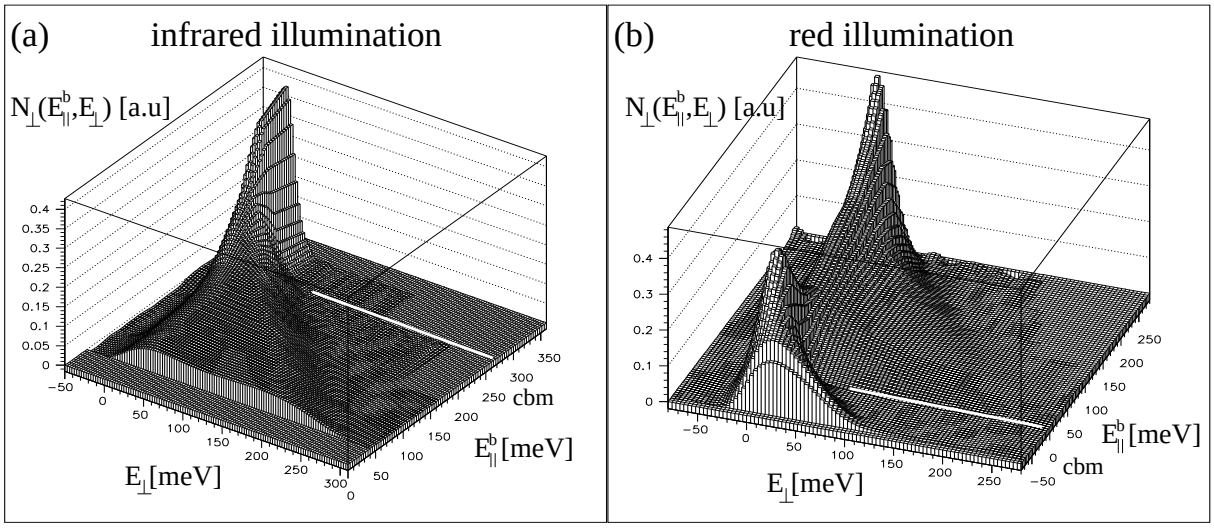

Figure 6.9: Lego plots of the interpolated distributions $N_{\perp}(E_{\parallel}^{b}, E_{\perp})$ for CR 106. The position of the conduction band minimum is indicated by a solid white line (cbm). (a) Infrared illumination, $E_{\parallel}^{b}$ referred to the vacuum level, and (b) red laser illumination, $E_{\parallel}^{b}$ referred to the conduction band minimum.

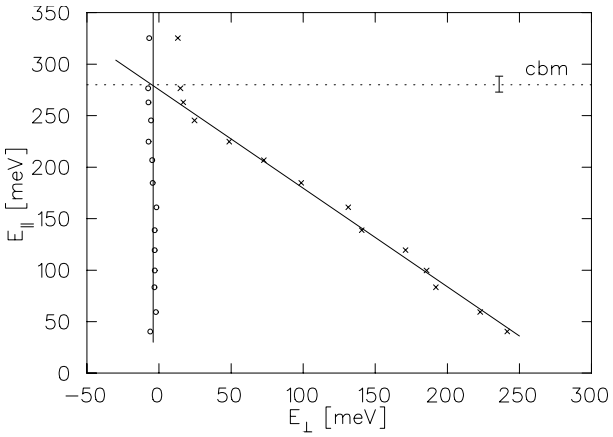

Figure 6.10: Positions of the turning points of the measured differential transverse energy distributions $N_\perp(N_\parallel^b, E_\perp)$ at different longitudinal energies $E_\parallel^b$. The solid lines were fitted to the data more than 20 meV below the conduction band minimum. Whereas it represents a linear fit in the case of the high $E_\perp$-wing, the mean value is indicated for the wing at low $E_\perp$. The position of the conduction band minimum is indicated as a horizontal line (cbm).

The extrapolation consisted of a simple continuation of the data for high longitudinal energies: $N_\perp(E_\parallel^b, E_\perp)$ was assumed to be constant and equal to the distribution for the highest $E_\parallel^b$ measured. The unchanging behavior of the transverse energy distribution in this regime is a reasonable assumption since the measurements reported earlier in this chapter as well as in previous studies [12, 13] indicate a transversely constant distribution of photoelectrons for longitudinal energies above the conduction band minimum. Furthermore, the relative contribution of electrons with longitudinal energies exceeding the maximum reached in the measurements (at least 60 meV above CBM) is very small, as can be seen in figure 6.1. Thus the error induced in the reconstructed two-dimensional energy distribution is negligible, even if the model used for the extrapolation is slightly wrong.

The extrapolation to lower longitudinal energies was performed regarding the change of the turning points of the measured transverse energy distributions for longitudinal energies below the conduction band minimum. This data is shown in figure 6.10.

The turning points corresponding to the wings at low transverse energies were in reasonable approximation at a constant value of transverse energy about zero. The turning points corresponding to the high $E_\perp$ slope could be described well by a line of constant total energy, i.e. $E_\perp + E_\parallel = const.$ The extrapolation to low longitudinal energies was thus performed as point-projection of the transverse energy distribution obtained at the

lowest measured longitudinal energy from the crossing point of the fits for the turning points onto the desired line of constant longitudinal energy. This was followed by a normalization according to condition 6.1. This extrapolation procedure is less evident than the one for the high energy tail. However, the continuous change in the transverse energy distribution for low longitudinal energies and the good agreement of the values of $\langle E_\perp \rangle$ measured for full extraction with the trend observed with a cutting barrier employed (see figure 6.5) makes the assumption of low deviations of the real distribution from this model very plausible. Furthermore, the fraction of electrons emitted with longitudinal energies out of the interval covered with the measurements is already low. Thus the induced error in the obtained total energy distribution seems acceptable.

Since the distributions of longitudinal energies $N_\parallel(E_\parallel)$, i.e. the longitudinal EDCs, are well known, they can be used as a weighting function. This yields the complete, two-dimensional energy distributions $N(E_\parallel, E_\perp)$, which are discussed in the following section.

6.3.2 Two-dimensional energy distributions

The results obtained under infrared illumination and red laser illumination of the photocathodes are discussed in separate sections.

Infrared illumination

It is instructive to first discuss the data on the basis of the density plots shown in figure 6.11. It can easily be recognized that the main part of the distribution is contained in an area limited by the vacuum level, a line corresponding to zero transverse energy and an upper limit of the total energy (bisecting lines) slightly above the value of $|\chi_{eff}|$. The difference in $|\chi_{eff}|$ for the two cathodes is clearly visible.
A further characteristic is a tail of electrons with low transverse energy at longitudinal energies exceeding the position of the conduction band minimum.

The lego plots of the distributions (figure 6.12) show a distinct peak at low transverse energies and at a longitudinal energy slightly below the conduction band minimum. The exponential tail with a slope of about $k_B T_{eff}$ ≈12 meV at longitudinal energies above the conduction band minimum is also recognized easily. At lower longitudinal energies, the distribution evolves to a kind of plateau. The ratio of the peak-height to the height of the plateau, however, differs in the two cases. Whereas for CR 59 it amount to approximately

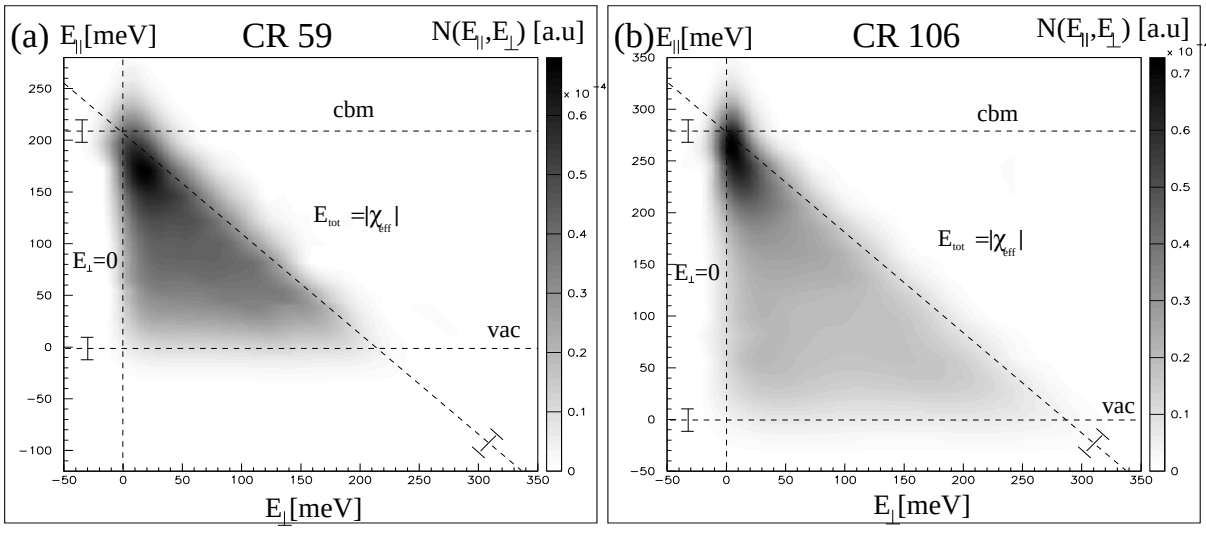

Figure 6.11: Density plots of the two-dimensional photoelectron energy distributions $N(E_\parallel, E_\perp)$ obtained under infrared illumination. The vacuum level (vac), the conduction band minimum (cbm), the line of $E_\perp$=0 and a line of constant total energy of the value of $|\chi_{eff}|$ are indicated as dashed lines. (a) Sample CR 59 and (b) sample CR 106.

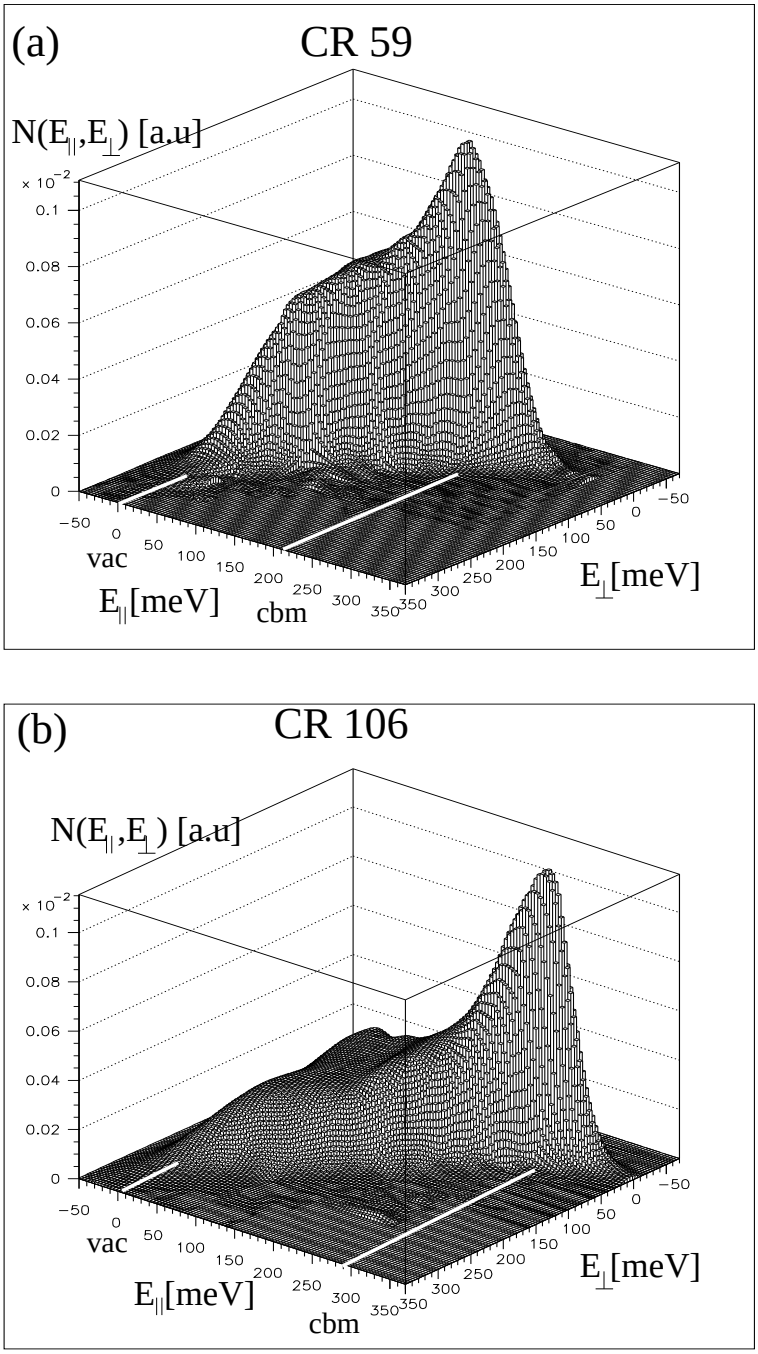

Figure 6.12: Two dimensional photoelectron energy distributions $N(E_{\|},E_{\perp})$ for infrared illumination of (a) CR 59 and (b) CR 106. The positions of the vacuum level (vac) and the conduction band minimum (cbm) are indicated as solid white lines.

2, it is strongly increased to about 4-5 in the case of CR 106.

The data indicate the contribution of different processes to the photoemission:

- The exponential tail at high longitudinal energies contains electrons which are ap-

proximately thermalized with the bulk material. Thus it seems that these electrons cross the semiconductor-vacuum interface without (strong) interaction.

- The extension of the plateau from zero transverse energies to a value of constant energy slightly above $|\chi_{eff}|$ indicates the contribution of elastic as well as inelastic scattering processes. The electrons at low both transverse and longitudinal energies suffered losses in total energy during the emission process. The electrons contributing to the wing on the high transverse energy border did not loose energy (in a considerable amount). They did rather undergo elastic scattering, leading to a change of the emission angle and thus to a transfer of longitudinal energy to the transverse degree of freedom. The mechanisms responsible for the energy losses are still controversial. The only proved mechanism is phonon emission ([34], see also figure 2.5 on page 15). Possible further mechanisms include, besides a scattering by surface defects, a temporal trapping in surface states and a subsequent emission into vacuum. Due to the localized nature of some of these states the angular distribution of the emitted electrons could be quite isotropic.

- A distinct peak appears at longitudinal energies slightly below the conduction band minimum. The longitudinal energy is about (40±10) meV ((20±10) meV) below the determined position of the conduction band minimum in case of CR 59 (CR 106). The transverse energy amounts to (17±5) meV and (5±5) meV, respectively. It thus seems that the electrons contributing to this feature lost an energy of about 30-40 meV in comparison to their starting position at the bottom of the conduction band minimum. Possibly an efficient energy loss mechanism leads to this high contribution of electrons with these energies.

  The peak positions in the longitudinal energy scale are, however, also in reasonable agreement with the calculated position of the highest two-dimensional sub-band in the band bending region [34]. Thus this peak might possibly be explained by the model [34, 13] which proposes an effective capture of electrons by the two-dimensional quantized sub-band in the band bending region, since the (longitudinal) starting position of a large subensemble of electrons would, in this case, correspond to the longitudinal energy of this level.

  The observed peak width is about the resolution reached in the experiments. Further details could thus not be revealed. Broadenings in the longitudinal energy scale could result from the statistical nature of the dopant distribution [68] and thus from a broadened position of this level over the cathode surface. In addition, the peak could be broadened by electron scattering during the transfer through the activation layer or effects of the non-ideal nature of the surface.

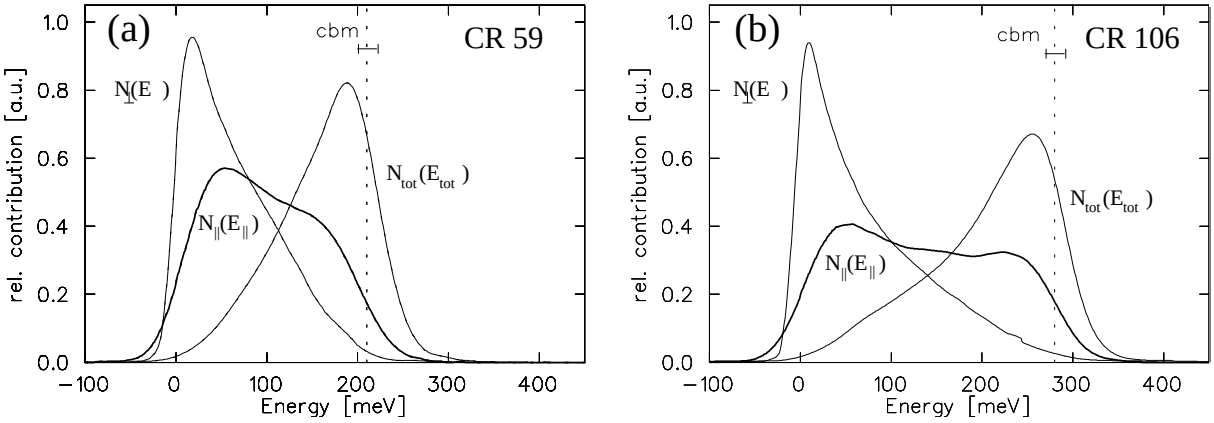

Figure 6.13: Distributions of photoelectrons as a function of total (E_{tot}), longitudinal ($E_{\parallel}$) and transverse ($E_{\perp}$) initial energy, obtained from the complete photoelectron energy distribution $N(E_{\parallel},E_{\perp})$ for (a) CR 59 and (b) CR 106.

cathode	$\lvert\chi_{eff}\rvert$	$\langle E_{tot}\rangle$	$\langle E_{\perp}\rangle$	$\langle E_{\parallel}\rangle$	E_{tot}^{peak}
CR 59	210 meV	163 meV	63 meV	98 meV	188 meV
CR 106	280 meV	210 meV	75 meV	135 meV	256 meV

Table 6.2: Summary of the data obtained from the energy distributions of the electrons photoemitted from CR 59 and CR 106.

The complete energy distributions can be analyzed further to obtain the distributions of the transverse, the longitudinal and the total energies of the complete set of photoelectrons. The results are presented in figure 6.13. It can be seen that the transverse energy distribution peaks at low energies and has a broad tail extending to higher energies. The distribution of the total energies extends from above CBM down to zero (i.e. some of the electrons virtually loose *all* of their initial energy), peaking about 20 meV below the value of $|\chi_{eff}|$. Values for the two cases are summarized in table 6.3.2.

All electrons with total energy below the value of $|\chi_{eff}|$ suffered energy loss during the emission process. The electrons above this value did not lose a considerable amount of energy, but a fraction of them with low longitudinal energies and, correspondingly, high transverse energies, took part in elastic scattering processes.

Red laser illumination

Also in the case of red laser illumination of the cathodes the data will first be discussed by means of density plots. Due to the strong decrease of the electron current at higher

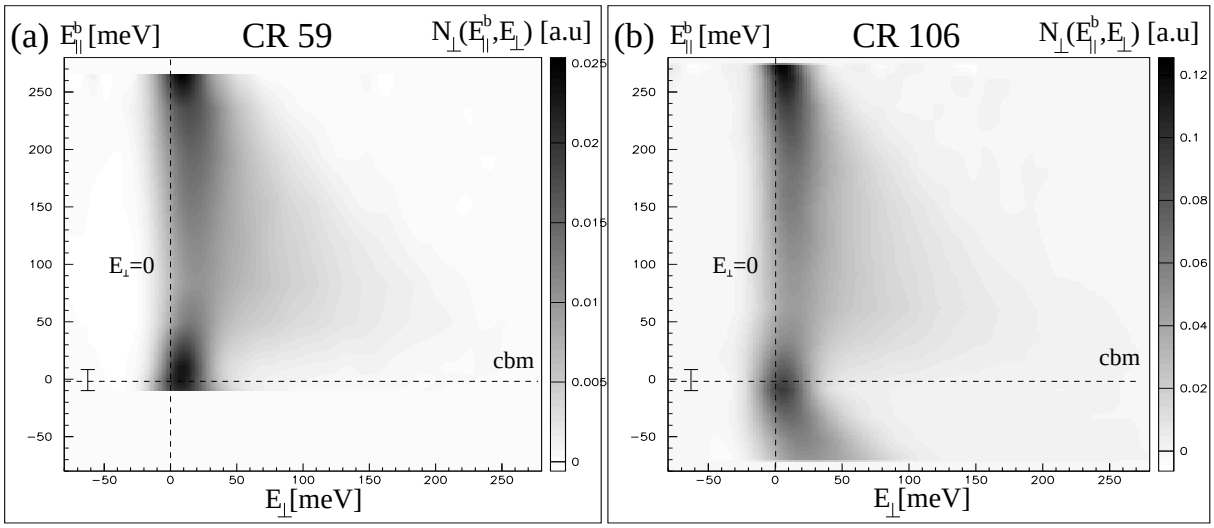

Figure 6.14: Interpolated transverse photoelectron energy distributions $N_\perp(E^b_\parallel, E_\perp)$ obtained for CR 56 (a) and CR 106 (b) under red light illumination. The data is normalized for the same value of $\int dE_\perp \cdot N_\perp(E^b_\parallel, E_\perp)$ for all $E^b_\parallel$. The conduction band minimum (cbm) as well as the line corresponding to $E_\perp$=0 are indicated as dashed lines. The longitudinal energy is referred to the conduction band minimum.

longitudinal energies, it is advantageous not to use the complete distributions for this purpose; they will be discussed below. Figure 6.14 shows the interpolated data, normalized according to condition 6.1.

The data indicate narrow distributions of transverse energy close to the maximum energy accessible to the electrons excited by this laser ($\approx$ 240 meV above CBM): Only little additional energy is available for the transverse degree of freedom from phonon interactions and from the contribution of electrons excited at a $\vec{k}$ with a higher effective mass of the heavy hole band. For an intermediate range of longitudinal energies, the distributions spread considerably. Approaching the CBM, the distributions narrow. Mainly electrons which relaxed to the CBM and thermalized with the bulk contribute to the photoelectron yield at these longitudinal energies. For CR 106 the measurements were extended to below the conduction band minimum. The change of the transverse energy distributions is, in this range of longitudinal energies, apparently very similar to the case of infrared illumination. This is in line with the observation that also the longitudinal EDC approximates the infrared case at longitudinal energies below $|\chi_{eff}|$.

The normalized, complete energy distributions are shown in figure 6.15. Besides a peak corresponding to the onset of emission of electrons which relaxed and thermalized in the bulk, the data show the strong decrease in intensity for rising longitudinal energies. In the

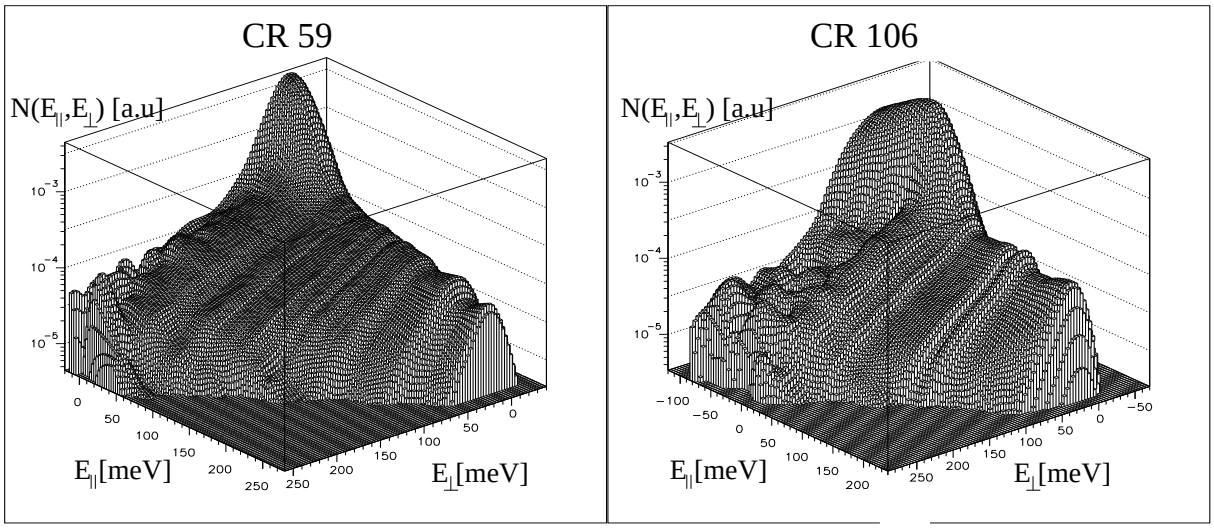

Figure 6.15: Two-dimensional energy distributions $N(E_{\parallel}, E_{\perp})$ for photoelectrons from NEA-GaAs illuminated with red laser light (λ=685 nm). The longitudinal energy scale is referred to the conduction band minimum.

logarithmic representation it is easily seen that the transverse energy of the photoelectrons is approximately limited by a line of constant total energy, corresponding to the energy of electrons which were excited by the red laser light (and underwent phonon scattering).

The modulations at high transverse energies and low longitudinal energies show a methodical limit: While the complete measurement covered several orders of magnitude, a single scan (fixed longitudinal energy) has a dynamic range of about 1.5 orders of magnitude. These structures are thus attributed to noise. The dynamic range could, in principle, be enhanced by measuring the corresponding $N_{\perp}(E_{\parallel}^{b}, E_{\perp})$ in several steps with adjusted parameters of the measurement (e.g. illumination power).

The modulations at high longitudinal energies can be explained by the fact that the raw data of the longitudinal EDCs were used for the normalization, and that smoothing has not been applied.

The data were also used to reconstruct the distribution of total energy of the photoelectrons. The results are shown in figure 6.16 for CR 106. The distribution of total energies of the hot photoelectrons is very similar to the data obtained by Zakharchenya et al. [27] for the steady-state hot-electron energy distribution of GaAs bulk material, determined by measuring the hot-electron photoluminescence. The distribution of these electrons thus seems to be not strongly affected by the transfer through the semiconductor-vacuum interface. Clearly, further investigations are necessary to clarify this point.

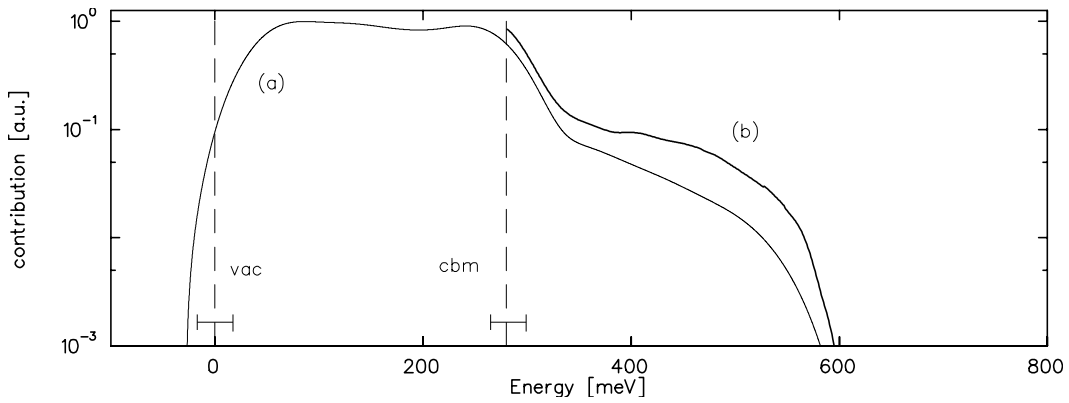

Figure 6.16: Longitudinal EDC obtained under red laser illumination (a), distribution of total energies N_{tot} obtained from $N(E_{\parallel}, E_{\perp})$ of the hot electrons (b). The energy is referred to the vacuum level.

6.4 Photocathode lifetime

The degradation of activated NEA-GaAs photocathodes may limit their potential applications. Particularly at high drawn currents the photocathode lifetime usually drops dramatically. A lifetime of about 40 hours at a dc current of initially 2.2 mA could be demonstrated at room temperature in the preparation chamber [13, 12]. Besides the excellent vacuum conditions in this part of the set-up a further degradation channel was excluded in those measurements: A particular geometry of the electron collector was chosen to avoid the back-stream of ions to the cathode. They could be produced by ionizations of the residual gas or by electron stimulated desorption from the collector. These optimized conditions can, however, not always be met in application. At the electron target for the TSR, which is currently under construction [10, 11], the base pressure is envisaged to be in the low 10^{-11} mbar range.

In order to reach lowest transverse energy spreads of the electron beam, photocathode operation at cryogenic temperatures is planned. These conditions could lead to further constraints of the lifetime of the photocathode since the adsorption of residual gas components is enhanced, particularly of the chemically inactive ones, e.g. CH_4 and Ar. It may appear as if the lower temperatures are advantageous in respect of the photocathode lifetime since thermally activated chemical processes and a potential restructuring of the activation layer are suppressed. However, photocathode lifetimes usually amount to several 100 h at room temperature in the preparation chamber. This shows that these effects, if present, do not limit the lifetime for practical operation.

To investigate the suitability of the conditions of the gun chamber for the application of NEA-GaAs photocathodes, lifetime measurements were performed in this part of the set-up. Figure 6.17 (a) shows a typical decrease of photocurrent in the gun chamber in the case of relatively low initial current of 1 μA. The measurement was performed after cleaning the analyzer with electron bombardment and after cooling the cathode with liquid nitrogen. The cathode was set on -100 V, all other electrodes were grounded. The fitted exponential curve yields a 1/e-lifetime of (41.5$\pm$0.5) hours. Lifetimes in the gun chamber under these conditions have reproducibly been observed to be of the stated order of magnitude.

The obtained values do not differ significantly from the lifetimes observed with the cathode kept at room temperature. Since the photocurrent itself, at least in this order of magnitude, does not lead to a considerable degradation of the photocathode, it can be concluded that the photocathode lifetime in the gun chamber is, in the low-current regime, mainly limited by the vacuum conditions. In spite of the low pressure of about

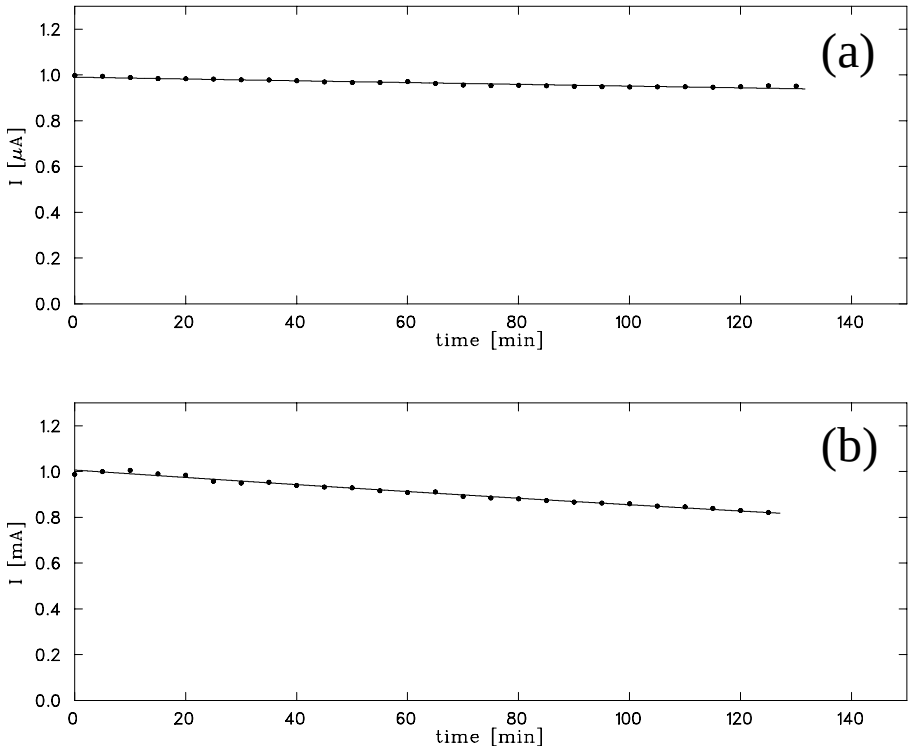

Figure 6.17: Photocathode lifetime measurements at cryogenic sample temperatures in the gun chamber for (a) the low-current regime (initial current 1 μA) and (b) the high-current regime (initial current 1 mA). The fitted exponential curves result in 1/e lifetimes of (41.5±0.5) hours in case (a) and (10.2±0.5) hours in case (b).

$2 \cdot 10^{-11}$ mbar they may not be optimal as the gun chamber was only baked at about 200°C in order to not imperil the rather fragile mounting system of the electron gun. The probably comparatively high partial pressure of H_2O could thus be responsible for the aging of the photocathode.

For the high-current regime the 1/e-lifetime typically amounted to several hours. Figure 6.17 (b) shows an example with an initial current of 1 mA. It was obtained at current limited emission with an extraction and acceleration potential of 270 V. Since the active area of the photocathode is limited by the Pierce-shield to about 7 mm^2, the corresponding current density was about 14 mA/cm^2. The 1/e lifetime in this case amounted to (10.2±0.5) hours.

High dc currents with a lifetime of this order of magnitude under comparable vacuum conditions have not been reported so far.

7. Conclusions and Outlook

This thesis concerns the detailed analysis of energy distributions of electrons photoemitted from NEA-GaAs at cryogenic temperatures. The resolution of the measurements was strongly enhanced by an improvement of the signal to noise ratio and the use of adiabatic transverse compression instead of expansion. A detailed analysis of the systematical errors caused by the non-ideal nature of the magnetic guiding field and of the retarding field analyzer lead to the accuracy necessary to investigate initial transverse energies of the photoelectrons in the few-meV-range. The development and implementation of a new differential method of energy analysis of electron beams permitted the first determination of the complete energy distribution of electron beams photoemitted from NEA-GaAs. The results obtained at cryogenic crystal temperatures can be summarized as follows:

- It was proved to be possible to produce electron beams with transverse beam temperatures in good agreement with the crystal temperature down to 90 K, corresponding to $k_BT \approx$7.8 meV, if only electrons with longitudinal energies higher than about 20 meV below the value of $|\chi_{eff}|$ (i.e. the conduction band minimum) are extracted. These electrons contributed about 6% of the total yield, independent of the activations performed in the present thesis. Since this part of the photoelectrons shows thermal spreads also at room temperature, it apparently crosses the semiconductor-vacuum interface without (strong) interaction.

- A strong peak appears at longitudinal energies about 20-40 meV below the conduction band minimum. It is also resolved in the longitudinal EDCs. It could be resulting from a large fraction of electrons which loose little energy and do not undergo considerable elastic scattering. The peak position is also in good agreement with the calculated position [34] of a two-dimensional quantized subband in the surface-near band bending region. This strong contribution to the photocurrent might thus possibly be attributed to a very effective capture of excited electrons by this level and the emission into vacuum therefrom. Possibly a second level in the band bending region comes into play in the cases of very high $|\chi_{eff}|$.

- It was found that both elastic and inelastic processes evidentally contribute to the overall emission process. The extension of the longitudinal EDCs from above the conduction band minimum down to the vacuum level is thus caused by losses of total energy as well as by changes of the angle of emission, i.e. the transfer of energy from the longitudinal degree of freedom to the transverse ones. Based on the distribution of total energies of the photoelectrons, the fraction of electrons which suffered a loss in total energy can be estimated to be about 30%. The average energy loss of electrons with longitudinal energies below the conduction band minimum amounts to about 1/3 of the initial total energy of $\approx |\chi_{eff}| + k_B T$.

- The energy distributions vary from cathode to cathode, indicating the importance of the influence of the photocathode surface and thus of the cathode preparation procedure. The data obtained indicate that a full activation may be more suitable for a highly efficient emission of cold electrons.

- It was shown that the production of electron beams emitted from a sample at cryogenic temperatures is possible with reasonable lifetimes at current densities in the range desired for the electron target in the envisaged vacuum conditions. Furthermore, it could be demonstrated that the effect of cathode cooling on the lifetime is low. For the production of cold electron beams the initial stages of the degradation are probably not very harmful, since the transmission of the barrier stays, in first approximation, unaffected, while the drop of QY is caused by an increase of the vacuum level (decrease of $|\chi_{eff}|$). This leads to a cut-off of electrons with low longitudinal energy , which would have to be filtered out anyway.

The results indicate promising lines for future research both for methodical improvements and for open physical questions:

The possibility to produce high dc-current electron beams with transverse energy spreads corresponding to the temperature of liquid nitrogen has still to be demonstrated. Since the effective QY for this purpose is only a fraction of the total QY (about 6% of the latter), an illumination power of about 1 W would be necessary to produce the milliampere beam currents of *cold dc* electrons desired for the application in the new electron target. The present cooling facility of the photocathode is incapable of dissipating the heat introduced into the system by an illumination power of this order. A new system for the

photocathode cooling with liquid nitrogen is currently under construction [57, 61].

The new differential method of energy analysis of an electron beam opens up possibilities for a large variety of studies. It could, for example, prove extremely fruitful in the investigation of electron beam relaxations at the new electron target. Besides the possibility to apply expansion parameters of down to $\alpha = \frac{1}{40}$, this device is particularly suited for these experiments since it has an extended drift region and allows a variation of the mode of electron acceleration over a wide range of parameters (see [10, 9]).

A third line of further research is the optimization of the photocathode preparation procedure, aiming at the improvement of the performance of these devices as sources of intense cold electron beams. In particular, systematical investigations concerning the influence of the preparation procedure on the effective QY for this application will be performed subsequent to this thesis. Improvements of the flatness of the surface and the further minimization of chemical contaminations might also lead to even lower, i.e. substantially subthermal, transverse energy spreads.

An extension of the vacuum set-up is currently pursued which will permit the cleaning of the photocathodes by a combination of radiative heating and exposure to atomic hydrogen. The presence of atomic hydrogen allows a more effective cleaning of the photocathodes at lower temperatures compared to the conventional heating procedure [69]. In addition to the better cleaning efficiency, the lower temperatures as well as the action of the atomic hydrogen itself lead to better geometrical surface qualities [70]. Transverse electron heating due to transverse electric fields resulting from cathode roughness or from a spatially varying work function (i.e. contact potentials) can thus be minimized. The time-consuming wet-chemical treatment which does not only require the extraction of the cathodes from the vacuum set-up, but also slightly deteriorates the surface quality of the cathode every time it is performed, will probably be necessary less frequently. The implementation of this new technique will thus lead to higher overall lifetimes of the crystals. It will, in addition, strongly facilitate the preparation procedure of the photocathodes which is especially important for the planned application in the electron target.

In order to easily identify the changes in the photoelectron energy distributions caused by the variations of the preparation procedure and to further elucidate the process of photoemission from NEA-GaAs, several steps should be taken into consideration to further increase the resolution of the energy analysis of electron beams. A reconstruction of the retarding field analyzer optimized for radially constant effective retarding potentials would be particularly advantageous. Also, the sensitivity of the new differential method could

be further improved by using a double lock-in technique. In addition to the modulated marking barrier, the retarding voltage in the analyzer could be modulated. Similar to the measurements of longitudinal EDCs, the derivative of the retarding curve and thus the differential transverse energy distribution could be obtained in-situ this way, leading to higher accuracies than ex-situ numerical differentiation. Finally, it should be considered to cool the photocathodes to even lower temperatures (e.g. by employing liquid helium). Even if this is only possible under low light intensities which would prevent the production of intense cold electron beams, the results obtained for the energy distribution of the photoelectrons should be much more sensitive to changes of the surface conditions in this case, since thermal broadenings are lower.

Bibliography

[1] J. J. Scheer and J. van Laar, *GaAs-Cs: A New Type of Photoemitter*, Solid State Communications **3** (1965), 189.

[2] R. L. Bell, *Negative Electron Affinity Devices*, Clarendon, Oxford, 1973.

[3] C.S. Feigerle, D. T. Pierce, A. Seiler and R. J. Celotta, *Intense source of monochromatic electrons: Photoemission from GaAs*, Appl. Phys. Lett. **44** (1984), 868.

[4] H.-J., Drouhin, C. Hermann and G. Lampel, *Photoemission from activated gallium arsenide. I. Very-high-resolution energy distribution curves*, Phys. Rev. B **31** (1985), 3859.

[5] D. Habs et al., *First Experiments with the Heidelberg Test Storage Ring TSR*, Nucl. Instrum. Meth. B **42** (1989), 290.

[6] S. Pastuszka, U. Schramm, M. Grieser, C. Broude, R. Grimm, D. Habs, J. Kenntner, H.-J. Miesner, T. Schüßler, D. Schwalm and A. Wolf, *Electron cooling and recombination experiments with an adiabatically expanded electron beam*, Nucl. Instrum. Meth. A **369** (1996), 11.

[7] M. Beutelspacher, M. Grieser, D. Schwalm and A. Wolf, *Longitudinal and transverse electron cooling experiments at the Heidelberg heavy ion storage ring TSR*, Nucl.Instr. and Meth. A **441** (2000), 110.

[8] G. H. Jansen, *Coulomb Interaction in Particle Beams*, Adv. El. El. Phys., Supplement 21, Academic Press, Boston, 1990.

[9] M. Schmitt, *Erzeugung energiescharfer Elektronenstrahlen*, Dissertation, Universität Heidelberg, 1999.

[10] F. Sprenger, Dissertation, in preparation.

[11] B. Lange, Diplomarbeit, in preparation.

[12] S. Pastuszka, *Erzeugung kalter Elektronenstrahlen durch Photoemission aus GaAs*, Dissertation, Universität Heidelberg, 1997.

[13] S. Pastuszka, M. Hoppe, D. Kratzmann, D. Schwalm, A. Wolf, A. S. Jaroshevich, S. N. Kosolobov, D. A. Orlov and A. S. Terekhov, *Preparation and performance of transmission-mode GaAs photocathodes as sources of cold dc electron beams*, J. Appl. Phys. **88** (2000), 6788.

[14] S. Pastuszka, D. Kratzmann, D. Schwalm, A. Wolf and A. S. Terekhov, *Transverse energy spread of photoelectrons emitted from GaAs photocathodes with negative electron affinity*, Appl. Phys. Lett. **71** (1997), 2967.

[15] S. Pastuszka, *Messung der transversalen Temperatur magnetisierter Elektronenstrahlen*, Diplomarbeit, Universität Heidelberg, 1994.

[16] P. Krause, *Temperaturrelaxation in magnetisierten Elektrononstrahlen*, Dissertation, Universität Heidelberg, 1992.

[17] D. A. Orlov, M. Hoppe, U. Weigel, A. S. Terekhov, A. Wolf and D. Schwalm, *Energy distributions of electrons emitted from GaAs(Cs,O)*, to be published.

[18] W. E. Spicer, *Negative Affinity 3-5 Photocathodes: Their Physics and Technology*, Appl. Phys. **12** (1979), 115.

[19] S. Adachi, *GaAs, AlAs, and $Al_xGa_{1-x}As$: Material parameters for use in research and device applications*, J. Appl. Phys. **53** (1985), R1.

[20] D. G. Fisher, R. E. Enstrom, J. S. Escher and B. F. Williams, *Photoelectron surface escape probability of (Ga,In)As:Cs-O in the 0.9 to $\approx$ 1.6 μm range*, J. Appl. Phys. **43** (1972), 3815.

[21] J. J. Uebbing and L. W. James, *Behaviour of Cesium Oxide as a Low Work-Function Coating*, J. Appl. Phys. **41** (1970), 4505.

[22] M. G. Burt and V. Heine, *The theory of the workfunction of caesium suboxides and caesium film*, J. Phys. C **11** (1978), 961.

[23] S. Pastuszka, A. S. Terekhov and A. Wolf, *'Stable to unstable' transition in the (Cs,O) acitvation layer on GaAs (100) surfaces with negative electron affinity in extremely high vacuum*, Appl. Surf. Sci. **99** (1996), 361.

[24] V. L. Alperovich, A. G. Paulish and A. S. Terekhov, *Domination of adatom-induced over defect-induced surface states on p-type GaAs(Cs,O) at room temperature*, Phys. Rev. B **50** (1994), 5480.

[25] ———, *Unpinned behaviour of the electronic properties of a p-GaAs(Cs,O) surface at room temperature*, Surf. Sci. **331-333** (1995), 1250.

[26] V. L. Alperovich, A. G. Paulish, H. E. Scheibler and A. S. Terekhov, *Evolution of electronic properties at the p-GaAs(Cs,O) surface during negative electron affinity state formation*, Appl. Phys. Lett. **66** (1995), 2122.

[27] B. P. Zakharchenya, D. N. Mirlin, V. I. Perel and I. I. Reshina, *Spectrum and polarization of hot-electron photoluminescence in semiconductors*, Sov. Phys. Usp. **25** (1982), 143.

[28] R. G. Ulbrich, *Low density photoexcitation phenomena in semiconductors: Aspects of theory and experiment*, Solid-State Electronics **21** (1978), 51.

[29] O. E. Tereshchenko, S. I. Chikichev and A. S. Terekhov, *Atomic structure and electronic properties of HCl-isopropanol treated and vacuum annealed GaAs(100) surface*, Appl. Surf.Sci. **142** (1999), 75.

[30] ———, *Composition and structure of HCl-isopropanol treated and vacuum annealed GaAs(100) surfaces*, J. Vac. Sci. Technol. A **17** (1999), 1.

[31] A. S. Terekhov and D. A. Orlov, *Photoelectron thermalization near the unpinned surface of GaAs(Cs,O) photocathode*, Proc. SPIE **2550** (1995), 157.

[32] ———, *Fine structure in the spectra of thermalized photoelectrons emitted from GaAs with a negative electron affinity*, JETP Lett. **59** (1994), 864.

[33] J. Kirschner, H. P. Oepen and H. Ibach, *Energy- and Spin-Analysis of Polarized Photoelectrons From NEA GaAsP*, Appl. Phys. A **30** (1983), 177.

[34] D. A. Orlov, V. E. Andreev and A. S. Terekhov, *Elastic and Inelastic Tunneling of Photoelectrons from the Dimensional Quantization band at a p^+-GaAs-(Cs,O) Interface into Vacuum*, JETP Lett. **71** (2000), 151.

[35] D. J. Bradley, M. B. Allenson and B. R. Holeman, *The transverse energy of electrons emitted from GaAs photocathodes*, J. Phys. D.: Appl. Phys. **10** (1977), 111.

[36] D. C. Rodway and M. B. Allenson, *In situ surface study of the activating layer on GaAs(Cs,O) photocathodes*, J. Phys. D: Appl. Phys. **19** (1986), 1353.

[37] C. Piaget, R. Polaert and J. C. Richard, *Gallium Indium Arsenide Photocathodes*, Adv. El. El. Phys. **40A** (1976), 377.

[38] C. A. Sanford and N. C. MacDonald, *Electron emission properties of laser pulsed GaAs negative electron affinity photocathodes*, J. Vac. Sci. Technol. B **8** (1990), 1853.

[39] B. R. Holeman, P. C. Conder and J. D. Skingsley, *Proximity Focused Image Intensifier with GaAs Photocathode*, Adv. El. El. Phys. **40A** (1976), 1.

[40] J. H. Pollard, *Directional Properties of Emission from Negative Affinity Photocathodes*, 8th Army Sci. Conf. West Point, New York 1972, published in [2].

[41] G. Vergara, A. Herrera-Gómez, W. E. Spicer, *Electron transverse energy distribution in GaAs negative electron affinity cathodes: Calculations compared to experiments*, J. Appl. Phys. **80** (1996), 1809.

[42] _____, *Calculated electron energy distribution of negative electron affinity cathodes*, Surf. Sci. **436** (1999), 83.

[43] T. Wada, T. Nitta, T. Nomura, M. Miyao and M. Hagino, *Influence of Exposure to CO, CO_2 and H_2O on the Stability of GaAs Photocathodes*, Jap. J. Appl. Phys. **29** (1990), 2087.

[44] H. Lüth, *Surfaces and Interfaces of Solid Materials*, Third Edition, Springer, Berlin, 1997.

[45] A. Herrera-Gómez, G. Vergara and W. E. Spicer, *Physics of high-intensity nanosecond electron source: Charge limit phenomenon in GaAs Photocathodes*, J. Appl. Phys. **79** (1996), 7318.

[46] A. S. Terekhov, private communication.

[47] U. Kolac, M. Donath, K. Ertl, H. Liebl and V. Dose, *High-performance GaAs polarized electron source for use in inverse photoemission spectroscopy*, Rev. Sci. Instrum. **59** (1988), 1933.

[48] V. Guidi, *Anomalous broadening of energy distributions in photoemitted electron beams*, J. Appl. Phys. **79** (1996), 8187.

[49] H.-J. Drouhin and Ph. Bréchet, *Origin of anomalous energy spreads in photoelectron beams*, Appl. Phys. Lett. **56** (1990), 2152.

[50] J. D. Jackson, *Classical Electrodynamics*, Wiley & Sons, New York, 1962.

[51] T. M. O'Neil, *Collision operator for a strongly magnetized pure electron plasma*, Phys. Fluids **26** (1983), 2128.

[52] V. I. Kudelainen, V. A. Lebedev, I. N. Meshkov, V. V. Parkomchuk and B. N. Sukhina, *Temperature relaxation in a magnetized electron beam*, JETP **56** (1982), 1191.

[53] G. A. Antypas and J. Edgecumbe, *Glass-sealed GaAs-AlGaAs transmission photocathode*, Appl. Phys. Lett. **26** (1975), 371.

[54] R. P. Vasques, B. F. Lewis, F. J. Grunthaner, *Cleaning chemistry of GaAs(100) and InSb(100) substrates for molecular-beam epitaxy*, J. Vac. Sci. Technol. B **1** (1983), 719.

[55] Z. Zong, S. Shogen, M. Kawasaki and I. Suemune, *X-ray photoelectron spectroscopy and atomic force microscopy surface study of GaAs(100) cleaning procedures*, J. Vac. Sci. Technol. B **13** (1995), 77.

[56] Y. Y. Lau, *Effects of cathode surface roughness on the quality of electron beams*, J. Appl. Phys. **61** (1987), 36.

[57] U. Weigel, *Spektroskopische Verfahren zur Temperaturbestimmung von GaAs-Photokathoden*, Diplomarbeit, Universität Heidelberg, 1999.

[58] M. Hoppe, D. A. Orlov, A. S. Terekhov, U. Weigel, A. Wolf and D. Schwalm, *Photoluminescence-based control of annealing temerature during NEA-GaAs photocathode preparation*, Proc. of the International Workshop on Polarized Sources and Targets PST99 (Erlangen), 1999, p. 506.

[59] Y. P. Varshni, *Temperature dependence of the energy gap in semiconductors*, Physica (Utrecht) **39** (1967), 149.

[60] M. Kamaratos and E. Bauer, *Interaction of Cs with the GaAs(100) surface*, J. Appl. Phys. **70** (1991), 7565.

[61] U. Weigel, Dissertation, in preparation.

[62] J. R. Pierce, *Theory and design of electron beams*, Van Nostrand, New York, 1954.

[63] D. Kratzmann, *Messung der transversalen Energie von Elektronenstrahlen aus GaAs-Photokathoden*, Diplomarbeit, Universität Heidelberg, 1997.

[64] U. Rossler, *Nonparabolicity and warping in the conduction band of GaAs*, Solid State Commun. **49** (1984), 943.

[65] D. A. Orlov, private communication.

[66] O. E. Tereshchenko, V. L. Alperovich and A. S. Terekhov, *Cs/GaAs(100) surface: two-dimensiojnal metal or Hubbard insulator ?*, JETP Lett. **70** (1999), 550.

[67] V. E. Andreev, V. V. Bakin, A. K. Bakarov, A. S. Jaroshevich, M. A. Kirillov, S. N. Kosolobov, H. E. Scheibler, S. V. Shevelev, A. I. Toporov and A. S. Terekhov, *Angular distribution and spin scattering of photoelectrons emitted from GaAs photocathode*, Proc. of the International Workshop on Polarized Sources and Targets PST 99 (Erlangen), 1999, p. 238.

[68] Ph. Ebert, T. Zhang, F. Kluge, M. Simon, Z. Zhang and K. Urban, *Importance of Many-Body Effects in the Clustering of Charged Zn Dopant Atoms in GaAs*, Phys. Rev. Lett. **83** (1999), 757.

[69] K. A. Elamrawi and H. E. Elsayed-Ali, *GaAs photocathode cleaning by atomic hydrogen from a plasma source*, J. Phys. D: Appl. Phys. **32** (1999), 251.

[70] T. Akatsu, A. Plößl, H.Stenzel and U. Gösele, *GaAs wafer bonding by atomic hydrogen surface cleaning*, J. Appl. Phys. **86** (1999), 7146.

Danksagung

'Experimentalphysik ist Teamwork'; diese Aussage gilt wohl in besonderem Maße für eine 'festkörperlastige' Arbeit, die in einer Atomphysik-Gruppe in einem Institut für Kernphysik durchgeführt wurde. Ich möchte deshalb nicht schließen, ohne mich zumindest bei Einigen derjenigen zu bedanken, die zu dieser Arbeit beigetragen haben.

Zunächst einmal danke ich meinem Betreuer Prof. Dr. Andreas Wolf und gleichermaßen Prof. Dr. Dirk Schwalm für die Möglichkeit, diese Arbeit unter den hervorragenden Bedingungen durchzuführen, die das Max-Planck-Institut für Kernphysik bietet. Sie haben mir auch in Phasen ohne erkennbaren Fortschritt Vertrauen entgegengebracht. Darüber hinaus werden mir beide nicht nur wegen mancher richtiger Antwort in Erinnerung bleiben, sondern vor allem wegen ihrer erstaunlichen Fähigkeit, praktisch immer die richtige *Frage* zu stellen.

Herrn Prof. Dr. Reinhard Neumann danke ich für die freundliche Bereitschaft, das Zweitgutachten zu erstellen.

Ein herzlicher Dank geht an Prof. Dr. Alexander 'Sasha' Terekhov vom Institut für Halbleiterphysik in Novosibirsk. Er hat mich jederzeit bereitwillig an seiner Erfahrung teilhaben lassen. Diskussionen mit ihm waren immer ein Vergnügen, nicht nur die physikalischen.

Dr. Dmitry 'Dima' Orlov möchte ich besonders danken. Er hat als Post-Doc einen reichen Schatz an Erfahrungen und Kenntnissen aus Novosibirsk mitgebracht. Über das transferierte Wissen hinaus hat er durch seinen Ideenreichtum, gepaart mit seiner steten Begeisterung für das Thema, außerordentlich zum Gelingen der Arbeit beigetragen.
Intensive, enge Zusammenarbeit führt zu Reibung. Wir waren jedoch (meist) in der Lage, die scheinbar verlustig gegangene Energie in produktive Wärme umzuwandeln.

'Meinem' ehemaligen Diplomanden und späteren Doktoranden-Kollegen Diplom-Physiker Udo Weigel danke ich für vielfältige Hilfestellungen und Diskussionen.

Alle Mitglieder der Arbeitsgruppe waren stets auch an Fragen außerhalb ihres speziellen Themas interessiert; die sich ergebenden Diskussionen sowie die stete Hilfbereitschaft haben eine Atmosphäre von außerordentlicher Produktivität geprägt. Besonders erwähnen möchte ich die Herren Diplom-Physiker Frank Sprenger, Peter Witte und Guido Saathof.

Die Arbeit wäre undenkbar gewesen ohne die vielfältige Unterstützung der 'nicht-wissenschaftlichen' Mitarbeiter. Neben dem kollegialen Umgang möchte ich zwei Aspekte hervorheben, die mir immer wieder besonders angenehm aufgefallen sind. Da wäre zunächst das (berechtigte) Vertrauen bzw. die gute Menschenkenntnis, die dazu führte, daß sie sich im gegebenen Falle von der Dringlichkeit einer Aufgabe überzeugen ließen. Darüberhinaus bin ich recht sicher, in meiner gesamten Zeit am Institut nicht einmal 'Geht nicht' gehört zu haben. Wenn, dann führte die Entgegnung 'Geht *so* nicht, aber man könnte vielleicht ...' zu einer produktiven Diskussion, die sowohl von Respekt vor als auch von Interesse an den 'Wissenschaften' des jeweils anderen geprägt war.

Einer Vielzahl von Freunden und Bekannten 'außerhalb' der Physik danke ich für das eine oder andere 'Reset'. Durch diverse 'kill -9 PID' konnte außerdem eine Überhitzung des Prozessors durch abgestürzte Prozesse genauso zuverlässig vermieden werden wie die Notwendigkeit einer Neuinstallation des Betriebssystems. Eine Aufzählung im einzelnen ist kaum möglich. Ich bin jedoch sicher, daß auch die Computer-Laien unter ihnen (in etwa) verstehen, was ich meine.
Besonders erwähnen möchte ich allerdings Tanja Bischoff, die nicht nur vielfältige sprachliche Verbesserungsvorschläge machte, sondern mich in der Schlußphase der Arbeit auch mit erstaunlicher Geduld ertragen und mir auf unnachahmliche Art und Weise Mut gemacht hat.